SPRINGER BRIEFS IN APPLIED SCIENCES AND TECHNOLOGY · STRUCTURAL MECHANICS

Leslie Banks-Sills

Interface Fracture and Delaminations in Composite Materials

Springer

SpringerBriefs in Applied Sciences and Technology

Structural Mechanics

Series editor

Emmanuel E. Gdoutos, Department of Theoretical and Applied Mechanics, Democritus University of Thrace, Xanthi, Greece

More information about this series at http://www.springer.com/series/15039

Leslie Banks-Sills

Interface Fracture and Delaminations in Composite Materials

Springer

Leslie Banks-Sills
School of Mechanical Engineering
Tel Aviv University
Ramat Aviv, Tel Aviv
Israel

ISSN 2191-530X ISSN 2191-5318 (electronic)
SpringerBriefs in Applied Sciences and Technology
ISSN 2520-8020 ISSN 2520-8039 (electronic)
SpringerBriefs in Structural Mechanics
ISBN 978-3-319-60326-1 ISBN 978-3-319-60327-8 (eBook)
DOI 10.1007/978-3-319-60327-8

Library of Congress Control Number: 2017943232

Printed on acid-free paper

This Springer imprint is published by Springer Nature
The registered company is Springer International Publishing AG
The registered company address is: Gewerbestrasse 11, 6330 Cham, Switzerland

We cannot expect in the immediate future that all women who seek it will achieve full equality of opportunity. But if women are to start moving towards that goal, we must believe in ourselves or no one else will believe in us; we must match our aspirations with the competence, courage and determination to succeed.

Rosalyn Yalow: Medical Physicist, awarded the Nobel prize in 1977

And, for my dear husband, Zvi, my wonderful children, Deborah and Rachel, and my grandchildren.

Preface

After many years of working in the field of fracture mechanics and, in particular, interface fracture and delaminations of composites, I finally was able to put together this brief description of these subjects. I was inspired by former mentors Bernie Budiansky, John Hutchinson, Jim Rice and Lyle Sanders. As some may say, I stood on the shoulders of these giants. Of course, in Israel, I am indebted to Jacob Aboudi for our many conversations over many years at Tel Aviv University. I came to Tel Aviv University as a theoretician and, early on, was requested to build a laboratory. I spent seven years working with Mircea Arcan who aided me in learning experimental methods. There is no greater satisfaction than carrying out experiments which are able to demonstrate various theories. I recommend that to everyone.

Working with many graduate students over the years honed my knowledge of these subjects, as well as others. My first graduate student was Chanan Gabay, an officer in the Israeli Air Force, who knocked on my door one day at Tel Aviv University saying that he had been waiting for me to arrive in Israel in order to work on fracture mechanics. My other students, to whom I am grateful, include: Jacob Bortman, Israel Wander, Daniel Schur, Navah Sela, Izhak Marmur, Aharon Rub, Ami Danieli, Dov Sherman, Yehuda Wolpert, David Loya, Ran Schwartman, Daining Fang, Elimor Makevet, Vadim Leiderman, Dana Ashkenazi, Alla Sherer, Vinodkumar Boniface, Yaacov Schwartz, Avraham Dorogoy, Chaim Ishbir, Orly Dolev, Ron Shachar, Itai Herskovitz, Yuval Freed, Lucy Shemesh, Iddo Kressel, Natalie Konovalov, Dror Decad, Jenny Shklovsky, Yael Buimovitz, Arcady Alperovitch, Liran Rogel, Yael Hikry, Liat Heller, Or Ben David, Maya Gohfeld, Gil Noivirt, Tal Simhi, Guy Shiber, Ido Simon, Elad Farkash, Mor Mega, Tomer Chocron and Hila Ben Gur. Of course, the two engineers who work in my laboratory, Rami Eliasi and Victor Fourman, are always there to help.

I am indebted to an understanding husband who allows me to work all of the time with nary a complaint. My daughters are also remembered for having suffered my absences.

Tel Aviv, Israel
May 2017

Leslie Banks-Sills

Contents

Symbols

a	Half-crack length
a_0	Initial delamination length
A_1	Virtual crack extension area
A_k	Integration area for the M-integral in material k
A_{0k}	Additional integration area for the thermal M-integral in material k
$A_{ij}^{(k)}$	Components of the matrix $\mathbf{A}_k$
$\mathbf{A}_k$	3×3 matrix related to mechanical properties of material k
b	Specimen width
B	Thickness of Brazilian disk specimen
$B_{ij}^{(k)}$	Components of the matrix $\mathbf{B}_k$
$\mathbf{B}_k$	3×3 matrix related to mechanical properties of material k
c	Lever arm
d_i, $\hat{d}_i$	Components of the eigenvectors $\mathbf{d}$ and $\hat{\mathbf{d}}$
$\mathbf{d}$, $\hat{\mathbf{d}}$	3×1 eigenvectors
D_{ij}, $i,j = 1.2.3$	Components of the tensor $\mathbf{D}$
$\mathbf{D}$	Tensor related to Barnett–Lothe tensor $\mathbf{L}_k$
E	Young's modulus
E_k	Young's modulus of material k
E_A, E_T	Axial and transverse Young's moduli
F_{jm}	j-component of nodal point force at node m
g	Ratio of $\mathcal{G}_{II}$ to $\mathcal{G}_I$
G_A, G_T	Axial and transverse shear moduli
$\mathcal{G}$	Griffith's energy or energy release rate
$\mathcal{G}_i$	Interface energy release rate
$\mathcal{G}_1$	Mode 1 energy release rate
$\mathcal{G}_c$	Critical energy release rate
$\mathcal{G}_{ic}$	Critical interface energy release rate
$\mathcal{G}_{ic}^*$	Reduced critical interface energy release rate

$\mathcal{G}_{1c}$	Critical mode 1 energy release rate
$\overline{\mathcal{G}}_{1c}$	Average critical mode 1 energy release rate
$\mathcal{G}^*_{1c}$	Reduced critical mode 1 energy release rate
$\mathcal{G}_I$	Mode I energy release rate
$\mathcal{G}_{II}$	Mode II energy release rate
$\mathcal{G}_{Ic}$	Mode I critical energy release rate or fracture toughness
$\mathcal{G}_{IR}$	Resistance mode I energy release rate
h, $2h$	Specimen thickness
H, H_1, H_2	Effective Young's moduli
i	$\sqrt{-1}$
$\Im$	Imaginary part of a complex quantity
$\mathcal{I}_I$, $\mathcal{I}_{II}$	Integrals used in VCCT
$\mathcal{I}_I^{(T)}$, $\mathcal{I}_{II}^{(T)}$	Integrals used in VCCT for transversely isotropic material
J	J-integral
$k = 1, 2$	Subscript or superscript denoting upper or lower material
K_I, K_{II}, K_{III}	Modes I, II and III stress intensity factors
K_{Ic}	Plane strain fracture toughness
K	Complex stress intensity factor; also statistical factor
$\hat{K}$	Normalized complex stress intensity factor
K_1, K_2, K_3	Modes 1, 2 and 3 stress intensity factors
K_1^*, K_2^*, K_{III}^*	Local stress intensity factors
$\mathbf{K}$	6×6 rotation matrix
ℓ	Length of finite element
$\ell_1^{(N)}(x_3)$	Length of virtual crack extension in element N
ℓ_j, $j = 2, 3, 4$	Sextic functions
L, l	Longitudinal length measurement
$\hat{L}$	Length scale used in fitting interface fracture test data
$\mathbf{L}_k$	Barnett–Lothe tensor of material k
m, m'	Number of nodal points in an element; also nodal point number
$M^{(1,2)}$	M-integral
n_i, $i = 1, 2, 3$	Components of normal vector
N	Number of samples; also element in which virtual crack extension is carried out
N_i	Shape functions
$p_i^{(k)}$ $i = 1, 2, 3$	Eigenvalues of the compatibility equations
P	Probability of failure
q_1	Normalized virtual crack extension
r, θ	Crack tip polar coordinates
R	Radius of Brazilian disk specimen
$\Re$	Real part of a complex quantity
s	Arc length; also contact zone length in Comninou model; also standard deviation

$s_{\alpha\beta}$ $\alpha, \beta = 1, ..., 6$	Components of the compliance matrix
$s'_{\alpha\beta}$ $\alpha, \beta = 1, ..., 6$	Reduced compliance components
$\breve{\mathbf{S}}$	3×3 tensor related to oscillatory parameter
$\mathbf{S}_k$	Barnett–Lothe tensor of material k
t	t-statistic
T	Transpose; also total
T_i, $i = 1, 2, 3$	Components of the traction vector
u_i, $i = 1, 2, 3$	Cartesian displacement components
$\mathbf{u}$	Displacement vector
$\mathbf{u}_i$	Nodal point displacement vector
${}_kU_i^{(s)}(\theta)$, $i = 1, 2, 3$	Displacement function for material k, $s = 1, 2, III$
V_k, $k = 1, 2$	Volume in which M-integral is carried out
W	Strain energy density
$W^{(1,2)}$	Interaction strain energy density of solutions (1) and (2)
W_F	Strain energy density for thermal problem
$W_F^{(1,2)}$	Interaction strain energy density for thermal problem
W_{ij}, $i,j = 1, 2, 3$	Components of the tensor $\mathbf{W}$
$\mathbf{W}$	Tensor related to Barnett–Lothe tensors $\mathbf{S}_k$ and $\mathbf{L}_k$
$\mathbf{x}$	Coordinate vector
$\mathbf{x}_i$	Nodal point coordinate vector
z_P, z_γ	Standard variate with probability P and confidence γ
$z_*^{(k)}$	Complex variable given by $x_1 + p_*^{(k)} x_2$
α	Coefficient of thermal expansion
α_A, α_T	Axial and transverse coefficients of thermal expansion
${}_k\alpha_{ij}$ $i,j = 1, 2, 3$	Components of coefficient of thermal expansion for anisotropic material k
β	Dundurs' like parameter
β_A, β_T	Axial and transverse inverse coefficients of thermal expansion
$\tilde{\beta}_k$	Inverse coefficient of thermal expansion for isotropic material k
β_{ij}^k, $i,j = 1, 2, 3$	Inverse coefficient of thermal expansion for anisotropic material k
$\beta_i^{(k)}$, $i = 1, 2, 3$	Related to the eigenvalues $p_i^{(k)}$ for material k
γ	Specific surface energy; also statistical confidence
Γ	J-integral contour
δ_i, $i = 1, 2, 3$	Stress singularities
δ_{ij}	Kronecker delta
Δ, Δ_1	Factors related to the eigenvalues of the compatibility equations
Δu_i, $i = 1, 2, 3$	Crack face displacement jumps
Δa	Virtual crack extension; also crack length increment
ε	Oscillatory parameter

η	Constant related to mechanical properties
ϑ_k	Temperature change in material k
κ	Kosolov's constant
κ_k	Kosolov's constant for material k
λ_k	Lamé constant for material k
Λ	Constant related to mechanical properties
μ	Shear modulus
μ_k	Shear modulus for material k
ν	Poisson's ratio
ν_k	Poisson's ratio for material k
ν_A, ν_T	Axial and transverse Poisson's ratios
ξ, η, ζ	Coordinates in the parent element
ξ_i, η_i, ζ_i	Coordinates of the nodal points in the parent element
Π	Potential energy
σ	Applied tensile stress
σ_{ij}, $i,j = 1,2,3$	Cartesian stress components
${}_k\Sigma_{ij}^{(s)}(\theta)$	Stress function for material k, $s = 1,2,III$, $i,j = 1,2,3$
τ	Applied shear stress
ϕ	Phase angle or mode mixity
ϕ_j	Stress function components
$\boldsymbol{\phi}$	Stress function vector
χ	Angle related to ε and r
ψ	Phase angle or mode mixity
ω	Brazilian disk specimen loading angle
Ω	Constant related to mechanical properties

Chapter 1
Introduction

Abstract In this chapter, the basic tenets of fracture mechanics are described. The first term of the asymptotic expression for the stress and displacement fields in the neighborhood of a crack tip is presented for a homogeneous, isotropic, linear elastic material. The concept of fracture modes and stress intensity factors are discussed. The energy approach through the Griffith energy is delineated. A presentation of the J-integral and its relationship to the Griffith energy and the stress intensity factors is given. A description of a fracture criterion through the fracture toughness is presented.

Keywords Energy release rate · Fracture mechanics · Fracture modes · Fracture toughness · Griffith energy · J-integral · Square-root singularity · Stress intensity factor

The earliest work on fracture mechanics begins with Griffith's publications in the 1920s [3, 4] in which an energy based fracture criterion was presented. The investigation was based on an earlier solution of an elliptical hole in an infinite sheet [9]. Griffith carried out tests on glass to substantiate the finding that defects decrease the fracture strength of a structure. Orowan [15] confirmed Griffith's theory in the case of a crystalline material. Westergaard [24] derived a complex variable stress function for the distribution of the stress in an infinite body resulting from a finite length crack. For the first time, the stresses were seen to be square-root singular. The first term of the asymptotic expansion of the stress components in the neighborhood of a two-dimensional and a penny-shaped crack was presented by Sneedon [21]. These investigations form an early basis of fracture mechanics. Later, Irwin who was working for the Naval Research Laboratory in the US, became interested in fracture as a result of the failure of Liberty ships which fractured in two while in calm waters. He wrote several reports and presented fracture studies at scientific meetings in the late 1940s [10, 23].

In 1957, both Irwin and Williams in the same journal [11, 25] developed the asymptotic expansion for the stress components in the neighborhood of a crack tip for linear elastic, homogeneous and isotropic materials. Irwin [11] determined the in-plane normal stresses σ_{xx} and σ_{yy} for mode I deformation and defined the amplitude of the square-root stress singularity in terms of the energy release rate $\mathcal{G}$. Williams [25] presented the first two terms of the series which were found by means

L. Banks-Sills, *Interface Fracture and Delaminations in Composite Materials*,
SpringerBriefs in Structural Mechanics, DOI 10.1007/978-3-319-60327-8_1

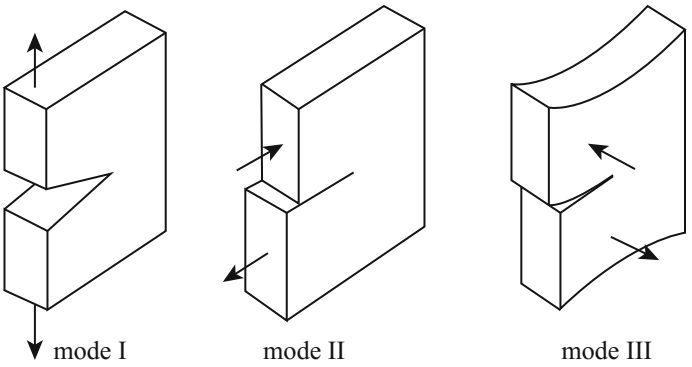

Fig. 1.1 Three modes of fracture

of a stress function. In addition, Irwin related the stress intensity factor to the energy release rate through the crack closure integral for all three modes [12]. By this time, the stress intensity factor concept had been in use for two years [23]. In [12], the first term of the asymptotic expansion of the stress and displacement fields for all three modes was presented.

For this type of material, there are three deformation modes of fracture as shown in Fig. 1.1. Mode I is the opening mode in which the crack faces open; mode II is the in-plane sliding mode in which the crack faces slide within the plane; and mode III is the tearing or out-of-plane sliding mode in which the crack faces move out-of-the plane in opposite directions. The first term of the stress and displacement fields for mode I is given by

$$\begin{Bmatrix} \sigma_{11} \\ \sigma_{12} \\ \sigma_{22} \end{Bmatrix} = \frac{K_I}{\sqrt{2\pi r}} \cos\frac{\theta}{2} \begin{Bmatrix} 1 - \sin\frac{\theta}{2}\sin\frac{3\theta}{2} \\ \sin\frac{\theta}{2}\cos\frac{3\theta}{2} \\ 1 + \sin\frac{\theta}{2}\sin\frac{3\theta}{2} \end{Bmatrix} \tag{1.1}$$

$$\begin{Bmatrix} u_1 \\ u_2 \end{Bmatrix} = \frac{K_I}{2\mu}\sqrt{\frac{r}{2\pi}} \begin{Bmatrix} \cos\frac{\theta}{2}\left(\kappa - 1 + 2\sin^2\frac{\theta}{2}\right) \\ \sin\frac{\theta}{2}\left(\kappa + 1 - 2\cos^2\frac{\theta}{2}\right) \end{Bmatrix} \tag{1.2}$$

where K_I is the mode I stress intensity factor, r and θ are the crack tip polar coordinates as shown in Fig. 1.2,

$$\kappa = \begin{cases} 3 - 4\nu & \text{plane strain} \\ (3-\nu)/(1+\nu) & \text{generalized plane stress} \end{cases} \tag{1.3}$$

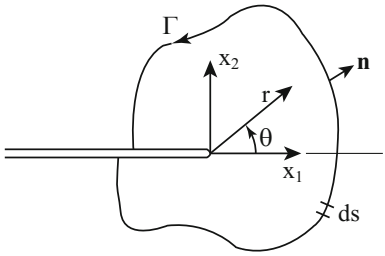

Fig. 1.2 Crack tip geometry

ν is Poisson's ratio and μ is the shear modulus. The subscripts $i = 1, 2, 3$ represent Cartesian coordinates.

For mode II deformation, the first term of the stress and displacement fields is given by

$$\begin{Bmatrix} \sigma_{11} \\ \sigma_{12} \\ \sigma_{22} \end{Bmatrix} = \frac{K_{II}}{\sqrt{2\pi r}} \begin{Bmatrix} -\sin\frac{\theta}{2}\left(2+\cos\frac{\theta}{2}\cos\frac{3\theta}{2}\right) \\ \cos\frac{\theta}{2}\left(1-\sin\frac{\theta}{2}\sin\frac{3\theta}{2}\right) \\ \cos\frac{\theta}{2}\sin\frac{\theta}{2}\cos\frac{3\theta}{2} \end{Bmatrix} \tag{1.4}$$

$$\begin{Bmatrix} u_1 \\ u_2 \end{Bmatrix} = \frac{K_{II}}{2\mu}\sqrt{\frac{r}{2\pi}} \begin{Bmatrix} \sin\frac{\theta}{2}\left(\kappa+1+2\cos^2\frac{\theta}{2}\right) \\ -\cos\frac{\theta}{2}\left(\kappa-1-2\sin^2\frac{\theta}{2}\right) \end{Bmatrix} \tag{1.5}$$

where K_{II} is the mode II stress intensity factor.

For mode III deformation, the first term of the asymptotic expansion for the stress and displacement fields is

$$\begin{Bmatrix} \sigma_{13} \\ \sigma_{23} \end{Bmatrix} = \frac{K_{III}}{\sqrt{2\pi r}} \begin{Bmatrix} -\sin\frac{\theta}{2} \\ \cos\frac{\theta}{2} \end{Bmatrix} \tag{1.6}$$

$$u_3 = 2\frac{K_{III}}{\mu}\sqrt{\frac{r}{2\pi}}\sin\frac{\theta}{2} \tag{1.7}$$

where K_{III} is the mode III stress intensity factor.

Equations (1.1)–(1.7) represent a universal solution for the stress and displacement components in the neighborhood of a crack tip. For each mode, the field quantities have the same r and θ dependence. Moreover, from Eqs. (1.1), (1.4) and (1.6), it is

possible to observe that the stresses are square-root singular in the neighborhood of the crack tip. This means that the stresses are becoming infinite as $r \to 0$. Physically, the stresses cannot become infinite. There must be some mechanism which will mitigate these high stresses. For metals it is plasticity; for polymers, crazing; for rocks; micro-cracks. The stress intensity factor is the amplitude of the singularity. This quantity determines the severity of the stresses at the crack tip. As an example, for a crack of length $2a$ in an infinite body, subjected to a tensile stress σ far from the crack and perpendicular to it, the stress intensity factor may be found as

$$K_I = \sigma\sqrt{\pi a}\ . \tag{1.8}$$

This is known as a Griffith crack. Note that the units of K are $F/L^{3/2}$ where F represents force and L, length. There are handbooks containing stress intensity factor solutions [14, 19, 20, 22].

In [3], a fracture criterion was proposed in which the energy necessary to create a new surface γ is balanced by the decrease in the potential energy Π of the system for a unit increase in crack length. That is,

$$\mathcal{G} = -\frac{\partial \Pi}{\partial a}\ . \tag{1.9}$$

One can then postulate that a crack will propagate when

$$\mathcal{G} = 2\gamma \tag{1.10}$$

where $\mathcal{G}$ is Griffith's energy, the energy release rate or the crack driving force. The factor 2 appears in Eq. (1.10) since there are two fracture surfaces as the crack expands. The expression in Eq. (1.10) is for very brittle materials such as single crystal materials. For others, there will be dissipative energy, so that one may write

$$\mathcal{G} = \mathcal{G}_c \tag{1.11}$$

where $\mathcal{G}_c$ is the critical energy release rate. Many authors write $\Gamma \equiv \mathcal{G}_c$.

Using the crack closure integral of Irwin [12], a relation between the energy release rate $\mathcal{G}$ and the stress intensity factors may be found as

$$\mathcal{G} = \begin{cases} \dfrac{1-\nu^2}{E}\left(K_I^2 + K_{II}^2\right) + \dfrac{1+\nu}{E}K_{III}^2 & \text{plane strain} \\ \dfrac{1}{E}\left(K_I^2 + K_{II}^2\right) & \text{generalized plane stress} \end{cases} \tag{1.12}$$

where E is Young's modulus.

Another important concept in fracture mechanics is that of the path independent J-integral. In 1968, Rice [17], in a ground breaking investigation, presented the J-integral given as

$$J = \int_{\Gamma} \left(W n_1 - T_i \frac{\partial u_i}{\partial x_1} \right) ds \tag{1.13}$$

where Γ is a curve beginning on the lower crack face and ending on the upper crack face (see Fig. 1.2), W is the strain energy density, n_1 is the component of the outer normal $\mathbf{n}$ to the curve Γ in the x_1-direction, T_i and u_i are, respectively, the traction and displacement vectors on Γ with $i = 1, 2$, x_1 is the coordinate shown in Fig. 1.2 and ds is the differential arc length along Γ. It was shown in [18] that

$$J = \mathcal{G} \, . \tag{1.14}$$

Hence, the relation between $\mathcal{G}$ and the stress intensity factors in Eq. (1.12) holds for J. An interesting proof of Eq. (1.14) may be found in [13].

Knowing the stress field in the neighborhood of a crack tip is not sufficient to predict fracture. To that end, a fracture criterion is required. This may be in the form of Eq. (1.11) in which crack propagation is predicted when the energy release rate reaches a critical value. This critical value depends on material and environment. By considering Eq. (1.12) and mode I deformation only,

$$\mathcal{G} = \frac{1}{H} K_I^2 \tag{1.15}$$

where

$$\frac{1}{H} = \begin{cases} \dfrac{1 - \nu^2}{E} & \text{plane strain} \\ \dfrac{1}{E} & \text{generalized plane stress} \, . \end{cases} \tag{1.16}$$

Hence, the criterion in Eq. (1.11) is equivalent to

$$K_I = K_{Ic} \tag{1.17}$$

where K_{Ic} is the plane strain fracture toughness, which is dependent on material and environment. See [1] for details concerning fracture toughness testing. Early development of the test method may be found in [2]. Compendia of papers in which the fracture toughness and Paris Law [16] parameters for various materials may be found in [5–8].

References

1. American Standard E399-12ϵ1 (2013) Standard test method for linear-elastic plane-strain fracture toughness K_{Ic} of metallic materials. In: Metals – mechanical testing; elevated and low-temperature tests; metallography, vol. 3.01. American Society for Testing and Materials, West Conshohocken, pp 519–551
2. Brown WF Jr, Srawley JE (1966) Plane strain crack toughness testing of high strength metallic materials. ASTM-STP 410. American Society of Testing and Materials, Philadelphia
3. Griffith AA (1921) The phenomena of rupture and flow in solids. Philos Trans R Soc A221:163–198
4. Griffith AA (1924) The theory of rupture. In: Biezeno CB, Burgers JM (eds) Proceedings of the first international congress for applied mechanics. Waltman J Jr, Delft, the Netherlands, pp 55–63
5. Hudson CM, Seward SK (1978) A compendium of sources of fracture toughness and fatigue crack growth data for metallic alloys. Int J Fract 14:R151–R184
6. Hudson CM, Seward SK (1982) A compendium of sources of fracture toughness and fatigue crack growth data for metallic alloys-part II. Int J Fract 20:R59–R117
7. Hudson CM, Seward SK (1989) A compendium of sources of fracture toughness and fatigue crack growth data for metallic alloys-part III. Int J Fract 39:R43–R60
8. Hudson CM, Seward SK (1991) A compendium of sources of fracture toughness and fatigue crack growth data for metallic alloys-part IV. Int J Fract 48:R19–R43
9. Inglis CE (1913) Stresses in a plate due to the presence of cracks and sharp corners. Trans Inst Nav Archit 55:219–241
10. Irwin GR (1948) Fracture dynamics. In: Jonassen F, Roop WP, Bayless RT (eds) Fracturing of metals. American Society for Metals, Cleveland, pp 147–166
11. Irwin GR (1957) Analysis of stresses and strains near the end of a crack traversing a plate. J Appl Mech 24:361–364
12. Irwin GR (1958) Fracture. In: Flügge S (ed) Handbuch der physik, vol VI. Springer, Germany, pp 551–590
13. Kanninen MF, Popelar CH (1985) Advanced fracture mechanics. Oxford Engineering Science, England, pp 164–166
14. Murakami Y (1987, 1992, 2001) Stress intensity factors handbook, vol 1–5. Pergamon Press, Oxford
15. Orowan E (1934) Die mechanischen festigkeitseigenschaften und die realstruktur der kristalle. Z Krist 89:327–343
16. Paris PC, Erdogan F (1963) A critical analysis of crack propagation laws. J Basic Eng 85:528–534
17. Rice JR (1968) A path independent integral and the approximate analysis of strain concentration by notches and cracks. J Appl Mech 35:379–386
18. Rice JR (1968) Mathematical analysis in the mechanics of fracture. In: Liebowitz H (ed) Fracture, vol II. Academic Press, New York, pp 191–311
19. Rooke DP, Cartwright DJ (1976) Compendium of stress intensity factors. Her Majesty's Stationary Office, London
20. Sih GC (1973) Handbook of stress intensity factors. Lehigh University, Pennsylvania
21. Sneedon IN (1946) The distribution of stress in the neighbourhood of a crack in an elastic solid. Proc R Soc Lond A 187:229–260
22. Tada H, Paris P, Irwin G (1973, 1987) The stress analysis of cracks handbook. Del Research Corporation, St. Louis
23. Wells AA (2000) George Rankin Irwin 26 February 1907 to 9 October 1998: Elected foreign member of the Royal Society. Biogr Mems Fell R Soc 46:269–283
24. Westergaard HM (1939) Bearing pressures and cracks. J Appl Mech 49:A49–A53
25. Williams ML (1957) On the stress distribution at the base of a stationary crack. J Appl Mech 24:109–114

Part I
Interface Fracture

Chapter 2
Fundamentals of Interface Fracture Mechanics

Abstract In this chapter, the basic principles of interface fracture mechanics are presented. After a brief description of the development of interface fracture, the first term of the asymptotic expression for the stress and displacement fields in the neighborhood of an interface crack tip between two homogeneous, isotropic, linear elastic materials is presented. The energy release rate for this crack type, as well as the J-integral are described. Both deterministic and statistically obtained fracture criteria are discussed.

Keywords Complex stress intensity factor · Interface · Interface energy release rate · Interface fracture toughness · Oscillatory parameter · Oscillatory singularity · Phase angles

The first paper published on interface fracture mechanics appeared in 1959 [33]. The problem of a crack along a perfectly bonded interface between two linear elastic, homogeneous and isotropic materials was considered. It was shown that the stresses possess two singularities: a square-root singularity and an oscillatory, square-root singularity. As a result of the oscillatory singularity, the stresses oscillate ever faster as the crack tip is approached. In [29], the problem of an interface crack in a slab subjected to bending was considered. The same singularities were found as in [33] and the stress distribution in polar coordinates surrounding the crack tip was determined. Despite the unrealistic oscillatory stresses and interface interpenetration, a series of papers were written in which stress intensity factors for interface cracks were determined [8, 15, 16, 27].

As a result of this behavior, researchers ceased publishing papers on this subject until 1977. Apparently the unrealistic oscillatory stresses and the interpenetration of the crack faces near the crack tip caused this hiatus. A series of papers appeared in the late 1970s [9–11, 14] in which a physically sound assumption was made. It was assumed that a contact zone of unknown length existed behind the crack tip and along the interface. For an infinite bimaterial body composed of two isotropic materials with a finite length crack along the interface subjected to far-field tension perpendicular to the crack faces, it was found that the normalized length of the contact zone s/a, where $2a$ is the crack length, was $O(10^{-4})$ to $O(10^{-7})$ depending upon material properties [9]. For pure in-plane shear applied to the same body, one

L. Banks-Sills, *Interface Fracture and Delaminations in Composite Materials*,
SpringerBriefs in Structural Mechanics, DOI 10.1007/978-3-319-60327-8_2

normalized contact zone length is $O(10^{-7})$ and the other is about one third [10]; this occurred for Dundurs' parameter $\beta = 0.5$ [13]. For smaller values of β, the contact zone sizes will decrease. Obtaining these solutions is rather complicated.

Since the contact zones in many loading cases will be small, investigators returned to the original approach in which an oscillating singularity and crack face interpenetration were found with the assumption that the contact or interpenetration zone was small [18–20, 26, 28]. With publication of these investigations, experimental studies involving prediction of crack propagation between two dissimilar materials began to appear. Some of these studies will be discussed in Chap. 4.

2.1 Stress and Displacement Field in the Neighborhood of an Interface Crack Tip

An interface crack between two dissimilar linear elastic, homogeneous and isotropic materials is considered in this chapter (see Fig. 2.1). The first term of the asymptotic expansion of the oscillatory, square-root stress field in polar coordinates was first presented in [28]. In Cartesian coordinates, the first term of the asymptotic expansion of the in-plane stress field is given by

$$ {}_k\sigma_{\alpha\beta} = \frac{1}{\sqrt{2\pi r}} \left[\Re \left(K r^{i\varepsilon} \right) \, {}_k\Sigma^{(1)}_{\alpha\beta}(\theta) + \Im \left(K r^{i\varepsilon} \right) \, {}_k\Sigma^{(2)}_{\alpha\beta}(\theta) \right] \tag{2.1} $$

where $\alpha, \beta = 1, 2, k = 1, 2$ denotes the upper and lower materials, respectively, and the crack tip polar coordinates r and θ shown in Fig. 2.1 are given in all x_1x_2 planes normal to the crack front. It may be pointed out that only straight crack fronts are considered here. In Eq. (2.1), the symbols $\Re$ and $\Im$ denote the real and imaginary parts of the quantity in parentheses, respectively, and $i = \sqrt{-1}$. The complex stress intensity factor in Eq. (2.1) is given by

$$ K = K_1 + iK_2 \tag{2.2} $$

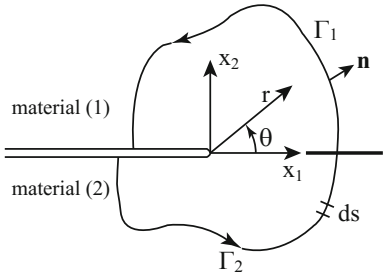

Fig. 2.1 Interface crack tip geometry

where K_1 and K_2 are real and, respectively, the modes 1 and 2 stress intensity factors. They are not associated with tension and in-plane shear stresses as they are for homogeneous bodies; hence, they are denoted with Arabic subscripts [26]. The oscillatory parameter ε is given by

$$\varepsilon = \frac{1}{2\pi} \ln\left(\frac{\kappa_1\mu_2 + \mu_1}{\kappa_2\mu_1 + \mu_2}\right) \tag{2.3}$$

where

$$\kappa_k = \begin{cases} 3 - 4\nu_k & \text{plane strain} \\ (3 - \nu_k)/(1 + \nu_k) & \text{generalized plane stress} \end{cases} \tag{2.4}$$

μ_k $(k = 1, 2)$ are the shear moduli of the upper and lower materials, respectively, and ν_k are the Poisson's ratios. In Eq. (2.1), the functions ${}_k\Sigma^{(1)}_{\alpha\beta}(\theta)$ and ${}_k\Sigma^{(2)}_{\alpha\beta}(\theta)$ may be found in [28] in polar coordinates and in [12] in Cartesian coordinates; they are presented in Appendix A. The out-of-plane stress components are given by

$${}_k\sigma_{\alpha 3} = \frac{K_{III}}{\sqrt{2\pi r}}\, {}_k\Sigma^{(III)}_{\alpha 3}(\theta)\ . \tag{2.5}$$

The mode III stress intensity factor K_{III} is associated with out-of-plane deformation; the functions ${}_k\Sigma^{(III)}_{\alpha 3}(\theta)$ may be found in [12] and Appendix A. Note that in three dimensions, the x_3-axis is normal to the in-plane axes in Fig. 2.1.

The first term of the asymptotic expression for the in-plane displacement components may be written as

$${}_k u_\alpha = \sqrt{\frac{r}{2\pi}}\left[\Re\left(K r^{i\varepsilon}\right)\ {}_kU^{(1)}_\alpha(\theta) + \Im\left(K r^{i\varepsilon}\right)\ {}_kU^{(2)}_\alpha(\theta)\right] \tag{2.6}$$

with $\alpha = 1, 2$; whereas, the out-of-plane displacement is given by

$${}_k u_3 = \sqrt{\frac{r}{2\pi}}\, K_{III}\ {}_kU^{(III)}_3(\theta)\ . \tag{2.7}$$

In Eqs. (2.6) and (2.7), the functions ${}_kU^{(1)}_\alpha(\theta)$, ${}_kU^{(2)}_\alpha(\theta)$ and ${}_kU^{(III)}_3(\theta)$ may be found in [12] and are presented in Appendix A. It may be noted that they have units of L^2/F where L is a length unit and F is force. Again, the expressions in Eqs. (2.1), (2.5)–(2.7) represent a universal solution for the stresses and displacements in the neighborhood of the crack tip.

As an example of a complex stress intensity, for a finite length crack $2a$ along the interface of two dissimilar isotropic, homogeneous materials, in an infinite body, subjected to a tensile stress σ normal to the crack faces and an in-plane shear stress τ both remote from the crack, it is found as

$$K_1 + i\,K_2 = (\sigma + i\tau)\sqrt{\pi a}(1 + 2i\varepsilon)(2a)^{-i\varepsilon}\ . \tag{2.8}$$

Note that the units of K are $FL^{-i\varepsilon}/L^{3/2}$ where F represents force and L, length. It should be noted that for all material combinations $|\varepsilon| \leq 0.175$. Moreover, the stress intensity factor may be normalized as

$$\hat{K} = K\hat{L}^{i\varepsilon} \tag{2.9}$$

where $\hat{K}$ has the usual units of stress intensity factors, namely $F/L^{3/2}$ and $\hat{L}$ is an arbitrary reference length.

2.2 Interface Energy Release Rate

Next, consider the interface energy release rate $\mathcal{G}_i$ where the subscript i represents interface. By means of Irwin's crack closure integral [21], it may be shown that the energy release rate of an interface crack is given in the form

$$\mathcal{G}_i = \frac{1}{H_1}\left(K_1^2 + K_2^2\right) + \frac{1}{H_2}K_{III}^2 \tag{2.10}$$

where

$$\frac{1}{H_1} = \frac{1}{2\cosh^2 \pi\varepsilon}\left(\frac{1}{\overline{E}_1} + \frac{1}{\overline{E}_2}\right) \tag{2.11}$$

$$\frac{1}{H_2} = \frac{1}{4}\left(\frac{1}{\mu_1} + \frac{1}{\mu_2}\right) . \tag{2.12}$$

and

$$\frac{1}{\overline{E}_k} = \begin{cases} \dfrac{1-\nu_k^2}{E_k} & \text{plane strain} \\ \dfrac{1}{E_k} & \text{generalized plane stress} \end{cases} \tag{2.13}$$

The two-dimensional version of Eq. (2.10) was first presented in [24].

Two phase angles ψ and ϕ may be defined as

$$\psi = \tan^{-1}\left[\frac{\Im\left(K\hat{L}^{i\varepsilon}\right)}{\Re\left(K\hat{L}^{i\varepsilon}\right)}\right] = \tan^{-1}\left(\frac{\sigma_{21}}{\sigma_{22}}\right)\Big|_{\theta=0, r=\hat{L}} \tag{2.14}$$

and

$$\phi = \tan^{-1}\left[\sqrt{\frac{H_1}{H_2}}\frac{K_{III}}{\sqrt{K_1^2 + K_2^2}}\right] = \tan^{-1}\left(\sqrt{\frac{H_1}{H_2}}\frac{\sigma_{23}}{\sqrt{\sigma_{22}^2 + \sigma_{21}^2}}\right)\Big|_{\theta=0, r=\hat{L}} \tag{2.15}$$

In Eq. (2.14), the units of the term $K\hat{L}^{i\varepsilon}$ are MPa$\sqrt{\text{m}}$, the ordinary units of stress intensity factors. From Eq. (2.14), at the interface ($\theta = 0$ in Fig. 2.1), ψ is a measure of the ratio between the in-plane shear and the normal stress components along the interface at a distance $\hat{L}$ from the crack tip. From Eq. (2.15), ϕ is a measure of the ratio between the out-of-plane shear stress and the in-plane stresses. It may also be noted that

$$\mathcal{G}_i = -\frac{\partial \Pi}{\partial a} \ . \tag{2.16}$$

It may be shown in two dimensions that the J-integral is given by [1]

$$J = \sum_{k=1}^{2} \int_{\Gamma_k} \left({}_kW n_1 - {}_kT_i \frac{\partial_k u_i}{\partial x_1} \right) ds \tag{2.17}$$

where $k = 1, 2$ denotes the upper and lower material, respectively, Γ_2 is a curve beginning on the lower crack face and ending at the interface, Γ_1 continues from the interface and ends on the upper crack face (see Fig. 2.1), the strain energy density

$${}_kW = \frac{1}{2} {}_k\sigma_{ij} \ {}_k\epsilon_{ij} \tag{2.18}$$

and ${}_k\epsilon_{ij}$ are the strain components in the upper and lower materials. In Eq. (2.17), n_1 is the component of the outer normal $\boldsymbol{n}$ to the curves Γ_k in the x_1-direction, ${}_kT_i$ and ${}_ku_i$ are, respectively, the traction and displacement vectors on Γ_k, x_1 is the coordinate shown in Fig. 2.1 and ds is the differential arc length along Γ_k. It may be shown that

$$J = \mathcal{G}_i \ . \tag{2.19}$$

Hence, the relation between $\mathcal{G}_i$ and the stress intensity factors in Eq. (2.10) holds for J.

2.3 Fracture Criterion

Fracture will occur when

$$\mathcal{G}_i = \mathcal{G}_{ic} \tag{2.20}$$

where $\mathcal{G}_{ic}$ is the interface fracture toughness or the critical interface energy release rate. It is possible to rewrite Eq. (2.10) as

$$\mathcal{G}_i = \frac{1}{H_1} \left(\hat{K}_1^2 + \hat{K}_2^2 \right) + \frac{1}{H_2} K_{III}^2 \tag{2.21}$$

where the normalized complex stress intensity factor $\hat{K}$ is defined in Eq. (2.9). Equation (2.21) may be manipulated as

$$\mathcal{G}_i = \mathcal{G}_1 \left(1 + \tan^2 \psi\right) \left(1 + \tan^2 \phi\right) \tag{2.22}$$

where

$$\mathcal{G}_1 \equiv \frac{\hat{K}_1^2}{H_1} \,. \tag{2.23}$$

When

$$\mathcal{G}_1 = \mathcal{G}_{1c} \tag{2.24}$$

where $\mathcal{G}_{1c}$ is the mode 1 critical energy release rate, the interface crack will propagate. From Eqs. (2.20), (2.22) and (2.24), the fracture criterion is given by

$$\mathcal{G}_{ic} = \overline{\mathcal{G}}_{1c} \left(1 + \tan^2 \psi\right) \left(1 + \tan^2 \phi\right) \tag{2.25}$$

where $\overline{\mathcal{G}}_{1c}$ is the average mode 1 critical energy release rate. When carrying out tests, the value of $\hat{K}_1$ is calculated for each test. Its value is substituted into Eq. (2.23) and an average value of $\mathcal{G}_{1c}$, $\overline{\mathcal{G}}_{1c}$, is found and used in Eq. (2.25). This criterion was presented for two dimensions in [4] and in three dimensions in [7]. In two dimensions, $\phi = 0$ in Eq. (2.25). It may be noted that Eq. (2.25) implies that the toughness is symmetric with respect to the phase angles ψ and ϕ. There are other investigations in the literature where a lack of symmetry about the phase angle ψ was considered [22, 30, 31].

In two dimensions, a typical failure curve, Eq. (2.25) with $\phi = 0$, is illustrated in Fig. 2.2. To employ the curve for a particular delamination in a structure with the same interface, an analysis of the structure is carried out to determine the values of the interface energy release rate $\mathcal{G}_i$ and the phase angle ψ for the value of $\hat{L}$ used to plot the curve. If for the calculated value of ψ, $\mathcal{G}_i$ is below the curve, it may be assumed that the structure will not fail. If it is above, it may be assumed that failure will occur. Note that ψ is a function of $\hat{L}$ as may be seen in Eq. (2.14). A change in $\hat{L}$ translates the abscissa in Fig. 2.2.

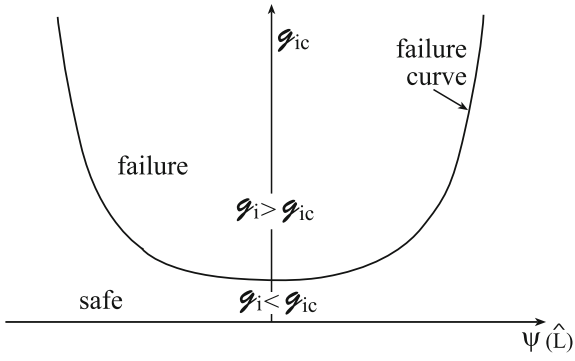

Fig. 2.2 Typical two-dimensional failure curve from Eq. (2.25) with $\phi = 0$

When testing a group of specimens, it has been observed that there is scatter about this curve [5, 6]. Hence, a probability analysis was proposed in [2, 3]. To this end, it is possible to ask the question: what is the chance that 10% of delaminations for a particular interface will unexpectedly fail with a value below the failure curve? One may propose that the average mode 1 energy release rate is decreased by a factor proportional to its standard deviation s. To this end, one may write that

$$\mathcal{G}_{1c}^{*} = \overline{\mathcal{G}}_{1c} - Ks \tag{2.26}$$

where $\overline{\mathcal{G}}_{1c}$ is the average value of $\mathcal{G}_{1c}$ and K is a statistical factor. The reduced failure curve in two dimensions is given by

$$\mathcal{G}_{ic}^{*} = \mathcal{G}_{1c}^{*}\left(1 + \tan^2\psi\right) \ ; \tag{2.27}$$

the three-dimensional reduced failure surface is given by

$$\mathcal{G}_{ic}^{*} = \mathcal{G}_{1c}^{*}\left(1 + \tan^2\psi\right)\left(1 + \tan^2\phi\right) \ . \tag{2.28}$$

In order to utilize the probabilistic failure curves, a statistical model is required. Two models were employed: one makes use of a t-distribution for statistical intervals [23, 32] and the other uses the standard variate to determine a probability and confidence interval [25].

For the statistical intervals, a one sided t-statistic was chosen with a 10% probability of unexpected failure. Thus,

$$K = t_{0.1,N-1}\sqrt{1 + \frac{1}{N}} \tag{2.29}$$

where 0.1 represents the 10% probability, N is the number of samples tested, $N - 1$ is the number of degrees of freedom and the term $1/N$ in the square-root accounts for the variability of $\overline{\mathcal{G}}_{1c}$. The value of t is tabulated for different probabilities (in this case 0.1) for $N - 1$ degrees of freedom (see for example [17] p. 367). This is equivalent to a 90% probability that each successive observation of the pair $(\mathcal{G}_i, \psi)$ will be less than the indicated value of $(\mathcal{G}_{ic}^{*}, \psi)$ and not fail.

In the second method,

$$K \simeq \frac{|z_P| + \sqrt{z_P^2 - ab}}{a} \tag{2.30}$$

where

$$a = 1 - \frac{z_\gamma^2}{2(N-1)} \qquad \text{and} \qquad b = z_P^2 - \frac{z_\gamma^2}{N} \ . \tag{2.31}$$

In Eqs. (2.30) and (2.31), z_P is the standard variate with a probability P and γ is the confidence. If we chose $P = 0.1$ and $\gamma = 0.95$, then there will only be a

10% probability that a value of $\mathcal{G}_{ic}$ will be obtained below the failure curve with a confidence of 95%.

In Chap. 4, test results will be presented and use will be made of the criteria in Eq. (2.25) with $\phi = 0$ and Eq. (2.27).

References

1. Atkinson C (1977) On quasistatic problems of cracks in a non-homogeneous elastic layer. Acta Mech 26:103–113
2. Banks-Sills L (2014) Review on interface fracture and delamination of composites. Strain 50:98–110
3. Banks-Sills L (2015) Interface fracture mechanics - theory and experiment. Int J Fract 191:131–146
4. Banks-Sills L, Ashkenazi D (2000) A note on fracture criteria for interface fracture. Int J Fract 103:177–188
5. Banks-Sills L, Travitzky N, Ashkenazi D, Eliasi R (1999) A methodology for measuring interface fracture toughness of composite materials. Int J Fract 99:143–161
6. Banks-Sills L, Travitzky N, Ashkenazi D (2000) Interface fracture properties of a bimaterial ceramic composite. Mech Mater 32:711–722
7. Banks-Sills L, Konovalov N, Fliesher A (2010) Comparison of two and three-dimensional analyses of interface fracture data obtained from Brazilian disk specimens. Int J Struct Integr 1:20–42
8. Cherepanov GP (1962) The stress state in a heterogeneous plate with slits. Iz AN SSSR, OTN, Mekhan i Mashin, in Russian 1:131–137
9. Comninou M (1977) The interface crack. J Appl Mech 44:631–636
10. Comninou M (1978) The interface crack in a shear field. J Appl Mech 45:287–290
11. Comninou M, Schmueser D (1979) The interface crack in a combined tension-compression and shear field. J Appl Mech 46:345–348
12. Deng X (1993) General crack-tip fields for stationary and steadily growing interface cracks in anisotropic bimaterials. J Appl Mech 60:183–189
13. Dundurs J (1969) Discussion: edge-bonded dissimilar orthogonal elastic wedges under normal and shear loading. J Appl Mech 36:650–652
14. Dundurs J, Comninou M (1979) Some consequences of the inequality conditions in contact and crack problems. J Elast 9:71–82
15. England AH (1965) A crack between dissimilar media. J Appl Mech 32:400–402
16. Erdogan F (1965) Stress distribution in bonded dissimilar materials with cracks. J Appl Mech 32:403–410
17. Freund JE (1963) Mathematical statistics. Prentice-Hall Inc., Englewood Cliffs
18. Hutchinson JW (1990) Mixed mode fracture mechanics of interfaces. In: Rühle M, Evans AG, Ashby MF, Hirth JP (eds) Metal ceramic interfaces. Pergamon Press, Oxford, pp 295–301
19. Hutchinson JW, Suo Z (1991) Mixed mode cracking in layered materials. In: Hutchinson JW, Wu TY (eds) Advances in applied mechanics, vol 29. Academic Press, California, pp 64–191
20. Hutchinson JW, Mear ME, Rice JR (1987) Crack paralleling an interface between dissimilar materials. J Appl Mech 54:828–832
21. Irwin GR (1958) Fracture. In: Flügge S (ed) Handbuch der physik, vol VI. Springer, Germany, pp 551–590
22. Liang YM, Liechti KM (1995) Toughening mechanisms in mixed-mode interfacial fracture. Int J Solids Struct 32:957–978
23. Luko SN, Neubauer DV (2011) Statistical intervals-Part 2: the prediction interval. Stand News, Sept/Oct, pp 14–15

24. Malyshev BM, Salganik RL (1965) The strength of adhesive joints using the theory of fracture. Int J Fract Mech 1:114–128
25. Natrella MG (1963) Experimental statistics. In: National bureau of standards handbook 91, Washington DC, pp 2-13–2-15
26. Rice JR (1988) Elastic fracture mechanics concepts for interfacial cracks. J Appl Mech 55:98–103
27. Rice JR, Sih GC (1965) Plane problems of cracks in dissimilar media. J Appl Mech 32:418–423
28. Rice JR, Suo Z, Wang JS (1990) Mechanics and thermodynamics of brittle interfacial failure in bimaterial systems. In: Rühle M, Evans AG, Ashby MF, Hirth JP (eds) Metal ceramic interfaces. Pergamon Press, Oxford, pp 269–294
29. Sih GC, Rice JR (1964) The bending of plates of dissimilar materials with cracks. J Appl Mech 31:477–482
30. Swadener JG, Liechti KM (1998) Asymmetric shielding mechanisms in the mixed-mode fracture of a glass/epoxy interface. J Appl Mech 65:25–29
31. Swadener JG, Liechti KM, de Lozanne AL (1999) The intrinsic toughness and adhesion mechanism of a glass/epoxy interface. J Mech Phys Solids 47:223–258
32. Whitmore GA (1986) Prediction limits for a univariate normal observation. Am Stat 40:141–143
33. Williams ML (1959) The stresses around a fault or crack in dissimilar media. Bull Seismol Soc Am 49:199–204

Chapter 3
Calculation of Stress Intensity Factors – An Interface Crack

Abstract In this chapter, aspects of the finite element method for obtaining the displacement field of a body containing an interface crack are described. Square-root singular, quarter-point elements in two and three dimensions will be presented. Once the displacement field is found three methods are suggested for computing stress intensity factors; they include the displacement extrapolation (DE) method, the conservative interaction energy integral or M-integral, and the Virtual Crack Closure Technique (VCCT). The stress intensity factors are then employed to obtain the interface energy release rate and two phase angles.

Keywords Displacement extrapolation method · Finite element method · M-integral · Quarter-point element · Shape functions · Thermal residual stresses · Virtual crack closure technique

In order to predict catastrophic failure of an interface crack, knowledge of the stress intensity factors is required. The J-integral in Eq. (2.17) may be computed numerically; but its result is related to the sum of the squares of the stress intensity factors by means of Eqs. (2.19) and (2.10). Hence, methods are required to calculate the stress intensity factors independently. Moreover, in this book, the finite element method is suggested for determining the displacement field. Use of the finite element method for interface cracks will be presented in Sect. 3.1. With this field, three methods will be described for obtaining stress intensity factors; they are the DE method which is discussed in Sect. 3.2; the M-integral which is discussed in Sect. 3.3; and VCCT which is discussed in Sect. 3.4.

3.1 Finite Element Method

As seen in Chap. 1, the stresses in the neighborhood of a crack tip or crack front in a homogeneous isotropic material are square-root singular. There have been many special elements developed to model this behavior. These were described in [2]. Quarter-point square and brick elements for two and three-dimensional geometries, respectively, have been found to produce excellent results. A review of these elements is also presented in [2, 3].

L. Banks-Sills, *Interface Fracture and Delaminations in Composite Materials*,
SpringerBriefs in Structural Mechanics, DOI 10.1007/978-3-319-60327-8_3

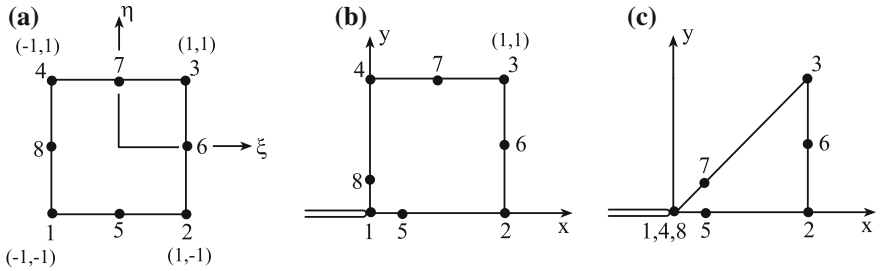

Fig. 3.1 Eight noded **a** parent element in the $\xi\eta$ plane and **b** quarter-point element in the xy plane. **c** Quarter-point collapsed triangular element

For the h-version of finite elements that is considered here, an isoparametric element is employed in which both displacement and coordinate vectors $\mathbf{u}$ and $\mathbf{x}$, respectively, are expressed in terms of the same shape functions N_i, namely

$$\mathbf{u} = \sum_{i=1}^{m} N_i \mathbf{u}_i \qquad \mathbf{x} = \sum_{i=1}^{m} N_i \mathbf{x}_i \ . \tag{3.1}$$

In Eq. (3.1), the displacement vector and coordinate vector in the physical space are either two or three-dimensional vectors; in two dimensions, $\mathbf{u}^T = [u, v]$ and $\mathbf{x}^T = [x, y]$; in three dimensions, $\mathbf{u}^T = [u, v, w]$ and $\mathbf{x}^T = [x, y, z]$. The number of nodal points in an element is m. In two dimensions, the shape functions N_i for an eight noded element ($m = 8$) are given by

$$N_i(\xi, \eta) = \frac{1}{4}\left[(1+\xi\xi_i)(1+\eta\eta_i) - \left(1-\xi^2\right)(1+\eta\eta_i) - (1+\xi\xi_i)\left(1-\eta^2\right)\right]\xi_i^2\eta_i^2$$
$$+\frac{1}{2}\left(1-\xi^2\right)(1+\eta\eta_i)\left(1-\xi_i^2\right)\eta_i^2 + \frac{1}{2}(1+\xi\xi_i)\left(1-\eta^2\right)\left(1-\eta_i^2\right)\xi_i^2 \tag{3.2}$$

where (ξ, η) are the coordinates in the parent element as shown in Fig. 3.1a and (ξ_i, η_i) are the coordinates of the ith nodal point. If the nodes closest to the crack tip in the physical element are moved to the quarter-point as illustrated in Fig. 3.1b, it has been proven that the strains are square-root singular along all rays emanating from the crack tip [4, 24]. It may be noted that the singularity is in a small region of the element near the crack tip, extending along the entire length of the element sides. For either a quarter-point, collapsed triangular element illustrated in Fig. 3.1c which uses the shape functions in Eq. (3.2) or a natural triangle, it was shown that the singularity extends along the diagonal ray emanating from the crack tip [11, 12]. The proof may be easily extended to include all rays emanating from the crack tip. Hence, the triangular element has a distinct advantage over the square or quadrilateral, quarter-point element. Since at that time, meshing and remeshing was more difficult than it is today, in [2] only quadrilateral, quarter-point elements were considered. Moreover,

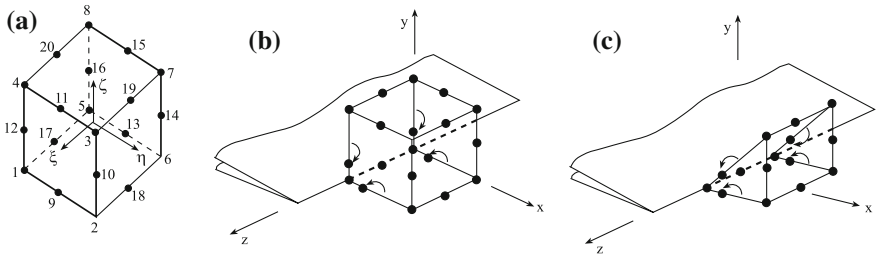

Fig. 3.2 Twenty noded **a** parent element in the $\xi\eta\zeta$ space and **b** quarter-point element in the xyz space. **c** Quarter-point collapsed prismatic element

square elements at the crack tip are preferred, since quadrilateral elements have been shown to disturb the singular region.

For three-dimensional, 20-noded brick elements, the shape functions are given by

$$\begin{aligned} N_i(\xi,\eta,\zeta) = & \frac{1}{8}\,(1+\xi\xi_i)\,(1+\eta\eta_i)\,(1+\zeta\zeta_i)\,(\xi\xi_i+\eta\eta_i+\zeta\zeta_i-2)\,\xi_i^2\eta_i^2\zeta_i^2 \\ & +\frac{1}{4}\,\left(1-\xi^2\right)(1+\eta\eta_i)\,(1+\zeta\zeta_i)\left(1-\xi_i^2\right) \\ & +\frac{1}{4}\,(1+\xi\xi_i)\left(1-\eta^2\right)(1+\zeta\zeta_i)\left(1-\eta_i^2\right) \\ & +\frac{1}{4}\,(1+\xi\xi_i)\,(1+\eta\eta_i)\left(1-\zeta^2\right)\left(1-\zeta_i^2\right) \end{aligned} \tag{3.3}$$

where (ξ,η,ζ) are the coordinates in the parent element as shown in Fig. 3.2a, (ξ_i,η_i,ζ_i) are the coordinates of the ith node in the parent element. Equation (3.1) may be employed in three-dimensions with the displacement vector $\mathbf{u}^T=[u,v,w]$ and the coordinate $\mathbf{x}^T=[x,y,z]$. For a twenty noded element, $m=20$.

It has been shown that the behavior of the strains within a twenty-noded brick quarter-point element shown in Fig. 3.2b are square-root singular within each xy-plane orthogonal to the crack front in a manner similar to that of the quadrilateral element. It is emphasized that the sides of the elements must be parallel to each other and orthogonal to the crack front to obtain this behavior. Moreover, although there are no nodal points within the element, the strains are square-root singular not only on the outer surfaces of the elements but also within each plane orthogonal to the crack front! For further details, see [7]. Finally, collapsed wedge elements using the same shape functions in Eq. (3.3) and shown in Fig. 3.2c may be considered. The analogous proof for the two-dimensional element was used in [12] to show that there is square-root singular behavior along the diagonal ray on the two outer xy-surfaces of the element. It may be shown that this occurs for all rays emanating from the crack front within all orthogonal xy-planes within the element (see Fig. 3.2c). Hence, in this case, the quarter-point, collapsed, prismatic elements appear to have

an advantage over the quarter-point, brick elements. It may be noted that meshes should be designed such that the elements are normal to the crack front and crack faces.

Although the stress components for an interface crack possess an oscillatory, square-root singularity, the elements presented here for homogeneous material are recommended for an interface crack. The dominant part of the singularity is square-root and these elements have been found to produce excellent results.

3.2 Displacement Extrapolation Method

The displacement extrapolation method was first presented in [15] for isotropic bodies subjected to modes I and II deformation. Because of its simplicity, it has been used widely in the literature. With mixed modes and homogeneous material, mode decoupling is immediate. For all material types, use is made of the crack opening displacements, namely

$$\Delta u_i(r) = {}_1u_i(r, \theta = \pi) - {}_2u_i(r, \theta = -\pi) \ . \tag{3.4}$$

In Eq. (3.4), u_i $(i = 1, 2, 3)$ are the displacement components in the x_i-directions and the left subscripts 1 and 2 denote, for an interface crack, the upper and lower materials, respectively.

For an interface crack between two dissimilar linear elastic, isotropic, homogeneous materials, using Eq. (3.4), as well as the first term of the asymptotic expansion of the displacement field in Eqs. (2.6) and (2.7) and the expressions in Eqs. (A.9)–(A.13), one may write that

$$\Delta u_2(r) + i\,\Delta u_1(r) = \frac{8\cosh \pi\varepsilon}{H_1(1+2i\varepsilon)}\sqrt{\frac{r}{2\pi}}\ K r^{i\varepsilon} \ , \qquad \Delta u_3(r) = \frac{8}{H_2}\sqrt{\frac{r}{2\pi}}\ K_{III} \ . \tag{3.5}$$

where ε, H_1 and H_2 are given, respectively, in Eqs. (2.3), (2.11) and (2.12). Solving for the complex stress intensity factor in Eq. $(3.5)_1$ and the mode III stress intensity factor in Eq. $(3.5)_2$, one obtains

$$K_1^*(r) = \frac{\sqrt{2\pi(1+4\varepsilon^2)}}{8\cosh \pi\varepsilon} H_1 \left\{ \cos\chi\ \frac{\Delta u_2(r)}{\sqrt{r}} - \sin\chi\ \frac{\Delta u_1(r)}{\sqrt{r}} \right\} \tag{3.6}$$

$$K_2^*(r) = \frac{\sqrt{2\pi(1+4\varepsilon^2)}}{8\cosh \pi\varepsilon} H_1 \left\{ \sin\chi\ \frac{\Delta u_2(r)}{\sqrt{r}} + \cos\chi \frac{\Delta u_1(r)}{\sqrt{r}} \right\} \tag{3.7}$$

$$K_{III}^*(r) = \frac{\sqrt{2\pi}\ H_2}{8}\ \frac{\Delta u_3}{\sqrt{r}} \tag{3.8}$$

where the starred quantities are local stress intensity factors depending on distance from the crack tip along the crack faces. In Eqs. (3.6) and (3.7),

$$\chi = \tan^{-1} 2\varepsilon - \varepsilon \ln r \ . \tag{3.9}$$

The displacement jumps $\Delta u_1(r)$, $\Delta u_2(r)$ and $\Delta u_3(r)$ are taken from the finite element results along rays orthogonal to the crack front along the crack faces in the x_i-directions, respectively.

In [18], the full series for the stress and displacement fields of an interface crack between two isotropic materials was presented. Focusing on the displacements, for the oscillatory, square-root singularity and the square-root singularity, terms of the type r^n, where $n = 1, 2, 3 \ldots$ were found. For these terms, the displacement vanishes along the crack faces. Therefore, along the crack faces, the displacement jumps are found to behave as

$$\Delta u_2 + i\, \Delta u_1 = A_1 r^{1/2+i\varepsilon} + A_2 r^{3/2+i\varepsilon} + O\left(r^{5/2+i\varepsilon}\right) \tag{3.10}$$

$$\Delta u_3 = B_1 r^{1/2} + B_2 r^{3/2} + O\left(r^{5/2}\right) \tag{3.11}$$

where A_1 and A_2 are complex constants, and B_1 and B_2 are real constants. The terms $r^{(2n+1)/2+i\varepsilon}$ in Eq. (3.10) and $r^{(2n+1)/2}$ in Eq. (3.11) are obtained from the general solution of the crack eigenvalue problem. Dividing Eqs. (3.10) and (3.11) by $r^{1/2+i\varepsilon}$ and $r^{1/2}$, respectively, leads to linear behavior of the local stress intensity factors for a range of r in the neighborhood of the crack tip. To proceed with the method, the local stress intensity factors given in Eqs. (3.6)–(3.8) are plotted along the crack faces as shown in Fig. 3.3 for K_1 for increasing values of the r-coordinate. These values are extrapolated to zero, so that

$$K_1 = \lim_{r\to 0} K_1^*, \qquad K_2 = \lim_{r\to 0} K_2^*, \qquad K_{III} = \lim_{r\to 0} K_{III}^* \ . \tag{3.12}$$

With the values of K_m^* ($m = 1, 2, III$) along the crack front, linear regression may be employed to determine a 'best' straight line. Nonetheless, judgement must be used in choosing the K value.

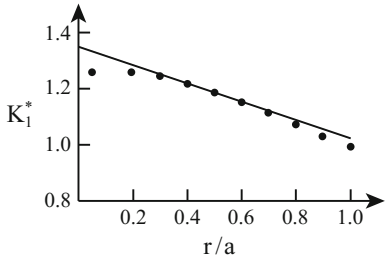

Fig. 3.3 Illustration of the displacement extrapolation method; local stress intensity factor K_1^* as a function of the normalized distance from the crack tip

3.3 M-Integral

The two-dimensional conservative J-integral for an interface crack is given in Eq. (2.17). As a result of the relation between J and $\mathcal{G}_i$ in Eq. (2.19) and the stress intensity factors in Eq. (2.10), it is not possible to obtain the values of each stress intensity factor separately with knowledge of J. However, the conservative interaction energy or M-integral developed in [16] and implemented in [40] for a crack in a homogeneous, isotropic material allows determination of the stress intensity factors. This method was extended to interface cracks in [39]. First the two-dimensional version of this integral is presented and then the three-dimensional version. Both mechanical and thermal integrals will be described.

3.3.1 Two Dimensions

To obtain the stress intensity factors, two solutions which satisfy equilibrium in the cracked body are superposed, namely,

$$\sigma_{ij} = \sigma_{ij}^{(1)} + \sigma_{ij}^{(2)} \tag{3.13}$$

$$\epsilon_{ij} = \epsilon_{ij}^{(1)} + \epsilon_{ij}^{(2)} \tag{3.14}$$

$$u_i = u_i^{(1)} + u_i^{(2)} \ . \tag{3.15}$$

Solution (1) is the sought after solution which is obtained numerically by means of the finite element method. Solution (2) is an auxiliary solution which is given by the first term of the asymptotic expansion of the field quantities related to the material under consideration. These solutions will be described in the sequel. Since superposition is employed in Eqs. (3.13)–(3.15) only linear elastic material may be considered. The in-plane stress intensity factors are given by

$$K_1 = K_1^{(1)} + K_1^{(2)} \tag{3.16}$$

$$K_2 = K_2^{(1)} + K_2^{(2)} \ . \tag{3.17}$$

The stress intensity factors related to solution (1) are those to be determined from the M-integral. Those related to solution (2) are chosen judiciously as will be described.

First, the J-integral in Eq. (2.17) may be converted into an area integral as [27]

$$J = \sum_{k=1}^{2} \int_{A_k} \left[{}_k\sigma_{ij} \frac{\partial_k u_i}{\partial x_1} - {}_k W n_1 \delta_{1j} \right] \frac{\partial q_1}{\partial x_j} \, dA \ . \tag{3.18}$$

In Eq. (3.18), $k = 1, 2$ represents the upper and lower materials respectively, indicial notation is used for the indices i and j but not k, $i, j = 1, 2$, A_k is the annular region shown in Fig. 3.4, q_1 is continuously differentiable within A_k, is unity on ${}_kC_1$

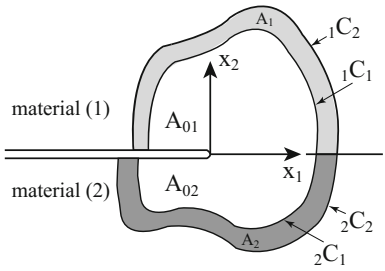

Fig. 3.4 Areas A_1 and A_2 for calculating the mechanical M-integral for an interface crack. Additional areas A_{01} and A_{02} for calculating the thermal M-integral

and vanishes on ${}_kC_2$. For a finite element analysis, A_k is chosen as a single ring of elements and

$$q_1 \;=\; \sum_{i=1}^{8} N_i(\xi,\eta)\, q_{1i} \tag{3.19}$$

where the eight noded, isoparametric element in Fig. 3.1a is employed in two dimensions. In Eq. (3.19), $N_i(\xi,\eta)$ are the shape functions and ξ and η are the coordinates in the parent element. The vector q_{1i} is chosen to fulfill the requirements already defined for q_1 with the additional restriction that the nodal points of the element are mapped in such a way that mid-point nodes remain in their respective positions in the mapped configuration as described in [8]. If integration takes place through the quarter-point elements, then q_{1i} is chosen so that the quarter-point nodes remain in that position in the mapped configuration. The last restrictions increase accuracy. It may be noted that $\Delta\ell q_1$ is actually a mapping of the physical element, where $\Delta\ell$ is a virtual crack extension; so that q_1 is a normalized virtual crack extension.

By substituting Eqs. (3.13)–(3.15) into the area J-integral in Eq. (3.18), it is possible to derive the M-integral as [9]

$$M^{(1,2)} \;=\; \sum_{k=1}^{2} \int_{A_k} \left[{}_k\sigma_{ij}^{(1)}\, \frac{\partial_k u_i^{(2)}}{\partial x_1} \;+\; {}_k\sigma_{ij}^{(2)}\, \frac{\partial_k u_i^{(1)}}{\partial x_1} \;-\; {}_kW^{(1,2)}\, \delta_{1j} \right] \frac{\partial q_1}{\partial x_j}\, dA \;. \tag{3.20}$$

It may be pointed out that earlier Yau et al. [40] used the line J-integral to derive a line M-integral. Since it was shown in [2] that the area J-integral has superior path independence than that of the line integral, the M-integral will be presented here only as an area integral. In Eq. (3.20), indicial notation is employed and δ is the Kronecker delta. The mutual strain energy density ${}_kW^{(1,2)}$ of the two solutions is given by

$${}_kW^{(1,2)} \;=\; {}_k\sigma_{ij}^{(1)}\, {}_k\epsilon_{ij}^{(2)} = {}_k\sigma_{ij}^{(2)}\, {}_k\epsilon_{ij}^{(1)} \;. \tag{3.21}$$

On the other hand, if one substitutes the expressions for the stress intensity factors in Eqs. (3.16) and (3.17) into (2.10) with $K_{III} = 0$, it is possible to show that

$$M^{(1,2)} \;=\; \frac{2}{H_1} \left[K_1^{(1)} K_1^{(2)} + K_2^{(1)} K_2^{(2)} \right] . \tag{3.22}$$

In Eq. (3.22), H_1 is defined in Eq. (2.11).

Two auxiliary solutions are required in order to determine both $K_1^{(1)}$ and $K_2^{(1)}$ for this problem. These are denoted as solutions $(2a)$ and $(2b)$. For auxiliary solution $(2a)$, choose

$$K_1^{(2a)} = 1 \qquad K_2^{(2a)} = 0 \; . \tag{3.23}$$

These may be substituted into the first term of the asymptotic solution for the displacement components of a crack along the interface between two dissimilar linearly elastic, homogeneous and isotropic materials given in Eq. (2.6). Recall that the functions ${}_kU_\alpha^{(1)}(\theta)$ and ${}_kU_\alpha^{(2)}(\theta)$ are given in Appendix A in Eqs. (A.9)–(A.12). For solution $(2b)$

$$K_1^{(2b)} = 0 \qquad K_2^{(2b)} = 1 \; . \tag{3.24}$$

For solution $(2a)$,

$$M^{(1,2a)} = \sum_{k=1}^{2} \int_{A_k} \left[{}_k\sigma_{ij}^{(1)} \frac{\partial_k u_i^{(2a)}}{\partial x_1} + {}_k\sigma_{ij}^{(2a)} \frac{\partial_k u_i^{(1)}}{\partial x_1} - {}_k W^{(1,2a)} \, \delta_{1j} \right] \frac{\partial q_1}{\partial x_j} \, dA \; . \tag{3.25}$$

In Eq. (3.25), the displacement derivatives, strain and stress components for solution (1) are obtained by means of a finite element formulation using the displacement components determined at the nodal points of a finite element formulation. The displacement derivatives, strain and stress components for solution $(2a)$ are obtained by means of a finite element formulation using the displacement components determined at the nodal points from Eqs. (2.6) and (3.23). With these values, the integral in Eq. (3.25) is evaluated. Substituting Eq. (3.23) into (3.22) leads to

$$M^{(1,2a)} = \frac{2}{H_1} \, K_1^{(1)} \; . \tag{3.26}$$

The stress intensity factor $K_1^{(1)}$ is determined by equating Eqs. (3.25) and (3.26).

In a similar manner, the mode 2 stress intensity factor $K_2^{(1)}$ may be found. Specifically,

$$M^{(1,2b)} = \sum_{k=1}^{2} \int_{A_k} \left[{}_k\sigma_{ij}^{(1)} \frac{\partial_k u_i^{(2b)}}{\partial x_1} + {}_k\sigma_{ij}^{(2b)} \frac{\partial_k u_i^{(1)}}{\partial x_1} - {}_k W^{(1,2b)} \, \delta_{1j} \right] \frac{\partial q_1}{\partial x_j} \, dA \tag{3.27}$$

and substitution of Eq. (3.24) into (3.22) yields

$$M^{(1,2b)} = \frac{2}{H_1} \, K_2^{(1)} \; . \tag{3.28}$$

The integral in Eq. (3.27) is carried out and Eqs. (3.27) and (3.28) are equated.

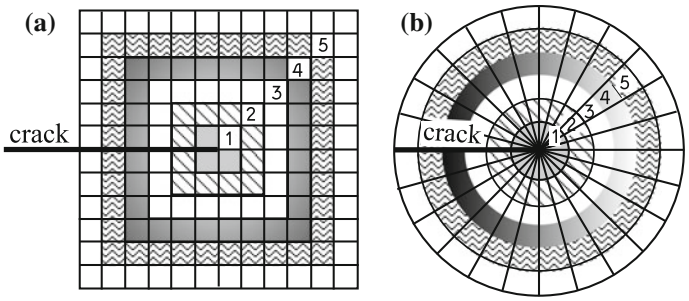

Fig. 3.5 Mesh and integration paths about the crack tip for **a** *square* elements and **b** *triangular* elements about the crack tip

The integrals in Eqs. (3.25) and (3.27) are calculated element by element within a ring of elements as shown in Fig. 3.5. In Fig. 3.5a, five rings are shown for square elements; whereas, in Fig. 3.5b, five rings are shown with triangular elements surrounding the crack tip. For solution (1), a finite element calculation yields the displacement vector at the nodal points. The necessary displacements, stresses and strains are computed at the integration points by means of a finite element scheme. For solution (2), the analytical solution for the displacement field is calculated at the nodal points. These are also used to obtain the field quantities at the integration points by means of a finite element scheme. After calculating the integrals in Eqs. (3.25) and (3.27), $K_1^{(1)}$ and $K_2^{(1)}$ are found by equating (3.26) to (3.25), and (3.28) to (3.27). Note that only the displacement field is required.

Next, the thermal M-integral is presented. It has been used to obtain stress intensity factors resulting from thermal stresses and may be used for general thermal problems. Note that the stresses in the neighborhood of a crack tip have the same singularity as that for mechanical loading. A thermal J-integral was presented in [38]. To this end, a strain energy density must be chosen. In [5] it was chosen as

$$ {}_kW_F = \frac{1}{2}\,{}_k\sigma_{ij}\;{}_k\epsilon_{ij} - \frac{1}{2}\,\vartheta_k\;\beta_{ij}^k\;{}_k\epsilon_{ij} \tag{3.29} $$

where ${}_kW_F$ is the strain energy density in [21], ${}_k\epsilon_{ij}$ is the total strain of the upper and lower materials, respectively, comprising the mechanical and thermal strain components, ϑ_k is the temperature change in material k and may be a function of position,

$$ \beta_{ij}^k = \tilde{\beta}_k \delta_{ij} \tag{3.30} $$

and

$$ \tilde{\beta}_k = \begin{cases} \dfrac{E_k \alpha_k}{1-2\nu_k} & \text{plane strain} \\ \dfrac{E_k \alpha_k}{1-\nu_k} & \text{generalized plane stress .} \end{cases} \tag{3.31} $$

In Eq. (3.31), α_k is the coefficient of thermal expansion (CTE) of the upper and lower materials. Since

$$\sigma_{ij} = \frac{\partial W_F}{\partial \epsilon_{ij}} \,, \tag{3.32}$$

it may be shown that the stress/strain relation is given by

$${}_k\sigma_{ij} = 2\mu_k \, {}_k\epsilon_{ij} + \lambda_k \, {}_k\epsilon_{ss}\delta_{ij} - \tilde{\beta}_k \vartheta_k \delta_{ij} \tag{3.33}$$

where μ_k and λ_k are the Lamé constants of the upper and lower materials.

The thermal M-integral may be written as [5]

$$\begin{aligned} M^{(1,2)} = \sum_{k=1}^{2} \int_{A_k} \left({}_k\sigma_{ij}^{(1)} \frac{\partial_k u_i^{(2)}}{\partial x_1} + {}_k\sigma_{ij}^{(2)} \frac{\partial_k u_i^{(1)}}{\partial x_1} - {}_k W_F^{(1,2)} \delta_{1j} \right) \frac{\partial q_1}{\partial x_j} \, dA \\ + \sum_{k=1}^{2} \beta_{ij}^k \int_{A_k} {}_k\epsilon_{ij}^{(2)} \frac{\partial \vartheta_k^{(1)}}{\partial x_1} \, q_1 \, dA + \sum_{k=1}^{2} \beta_{ij}^k \int_{A_{0k}} {}_k\epsilon_{ij}^{(2)} \frac{\partial \vartheta_k^{(1)}}{\partial x_1} \, dA \,. \end{aligned} \tag{3.34}$$

The areas A_k and A_{0k} are shown in Fig. 3.4. The interaction strain energy density is given by

$${}_k W_F^{(1,2)} = {}_k\sigma_{ij}^{(1)} \, {}_k\epsilon_{ij}^{(2)} = {}_k\sigma_{ij}^{(2)} \, {}_k\epsilon_{ij}^{(1)} - \beta_{ij}^k \vartheta_k^{(1)} \, {}_k\epsilon_{ij}^{(2)} \tag{3.35}$$

where the auxiliary solution for the temperature change $\vartheta_k^{(2)}$ is taken to be zero. Hence, the auxiliary solution remains the same as for that of the mechanical solution. In addition to Eq. (3.34), Eq. (3.22) is also used in the calculation. As described for the mechanical M-integral, the stress intensity factors are obtained by means of Eqs. (3.26) and (3.28). If $\vartheta_k^{(1)}$ is not a function of x_1, the thermal M-integral takes the form of the mechanical M-integral with ${}_k W^{(1,2)}$ replaced with ${}_k W_F^{(1,2)}$ and the constitutive law in Eq. (3.33) prevailing. Finally, it may be noted that if $\vartheta_k^{(1)} = 0$, then Eqs. (3.34) and (3.35) revert to the mechanical M-integral with the constitutive relation in Eq. (3.33) becoming that for an isothermal problem.

3.3.2 Three Dimensions

In [27, 29, 34], the mechanical M-integral was extended to three dimensions; it was implemented in [20, 22] for interface cracks. In [10, 34], the thermal M-integral was extended to three dimensions.

In both cases, to the superposition conditions in Eqs. (3.13)–(3.17) is added

$$K_{III} = K_{III}^{(1)} + K_{III}^{(2)} \,. \tag{3.36}$$

Table 3.1 Stress intensity factors for the auxiliary solutions

2α	$K_1^{(2\alpha)}$	$K_2^{(2\alpha)}$	$K_{III}^{(2\alpha)}$
$2a$	1	0	0
$2b$	0	1	0
$2c$	0	0	1

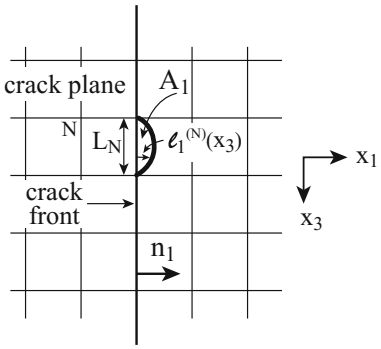

Fig. 3.6 Virtual crack extension along the crack front denoted on the finite element mesh

Since there are three unknown stress intensity factors $K_1^{(1)}$, $K_2^{(1)}$ and $K_{III}^{(1)}$, there are three auxiliary solutions. The latter are determined from the first term of the asymptotic displacement components in Eqs. (2.6) and (2.7). The values of the stress intensity factors for the three auxiliary solutions $(2a)$, $(2b)$ and $(2c)$ are defined in Table 3.1.

For a straight crack front as in Fig. 3.6, the M-integral may be written as [20]

$$M_N^{(1,2\alpha)} = \frac{1}{A_1} \sum_{k=1}^{2} \int_{V_k} \left[{}_k\sigma_{ij}^{(1)} \frac{\partial_k u_i^{(2\alpha)}}{\partial x_1} + {}_k\sigma_{ij}^{(2\alpha)} \frac{\partial_k u_i^{(1)}}{\partial x_1} - {}_k W^{(1,2\alpha)} \delta_{1j} \right] \frac{\partial q_1}{\partial x_j} \, dV, \tag{3.37}$$

where $M_N^{(1,2\alpha)}$ is the average value of the M-integral along the crack front in element N (see Fig. 3.6), $\alpha = a, b, c$, $i, j = 1, 2, 3$. The area ahead of the crack front created by the virtual crack extension shown in Fig. 3.6 is given by

$$A_1 = \int_0^{L_N} \ell_1^{(N)}(x_3) \, dx_3 \tag{3.38}$$

where $\ell_1^{(N)}(x_3)$ is the length of the virtual crack extension as shown in Fig. 3.6 and L_N is the length of element N along the crack front. The normalized virtual crack extension is now given by

$$q_1 = \sum_{i=1}^{20} N_i(\xi, \eta, \zeta) \, q_{1i} \tag{3.39}$$

where N_i are the shape functions in Eq. (3.3) and q_{1i} are chosen appropriately as described in [20]. On the other hand, substitution of Eqs. (3.16), (3.17) and (3.36) into (2.10) leads to

$$M_N^{(1,2\alpha)} = \frac{2}{H_1}\left(K_1^{(1)}K_1^{(2\alpha)} + K_2^{(1)}K_2^{(2\alpha)}\right) + \frac{2}{H_2}K_{III}^{(1)}K_{III}^{(2\alpha)}\,, \tag{3.40}$$

where H_1 and H_2 are given, respectively, in Eqs. (2.11) and (2.12).

Substituting the stress intensity factors of the auxiliary solutions in Table 3.1 into Eq. (3.40) and equating Eqs. (3.37) and (3.40) results in

$$K_1^{(1)} = \frac{H_1}{2A_1}\sum_{k=1}^{2}\int_{V_k}\left[{}_k\sigma_{ij}^{(1)}\frac{\partial_k u_i^{(2a)}}{\partial x_1} + {}_k\sigma_{ij}^{(2a)}\frac{\partial_k u_i^{(1)}}{\partial x_1} - {}_k W^{(1,2a)}\delta_{1j}\right]\frac{\partial q_1}{\partial x_j}\,dV\,; \tag{3.41}$$

$$K_2^{(1)} = \frac{H_1}{2A_1}\sum_{k=1}^{2}\int_{V_k}\left[{}_k\sigma_{ij}^{(1)}\frac{\partial_k u_i^{(2b)}}{\partial x_1} + {}_k\sigma_{ij}^{(2b)}\frac{\partial_k u_i^{(1)}}{\partial x_1} - {}_k W^{(1,2b)}\delta_{1j}\right]\frac{\partial q_1}{\partial x_j}\,dV\,; \tag{3.42}$$

and

$$K_{III}^{(1)} = \frac{H_2}{2A_1}\sum_{k=1}^{2}\int_{V_k}\left[{}_k\sigma_{ij}^{(1)}\frac{\partial_k u_i^{(2c)}}{\partial x_1} + {}_k\sigma_{ij}^{(2c)}\frac{\partial_k u_i^{(1)}}{\partial x_1} - {}_k W^{(1,2c)}\delta_{1j}\right]\frac{\partial q_1}{\partial x_j}\,dV\,. \tag{3.43}$$

A two-dimensional view of the integration domains is illustrated in Fig. 3.7. The thickness of each domain is equal to the thickness of the element along the crack front that participates in the integration. It should be noted that in contrast to the

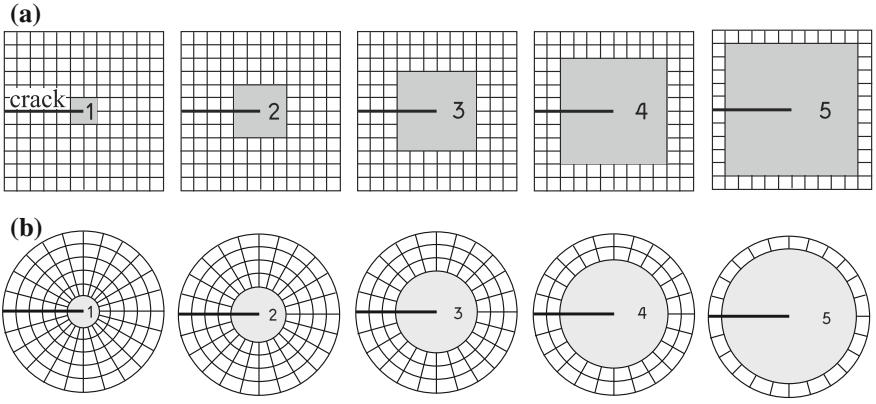

Fig. 3.7 Cross-sectional view of integration domains in the x_1x_2-plane for quarter-point **a** brick and **b** prismatic elements adjacent to the crack front. The numbers represent the integration volumes

two-dimensional analyses, topologically it is not possible to carry out the integration in rings surrounding the crack front. Rather, each integration volume includes the layer of elements in the previous volume. Hence, all integration volumes include the singular elements. In Fig. 3.7a, a cross-section of the integration volumes for brick elements are shown for 5 different domains; in Fig. 3.7b, these volumes include the prismatic, collapsed elements surrounding the crack front.

A three-dimensional thermal M-integral may be derived similarly to that in two dimensions. One may write that

$$M_N^{(1,2\alpha)} = \frac{1}{A_1} \sum_{k=1}^{2} \int_{V_k} \left\{ \left[{}_k\sigma_{ij}^{(1)} \frac{\partial_k u_i^{(2\alpha)}}{\partial x_1} + {}_k\sigma_{ij}^{(2\alpha)} \frac{\partial_k u_i^{(1)}}{\partial x_1} - {}_k\sigma_{rs}^{(1)} \, {}_k\epsilon_{rs}^{(2\alpha)} \delta_{1j} \right] \frac{\partial q_1}{\partial x_j} + \beta_{rs}^k \, {}_k\epsilon_{rs}^{(2\alpha)} \frac{\partial_k \vartheta^{(1)}}{\partial x_1} q_1 \right\} dV \tag{3.44}$$

where $\alpha = a, b$ and c in succession, $i, j, r, s = 1, 2, 3$, there is no summation on k and ${}_k\epsilon_{rs}^{(2\alpha)}$ is the mechanical strain of the first term of the asymptotic expansion. If the temperature change ${}_k\vartheta^{(1)}$ is a constant, then the M-integral in Eq. (3.44) agrees with the mechanical M-integral in Eq. (3.37). The only difference relates to the constitutive relation. For the thermal problem, the constitutive relation is given in Eq. (3.33); for the mechanical problem, $\tilde{\beta}_k$ is zero in Eq. (3.33). The remainder of the procedure is the same as for the three-dimensional mechanical M-integral.

3.4 Virtual Crack Closure Technique

The Virtual Crack Closure Technique (VCCT) was first presented in [33] for a linear elastic, homogeneous and isotropic material. It is based on the crack closure integral of Irwin [25] given by

$$\mathcal{G} = \lim_{\Delta a \to 0} \frac{1}{\Delta a} \int_0^{\Delta a} [\sigma_{22}(\Delta a - r) u_2(r) + \sigma_{21}(\Delta a - r) u_1(r) + \sigma_{23}(\Delta a - r) u_3(r)] \, dr \, . \tag{3.45}$$

In Eq. (3.45), Δa is the virtual crack extension; σ_{2j} are the traction components ahead of the crack of length a, $j = 1, 2, 3$, with σ_{22} shown in Fig. 3.8a; u_j are the crack face displacements of a crack of length $a + \Delta a$ and r is the radial coordinate along the crack faces as shown in Fig. 3.8b. The first, second and third integrals in Eq. (3.45) are, respectively, the modes I, II and III energy release rates, $\mathcal{G}_I$, $\mathcal{G}_{II}$ and $\mathcal{G}_{III}$.

To calculate the energy release rates for a particular problem by means of the finite element method, it would seem that two finite element analyses should be carried out. Considering, for example, mode I deformation and a four noded element, the energy release rate may be written as

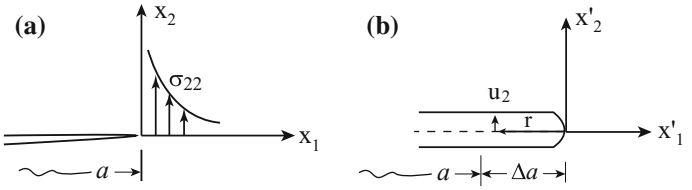

Fig. 3.8 **a** Crack of length a and **b** crack of length $a + \Delta a$

$$\mathcal{G}_I = \frac{1}{2\Delta a} F_{2m} \Delta u_{2m} \tag{3.46}$$

where Δa is the length of the virtual crack extension which is usually taken as the length of the elements surrounding the crack tip, F_{2m} is the nodal force in the x_2-direction at nodal point m (at the crack tip) for a crack of length a in Fig. 3.8a and Δu_{2m} is the crack opening displacement at nodal point m at the point behind the crack tip for a crack of length $a + \Delta a$ in Fig. 3.8b. Similar equations may be written for an element containing eight nodal points.

In [33], one finite element analysis was carried out with a crack of length $a + \Delta a$ and four noded elements. The nodal force was taken from the crack tip. This will be larger than that for a crack of length a. The displacement was taken from the nodal point for $r = \Delta a$ in Fig. 3.8b. Two problems were solved with a relative virtual crack extension $\Delta a/a = 0.1$. Stress intensity factors differed by less than 0.5% with those obtained by means of the line J-integral. It may be noted that the line J-integral has an error, as well.

The method was extended in [31] where again only one finite element mesh was analyzed for a crack of length a. The elements surrounding the crack tip were of length Δa. The force from the node at the crack tip was taken to be F_{2m}. The crack opening displacement was taken from the nodes behind the crack tip with $r = \Delta a$. This displacement will be smaller than the actual displacement for the case when the crack is extended by Δa. In addition to four noded elements, higher order elements were considered including quadratic, regular and quarter-point, as well as cubic, regular and singular elements. For all element types, a central cracked finite body with $a/b = 0.8$, where a is the half-crack length and b is the half-width of the body, produced energy release rate values within 3% agreement with a reference solution. The relative virtual crack extension of $\Delta a/a = 0.0625$ was used.

A summary of investigations carried out for interface cracks was presented in [6]. There were many studies which showed that the energy release rates $\mathcal{G}_I$ and $\mathcal{G}_{II}$ simply oscillate as Δa is varied and do not converge as $\Delta a \to 0$ [17, 23, 26, 28, 32, 35, 37]. Although the in-plane energy release rates oscillate, the stress intensity factors which are derived from them do not depend on Δa. Various equations were developed to obtain the stress intensity factors [14, 36, 37] producing multiple solutions from four to eight pair. In [1], various expressions for the stress intensity factors were compared and shown to be equivalent. Incorrect criteria were proposed

for eliminating extraneous solutions. In [6], two pairs of stress intensity factors were determined. The criterion for determining the valid pair stipulated that the crack is open as will be described.

In [6], the stress intensity factors were found as

$$K_1 = \pm\sqrt{H_1 \mathcal{G}_i}\cos\psi \qquad K_2 = K_1 \tan\psi \tag{3.47}$$

where H_1 is given in Eq. (2.11) and ψ is the mode mixity given by

$$\psi = \tan^{-1}\left(\frac{K_2}{K_1}\right) \tag{3.48}$$

or in Eq. (2.14) with $\hat{L} = 1$. In Eq. (3.47), the interface energy release rate is given by

$$\mathcal{G}_i = \mathcal{G}_I + \mathcal{G}_{II} \tag{3.49}$$

where $\mathcal{G}_I$ and $\mathcal{G}_{II}$ are found by means of a finite element analysis with eight noded elements and the expressions

$$\mathcal{G}_I = \frac{1}{2\Delta a}\sum_{m=1}^{N} F_{2m}\Delta u_{2m'} \tag{3.50}$$

$$\mathcal{G}_{II} = \frac{1}{2\Delta a}\sum_{m=1}^{N} F_{1m}\Delta u_{1m'}\ . \tag{3.51}$$

In Eqs. (3.50) and (3.51), F_{1m} and F_{2m} are the nodal point forces in the x_1 and x_2-directions, respectively, at node m; $\Delta u_{1m'}$ and $\Delta u_{2m'}$ are the displacement jumps in the x_1 and x_2-directions, respectively, at node m' (see Fig. 3.9); and N is the total number of nodes which participate in the calculation. The virtual crack extension $\Delta a = N\ell/2$ where ℓ is the length of each element included in the calculation. For example, if one element on each side of the crack tip participates in the calculation, then $N = 2$ and $\Delta a = \ell$ as shown in Fig. 3.9a. The displacement jumps are taken from the element behind the crack tip and the nodal point forces from the element ahead of the crack tip. Four elements involved in the calculation are illustrated in

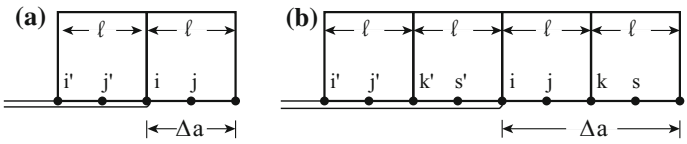

Fig. 3.9 Illustration of nodal points participating in energy release rate calculation for **a** one element and **b** two elements on each side of the crack tip. The length of each element participating in the calculation is ℓ; Δa is the virtual crack extension

Fig. 3.9b with $N = 4$ and $\Delta a = 2\ell$. The number of elements in the calculation may be increased in a similar manner. A discussion of this approach will be presented later.

The mode mixity ψ in Eq. (3.47) is not calculated from Eq. (3.48) since it depends on the complex stress intensity K which is unknown but rather from

$$\psi = \frac{1}{2}\cos^{-1}\left(\frac{1}{C}\frac{1-g}{1+g}\right) - \frac{1}{2}\tan^{-1}\left(\frac{P_I}{P_R}\right) - \varepsilon \ln \Delta a \ . \tag{3.52}$$

In Eq. (3.52),

$$g \equiv \frac{\mathcal{G}_{II}}{\mathcal{G}_I} \ , \tag{3.53}$$

$$P = \frac{\Gamma\left(\frac{1}{2} + i\varepsilon\right)\Gamma\left(\frac{1}{2} + i\varepsilon\right)}{\Gamma\left(2 + 2i\varepsilon\right)} \ . \tag{3.54}$$

where Γ is a special function and ε is given in Eq. (2.3) and P_R and P_I are, respectively, the real and imaginary parts of P given in Eq. (3.54). In Eq. (3.52),

$$C = \frac{\cosh \pi\varepsilon}{\pi}\sqrt{P_R^2 + P_I^2} \tag{3.55}$$

and Δa is the virtual crack extension.

Once ψ in Eq. (3.52) is known, two pairs of stress intensity factors in Eq. (3.47) are obtained. In order to determine the valid pair of stress intensity factors, it is assumed that the crack is open i.e. $\Delta u_y > 0$. Then, from Eq. $(3.5)_1$, one may require that

$$-\frac{\pi}{2} < \tan^{-1}\left(\frac{K_2}{K_1}\right) - \tan^{-1} 2\varepsilon + \varepsilon \ln r < \frac{\pi}{2} \tag{3.56}$$

where r may be chosen to be about $a/100$. The valid pair K_1 and K_2 satisfies Eq. (3.56).

In most studies, the virtual crack extension Δa consisted of one element as shown in Fig. 3.9a. One of the important contributions of [30] consists of the suggestion to use many very small elements as part of the virtual crack extension Δa. It may be noted that in [13], the idea of using more than one element in the calculation of the energy release rates was also made. In [6], many elements were used as part of the virtual crack extension. In fact, a sequence of values for Δa were used. Hence, many pairs of stress intensity values were obtained. In order to choose a 'best' solution, a criterion was proposed. In carrying out the analysis to obtain the relationship between the energy release rates $\mathcal{G}_I$ and $\mathcal{G}_{II}$, and the stress intensity factors K_1 and K_2, two additional integrals were found to be equal and given by

$$\frac{1}{2\Delta a}\int_0^{\Delta a}\sigma_{22}(x_1)\Delta u_1(\Delta a - x_1)dx_1 = \frac{1}{2\Delta a}\int_0^{\Delta a}\sigma_{21}(x_1)\Delta u_2(\Delta a - x_1)dx_1 \ . \tag{3.57}$$

The left and right hand sides of Eq. (3.57) are defined as $\mathcal{I}_I$ and $\mathcal{I}_{II}$, respectively. From the finite element analysis, these integrals may be written as

$$\mathcal{I}_I = \frac{1}{2\Delta a}\sum_{m=1}^{N} F_{2m}\Delta u_{1m'} \tag{3.58}$$

$$\mathcal{I}_{II} = \frac{1}{2\Delta a}\sum_{m=1}^{N} F_{1m}\Delta u_{2m'} \ . \tag{3.59}$$

In calculating $\mathcal{I}_I$ and $\mathcal{I}_{II}$ by means of Eqs. (3.58) and (3.59), it was observed that they are not equal as they should be analytically. The 'best' solution was chosen for

$$\text{percent difference} = \frac{\mathcal{I}_I - \mathcal{I}_{II}}{\mathcal{I}_I}\cdot 100 \tag{3.60}$$

being a minimum. In the case studied in [6], this was seen to be a good criterion.

Finite element analyses were presented in [6] for an interface crack between two dissimilar isotropic materials in a two-dimensional body. Very fine meshes were used. A further study for a crack between two dissimilar transversely isotropic materials examined use of coarser meshes [19]. It was found that if the stress intensity factors are similar in magnitude, it is possible to use one element as the virtual crack extension. If there is a difference between them by an order of magnitude or more, fine meshes and many elements as part of the virtual crack extension are required.

References

1. Agrawal A, Karlsson AM (2006) Obtaining mode mixity for a bimaterial interface crack using the virtual crack closure technique. Int J Fract 141:75–98
2. Banks-Sills L (1991) Application of the finite element method to linear elastic fracture mechanics. Appl Mech Rev 44:447–461
3. Banks-Sills L (2010) Update - application of the finite element method to linear elastic fracture mechanics. Appl Mech Rev 63:020803-1–020803-17
4. Banks-Sills L, Bortman Y (1984) Reappraisal of the quarter-point quadrilateral element in linear elastic fracture mechanics. Int J Fract 25:169–180
5. Banks-Sills L, Dolev O (2004) The conservative M-integral for thermal-elastic problems. Int J Fract 125:149–170
6. Banks-Sills L, Farkash E (2016) A note on the virtual crack closure technique for an interface crack. Int J Fract 201:171–180
7. Banks-Sills L, Sherman D (1989) On quarter-point three-dimensional finite elements in linear elastic fracture mechanics. Int J Fract 41:177–196
8. Banks-Sills L, Sherman D (1992) On the computation of stress intensity factors for three-dimensional geometries by means of the stiffness derivative and J-integral methods. Int J Fract 53:1–20

9. Banks-Sills L, Travitzky N, Ashkenazi D, Eliasi R (1999) A methodology for measuring interface fracture toughness of composite materials. Int J Fract 99:143–161
10. Banks-Sills L, Freed Y, Eliasi R, Fourman V (2006) Fracture toughness of the $+45°/-45°$ interface of a laminate composite. Int J Fract 141:195–210
11. Barsoum RS (1974) Application of quadratic isoparametric finite elements in linear fracture mechanics. Int J Fract 10:603–605
12. Barsoum RS (1976) On the use of isoparametric finite elements in linear fracture mechanics. Int J Num Methods Eng 10:25–37
13. Beuth JL (1996) Separation of crack extension modes in orthotropic delamination models. Int J Fract 77:305–321
14. Bjerkén C, Persson C (2001) A numerical method for calculating stress intensity factors for interface cracks in bimaterials. Eng Fract Mech 68:235–246
15. Chan SK, Tuba IS, Wilson WK (1970) On the finite element method in linear elastic fracture mechanics. Eng Fract Mech 2:1–17
16. Chen FHK, Shield RT (1977) Conservative laws in elasticity of J-integral type. Z Angew Math Phys 28:1–22
17. Dattaguru B, Venkatesha KS, Ramamurthy TS, Buchholz FG (1994) Finite element estimates of strain energy release rate components at the tip on an interface crack under mode I loading. Eng Fract Mech 49:451–463
18. Deng X (1993) General crack-tip fields for stationary and steadily growing interface cracks in anisotropic bimaterials. J Appl Mech 60:183–196
19. Farkash E, Banks-Sills L (2017) Virtual crack closure technique for an interface crack between two transversely isotropic materials. Int J Fract 205:189–202
20. Freed Y, Banks-Sills L (2005) A through interface crack between a $\pm 45°$ transversely isotropic pair of materials. Int J Fract 133:1–41
21. Fung YC (1965) Foundations of solid mechanics. Prentice Hall, New Jersey, pp 354–355
22. Gosz M, Dolbow J, Moran B (1998) Domain integral formulation for stress intensity factor computation along curved three-dimensional interface cracks. Int J Solids Struct 35:1763–1783
23. Hemanth D, Shivakumar Aradhya KS, Rama Murthy TS, Govinda Raju N (2005) Strain energy release rates for an interface crack in orthotropic media - a finite element investigation. Eng Fract Mech 72:759–772
24. Henshell RD, Shaw KG (1975) Crack tip finite elements are unnecessary. Int J Num Methods Eng 9:495–507
25. Irwin GR (1958) Fracture. In: Flügge S (ed) Encyclopedia of physics, vol IV. Springer, Germany, pp 551–590
26. Krueger R (2004) Virtual crack closure technique: history, approach, and applications. Appl Mech Rev 57:109–143
27. Li FZ, Shih CF, Needleman A (1985) A comparison of methods for calculating energy release rates. Eng Fract Mech 21:405–421
28. Mantič V, París F, (2004) Relation between SIF and ERR base measures of fracture mode mixity in interface cracks. Int J Fract 130:557–569
29. Moran B, Shih CF (1987) Crack tip and associated domain integrals from momentum and energy balance. Eng Fract Mech 27:615–642
30. Oneida EK, van der Meulen MCH, Ingraffea AR (2015) Methods for calculating G, G_I and G_{II} to simulate crack growth in 2D, multiple-material structures. Eng Fract Mech 140:106–126
31. Raju IS (1987) Calculation of strain-energy release rates with higher order and singular finite elements. Eng Fract Mech 28:251–274
32. Raju IS, Crews JH Jr, Aminpour MA (1988) Convergence of strain energy release rate components for edge-delaminated composite laminates. Eng Fract Mech 30:383–396
33. Rybicki EF, Kanninen MF (1977) A finite element calculation of stress intensity factors by a modified crack closure integral. Eng Fract Mech 9:931–938
34. Shih CF, Moran B, Nakamura T (1986) Energy release rate along a three-dimensional crack front in a thermally stressed body. Int J Fract 30:79–102

35. Sun CT, Jih CJ (1987) On strain energy release rates for interfacial cracks in bi-material media. Eng Fract Mech 28:13–20
36. Sun CT, Qian W (1997) The use of finite extension strain energy release rates in fracture of interfacial cracks. Int J Solids Struct 34:2595–2609
37. Toya M (1992) On mode I and mode II energy release rates of an interface crack. Int J Fract 56:345–352
38. Wilson WK, Yu I-W (1979) The use of the J-integral in thermal stress crack problems. Int J Fract 15:377–387
39. Yau JF, Wang SS (1984) An analysis of interface cracks between dissimilar isotropic materials using conservation integrals in elasticity. Eng Fract Mech 20:423–432
40. Yau JF, Wang SS, Corten HT (1980) A mixed-mode crack analysis of isotropic solids using conservation laws of elasticity. J Appl Mech 47:335–341

Chapter 4
Testing–Interface Crack Between Two Isotropic Materials

Abstract In this chapter, an interface crack between two dissimilar linear elastic, homogeneous and isotropic materials is considered. Methods of testing, as well as some test results are presented.

Keywords Brazilian disk specimen · Confidence · Failure curve · Interface fracture toughness · Probability

Experimental studies of a crack between two adherends joined by a thin layer of material such as epoxy, copper or nickel have been published [3, 9, 12–16]. Various specimens were tested. In general, it was found that the critical interface energy release rate $\mathcal{G}_{ic}$ is a function of the phase angle or mode mixity ψ given in Eq. (2.14). In addition, investigations were presented in which there were only two materials which were joined [5, 6, 10, 11, 17]. In [10, 17], the interface between aluminum and epoxy was studied; in [5, 11], the interface between glass and epoxy was studied; whereas, in [6], two ceramic clays were joined. In [10, 17], an empirical fracture criterion was used. In [5, 6, 11], the critical interface energy release rate $\mathcal{G}_{ic}$ was seen to be a function of the phase angle ψ.

Tests carried out on an interface crack between glass and epoxy [5], as well as a pair of ceramic clays [6] are described. A Brazilian disk specimen shown in Fig. 4.1 was employed. The Brazilian disk specimen was originally designed to test the tensile strength of concrete [8]. In Fig. 4.1a, a glass/epoxy specimen is shown with a 1 mm thick aluminum (AA 2024-T851) ring surrounding the epoxy. The ring was added to induce compressive stresses at the specimen edges along the interface to prevent separation. In Fig. 4.1b, two ceramic clays, K-142 and K-144, (Vingerling, Holland) were bonded together. In each case, there is a central crack of length $2a$ along the interface. The radius and thickness of the specimens are R and B, respectively. Various mixed mode combinations are attained by rotating the specimen within the loading frame [5, 6], that is, by changing the angle ω. The properties of the materials are presented in Table 4.1, where E is Young's modulus, ν is Poisson's ratio and α is the coefficient of thermal expansion.

Twenty-five glass/epoxy specimens were tested with results reported in [5]. The nominal radius of the specimens was $R = 20$ mm. The natural crack lengths ranged

L. Banks-Sills, *Interface Fracture and Delaminations in Composite Materials*,
SpringerBriefs in Structural Mechanics, DOI 10.1007/978-3-319-60327-8_4

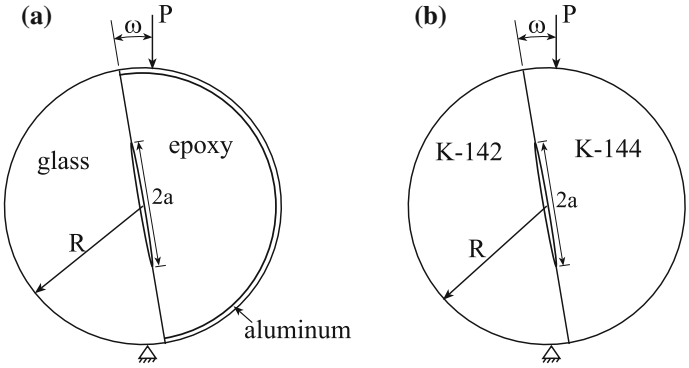

Fig. 4.1 Brazilian disk specimen composed of **a** glass and epoxy and **b** two ceramic clays

Table 4.1 Material properties of the bi-material, isotropic Brazilian disk specimens

Material	E (GPa)	ν	α (/°C)
Glass	73.0	0.22	8.00×10^{-6}
Epoxy	2.9	0.29	73.0×10^{-6}
Aluminium	70.0	0.33	23.5×10^{-6}
K-142	19.5	0.29	6.01×10^{-6}
K-144	23.3	0.20	5.38×10^{-6}

between 18.02 mm $\leq 2a \leq$ 22.64 mm, the thickness ranged between 7.79 mm $\leq B \leq$ 7.92 mm and the loading angle ranged between $-10° \leq \omega \leq 13°$. For the glass/epoxy pair, the oscillatory parameter was found from Eq. (2.3) to be $\varepsilon = -0.0881$. It may be pointed out that the specimens were cured in an oven at 25 °C. The temperature change ϑ was obtained from the difference between the curing temperature and the room temperature during the test.

Two-dimensional analyses were carried out to obtain the stress intensity factors resulting from applied loading and residual curing stresses [5]. The finite element method and the interaction energy or M-integral in Eqs. (3.25)–(3.28) [2] were used to obtain the $K_1^{(f)}$ and $K_2^{(f)}$ values for applied loading. A weight function [1, 4] was used to obtain the values of $K_1^{(r)}$ and $K_2^{(r)}$ arising from the residual stresses. The values from the two contributions were superposed. In [7], two-dimensional finite element analyses were carried out again for both the applied loading and residual stresses. The thermal M-integral in Eq. (3.34) was used for the latter. For both cases, the stress intensity factors were obtained by means of the interaction energy integral. It was found that the results obtained for applied loading differed by less than 0.9% except for very small values of $K_1^{(f)}$ obtained for the loading angle $\omega = 13°$. Since the meshes were finer in [7], the results obtained there are presented here. Moreover, for the $K^{(r)}$ values, differences of up to 2.6% were obtained. In [5], the weight function together with the finite element method were employed to obtain the results. It is thought that the M-integral used in [7] produced more accurate results.

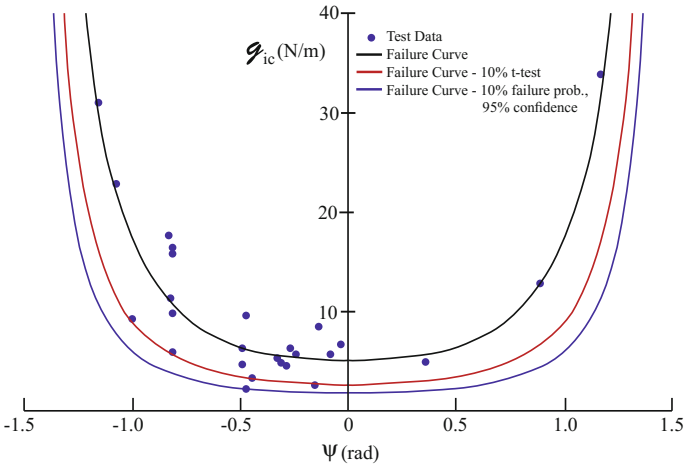

Fig. 4.2 Failure curves and test points for the glass/epoxy material pair ($\overline{\mathcal{G}}_{1c} = 5.1$ N/m, $\mathcal{G}^*_{1c} = 2.7$ N/m using the t-statistic, $\mathcal{G}^*_{1c} = 1.8$ N/m using the z-variate model and $\hat{L} = 1.1$ mm)

By means of superposition of the K-values for applied load and residual thermal stresses, the values of $K_1^{(T)}$ and $K_2^{(T)}$, where T represents total, were obtained. The energy release rate $\mathcal{G}_i$ may be calculated from Eq. (2.10) and the phase angle ψ from Eq. (2.14) with the total K-values. It may be noted that only a two-dimensional analysis is considered here so that K_{III} is omitted. In the process of determining the length $\hat{L}$, an arbitrarily small value is used to plot the $(\mathcal{G}_{ic}, \psi)$ points obtained for each specimen. A second $\hat{L}$ value is chosen to center the points about $\psi = 0$. In Fig. 4.2, the points are plotted with $\hat{L} = 1.1$ mm. For two-dimensions, the failure curve in Eq. (2.25) is found by taking $\phi = 0$ and given by

$$\mathcal{G}_{ic} = \overline{\mathcal{G}}_{1c} \left(1 + \tan^2 \psi\right) \ . \tag{4.1}$$

The value of $\overline{\mathcal{G}}_{1c} = 5.1$ N/m was found by taking the average of the values in Eq. (2.23) for all tests with $H_1 = 6.56$ GPa as defined in Eq. (2.11). The standard error of $\overline{\mathcal{G}}_{1c}$ is 0.36 N/m. Equation (4.1) is plotted as the black curve in Fig. 4.2. As mentioned previously, the value of $\hat{L}$ may be adjusted so that the test points and the failure curve give a better fit. This was not necessary here with $\hat{L} = 1.1$ mm.

This curve is the deterministic failure curve. To use this curve for predicting failure, consider a crack along an interface between these two materials in a structure. The values of $\mathcal{G}_i$ and ψ for $\hat{L} = 1.1$ mm are calculated. If the point lies below the failure curve, then crack propagation is not anticipated. However, it may be observed that there are test data below the curve. This is part of the scatter in the data. As described in Sect. 2.3, it is possible to obtain a failure probability curve by employing Eq. (2.26). In this study, use is made of the t-statistic for a 10% probability of unexpected failure, as well as the z-variate for a 10% probability of unexpected failure with a

95% confidence. Thus, below the adjusted failure curves, only statistical outliers may be found. To this end, use is made of Eqs. (2.26), (2.27) and (2.29) for the t-statistic. This curve is shown in Fig. 4.2 in red. The value of $\mathcal{G}_{1c}^{*}$ is found from Eq. (2.26) with the standard deviation $s = 1.81$ N/m and the value of $t_{0.1,24} = 1.32$, so that $K = 1.34$ and $\mathcal{G}_{1c}^{*} = 2.7$ N/m. For the curve in red in Fig. 4.2, there is a 10% probability that the next data point will be below this curve and the specimen will fail unexpectedly. Indeed, there is one data point from the test data below the curve. On the other hand using the z-variate, for a 10% failure curve with a 95% confidence, the expressions in Eqs. (2.30) and (2.31) are used. The value of $z_{0.1} = -1.28$ and $z_{0.95} = 1.64$ leading to a value of $K = 1.83$ and $\mathcal{G}_{1c}^{*} = 1.8$ N/m. Plotting Eq. (2.27) with this value of $\mathcal{G}_{1c}^{*}$ leads to the blue curve in Fig. 4.2. Again, one test point is below the curve.

Next, consider thirty-one bimaterial ceramic clay specimens which were tested [6]. The normalized crack length ranged between $0.27 \leq a/R \leq 0.32$, the thickness ranged between 9.23 mm $\leq B \leq$ 10.71 mm and the loading angles ranged between $-15^{\circ} \leq \omega \leq 15^{\circ}$. It may be noted that the crack was actually a thin notch which was created by a strip of Teflon which was about 10 μm thick. The oscillatory parameter, found from Eq. (2.3) was $\varepsilon = -0.00563$. The specimens were dried and sintered, reaching a maximum temperature of 1,040 °C. The temperature change ϑ was obtained from the difference between the curing temperature and the room temperature during the test.

Using the values of the total stress intensity factors $K_1^{(T)}$ and $K_2^{(T)}$, the energy release rate $\mathcal{G}_i$ was calculated from Eq. (2.10) and the phase angle ψ from Eq. (2.14); note that K_{III} was taken to be zero. An appropriate value of the length parameter is $\hat{L} = 100$ μm. The data points for this case are plotted in Fig. 4.3. The value of $\overline{\mathcal{G}}_{1c} = 3.9$ N/m is found by taking the average of the values in Eq. (2.23) with

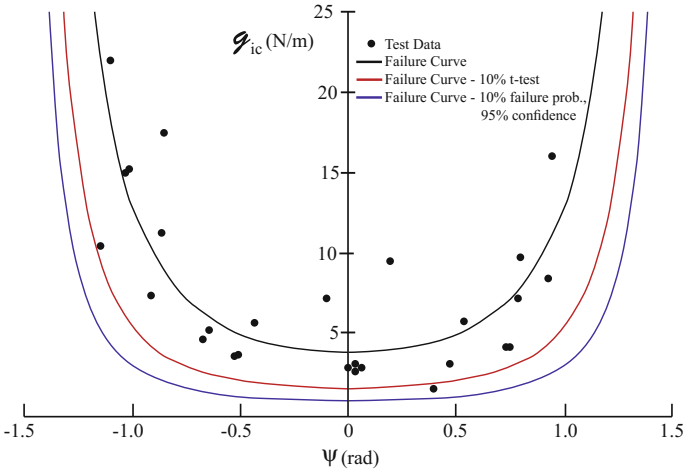

Fig. 4.3 Failure curves and test points for the ceramic clay material pair ($\overline{\mathcal{G}}_{1c} = 3.9$ N/m, $\mathcal{G}_{1c}^{*} = 1.6$ N/m using the t-statistic, $\mathcal{G}_{1c}^{*} = 0.9$ N/m using the z-variate model and $\hat{L} = 100$ μm)

$H_1 = 22.7$ GPa as defined in Eq. (2.11). The standard error of $\overline{\mathcal{G}}_{1c}$ is 0.30 N/m. Equation (4.1) is plotted as the black curve in Fig. 4.3. This is the deterministic failure curve. It may be noted that there are many test points below this curve. To obtain a curve which predicts a 10% probability of unexpected failure with the t-statistic, the parameter $\mathcal{G}^*_{1c}$ is found from Eqs. (2.26) and (2.29) with the standard deviation $s = 1.68$ N/m, the value of $t_{0.1,30} = 1.30$ so that $K = 1.32$. Recall that $N = 31$. The curve in Eq. (2.27) with $\mathcal{G}^*_{1c} = 1.6$ N/m is plotted in red in Fig. 4.3. There is one point below this curve. For the second approach where the probability of unexpected failure is $P = 10\%$ and the confidence is $\gamma = 95\%$, use of Eqs. (2.30) and (2.31) leads to $K = 1.76$, so that from Eq. (2.26), $\mathcal{G}^*_{1c} = 0.9$ N/m. In this case, there are no points below the failure curve.

In [7], three-dimensional analyses were carried out on each of the test specimens described in this chapter. Using these analyses, a three-dimensional failure surface was attained with a small range of values of the phase angle ϕ in Eq. (2.15). It was concluded that for a body containing an interface crack between two dissimilar isotropic materials subjected to in-plane loads, a two-dimensional analysis is sufficient for predicting failure.

References

1. Banks-Sills L (1993) Weight functions for interface cracks. Int J Fract 60:89–95
2. Banks-Sills L (2010) Update - application of the finite element method to linear elastic fracture mechanics. Appl Mech Rev 63:020803-1–020803-17
3. Banks-Sills L, Schwartz J (2002) Fracture testing of Brazilian disk sandwich specimens. Int J Fract 118:191–209
4. Banks-Sills L, Ashkenazi D, Eliasi R (1997) Determination of the effect of residual curing stresses on an interface crack by means of the weight function method. J Comput Mech 19:507–510
5. Banks-Sills L, Travitzky N, Ashkenazi D, Eliasi R (1999) A methodology for measuring interface fracture toughness of composite materials. Int J Fract 99:143–161
6. Banks-Sills L, Travitzky N, Ashkenazi D (2000) Interface fracture properties of a bimaterial ceramic composite. Mech Mater 32:711–722
7. Banks-Sills L, Konovalov N, Fliesher A (2010) Comparison of two and three-dimensional analyses of interface fracture data obtained from Brazilian disk specimens. Int J Struct Integr 1:20–42
8. Carneiro FLLB (1943) A new method to determine the tensile strength of concrete. In: Proceedings of the fifth meeting of the Brazilian association for technical rules, Third section, 126–129 (in Portuguese)
9. Cao HC, Evans AG (1989) An experimental study of the fracture resistance of bimaterial interfaces. Mech Mater 7:295–304
10. Ikeda T, Miyazaki N, Soda T (1998) Mixed mode fracture criterion of interface crack between dissimilar materials. Eng Fract Mech 59:725–735
11. Liechti KM, Chai YS (1991) Biaxial loading experiments for determining interfacial fracture toughness. J Appl Mech 58:680–687
12. Shanbhag MR, Eswaran K, Maiti SK (1993) Measurement of fracture toughness of bimaterial interfaces and a stress-based approach to their fracture. Eng Fract Mech 44:75–89
13. Thurston ME, Zehnder AT (1993) Experimental determination of silica/copper interfacial toughness. Acta Metall Mater 41:2985–2992

14. Thurston ME, Zehnder AT (1996) Nickel-alumina interfacial fracture toughness: experiments and analysis of residual stress effects. Int J Fract 76:221–241
15. Wang J-S (1995) Interfacial fracture toughness of a copper/alumina system and the effect of the loading phase angle. Mech Mater 20:251–259
16. Wang J-S, Suo Z (1990) Experimental determination of interfacial toughness curves using Brazil-nut-sandwiches. Acta Metall Mater 38:1279–1290
17. Yuuki R, Liu J-Q, Xu J-Q, Ohira T, Ono T (1994) Mixed mode fracture criteria for an interface crack. Eng Fract Mech 47:367–377

Part II
Delaminations in Composites

Chapter 5
Mathematical Treatment of Delaminations

Abstract In this chapter, a delamination in a multi-directional (MD) fiber reinforced laminate composite is considered. This problem is treated as an interface crack between two dissimilar anisotropic materials with both a square-root stress singularity and an oscillating, square-root singularity at the crack tip. The mechanical and thermal properties of the composite plies are obtained by means of homogenization. Several interfaces are considered including $0°//90°$, $+45°//-45°$, $30°//-60°$ and $-30°//60°$, as well as an interface between two woven plies of an MD laminate. The double slash represents the position of the delamination relative to the ply directions. The first term of the asymptotic expansion of the stress and displacement fields will be presented together with the interface energy release rate, phase angles and the J-integral.

Keywords Delamination · Interface energy release rate · Laminate · Lekhnitskii formalism · Multi-directional laminate · Oscillatory singularity · Phase angles · Stroh formalism · Woven composite

Delaminations are the most prevalent damage in composite laminates. In this chapter, long fiber reinforced composite plies, as well as woven fabric plies are considered. The material is inhomogeneous and anisotropic. The High Fidelity Generalized Method of Cells (HFGMC) [1] was used to obtain homogenized mechanical and thermal properties making the material effectively homogeneous and anisotropic. A delamination occurring between two plies with fibers in different directions is treated as an interface crack between two anisotropic materials (see Fig. 2.1).

To obtain the first term of the asymptotic expansion of the stress and displacement fields for any pair of dissimilar anisotropic materials, the Stroh [13] and Lekhnitskii [10] formalisms are used. For an interface crack or delamination between two dissimilar materials, there exists two singularities: an oscillatory, square-root singularity in the form of $-\frac{1}{2} \pm i\varepsilon$ and a square-root singularity $-\frac{1}{2}$. The oscillatory parameter ε is found following [14] as

$$\varepsilon = \frac{1}{2\pi} \ln\left(\frac{1+\beta}{1-\beta}\right) \tag{5.1}$$

L. Banks-Sills, *Interface Fracture and Delaminations in Composite Materials*,
SpringerBriefs in Structural Mechanics, DOI 10.1007/978-3-319-60327-8_5

where

$$\beta = \left\{ -\frac{1}{2} \operatorname{tr}(\check{\mathbf{S}}^2) \right\}^{1/2} . \tag{5.2}$$

The 3×3 matrix $\check{\mathbf{S}}$ is given by

$$\check{\mathbf{S}} = \mathbf{D}^{-1}\mathbf{W} \tag{5.3}$$

where

$$\mathbf{D} = \mathbf{L}_1^{-1} + \mathbf{L}_2^{-1} \tag{5.4}$$

and

$$\mathbf{W} = \mathbf{S}_1\mathbf{L}_1^{-1} - \mathbf{S}_2\mathbf{L}_2^{-1} . \tag{5.5}$$

The subscripts 1 and 2 in Eqs. (5.4) and (5.5) represent, respectively, the upper and lower material. Since the Barnett–Lothe tensors $\mathbf{S}_k$ and $\mathbf{L}_k$ are real [14] (pp. 146–147) and

$$-\mathbf{A}_k\mathbf{B}_k^{-1} = \mathbf{S}_k\mathbf{L}_k^{-1} + i\mathbf{L}_k^{-1} , \tag{5.6}$$

knowledge of the left hand side of Eq. (5.6) is sufficient to determine Eqs. (5.4) and (5.5). In Eq. (5.6), there is no summation on k. Since the matrices $\boldsymbol{D}$, $\boldsymbol{W}$ and $\check{\mathbf{S}}$ involve basic arithmetic operations of matrices applied to the Barnett–Lothe tensors, which are real, the tensors $\boldsymbol{D}$, $\boldsymbol{W}$ and $\check{\mathbf{S}}$ are real, as well. Furthermore, $\boldsymbol{D}$ and $\boldsymbol{D}^{-1}$ are symmetric positive definite tensors and $\boldsymbol{W}$ is a skew symmetric tensor [14] (pp. 344, 426).

The general expressions for the matrices $\mathbf{A}_k$, $\mathbf{B}_k$ and $\mathbf{B}_k^{-1}$ which may be found in [14] (pp. 170–172) are presented in Appendix B. The specific matrices for the upper and lower materials for each interface considered are also presented in Appendix B. It is observed that the notation employed here for ε in Eq. (5.1) differs from that of Rice [11] and Hutchinson [8] in which the fraction is inverted. The notation here is in keeping with Dundurs [6]. However, it is immaterial if one is consistent.

The relations

$$\sigma_{j1} = -\phi_{j,2} \tag{5.7}$$

$$\sigma_{j2} = \phi_{j,1} \tag{5.8}$$

are useful for obtaining the stress components where ϕ_j ($j = 1.2.3$) is a stress function. The general expressions for the displacement vector $\mathbf{u}$ and the stress function vector $\boldsymbol{\phi}$ are presented in Appendix C.

In Sect. 5.1, a laminate containing plies reinforced with long fibers in a multi-directional layup is considered. The fibers in the upper ply are in the 0°-direction and those in the lower ply are in the 90°-direction. Making reference to Fig. 2.1, the 0°-direction coincides with the x_1-axis and fibers in the 90°-direction coincide with the x_3-direction. An interface delamination is located between these two plies. Next, in Sect. 5.2, an interface delamination between plies with fibers in the $+45°$ and $-45°$-directions is considered. Another two layups are presented in Sect. 5.3. One has an interface between two plies with fibers in the $+30°$-direction in the upper

ply and fibers in the $-60°$ in the lower ply. For the second case, the upper ply has fibers in the $-30°$-direction; in the lower ply, they are in the $+60°$-direction. Finally in Sect. 5.4, two woven plies are considered with tows in different directions.

5.1 The 0°//90° Interface

Consider that material (1) consists of a material with fibers in the 0°-direction and material (2) is a material which consists of fibers in the 90°-direction (see Fig. 2.1). The delamination front is along the x_3-axis. Thus, the upper and lower materials are transversely isotropic in this coordinate system and described by five independent elastic constants and two coefficients of thermal expansion. For two different carbon/epoxy composites (AS4/3501-6 and AS4/3502), the mechanical and thermal properties were obtained by means of a micro-mechanical model from the properties of the constituents. Use was made of the High Fidelity Generalized Method of Cells (HFGMC) [1]. The mechanical properties may be found in [2] for AS4/3501-6; the mechanical properties and coefficients of thermal expansion may be found in [4] for AS4/3502.

For the 0°//90° interface, the first term of the asymptotic solution for the stress components is given in Eqs. (2.1) and (2.5). The double slash indicates the location of the delamination. As with two isotropic materials, for this pair of materials,

$$K = K_1 + iK_2 \; ; \tag{5.9}$$

that is, the oscillatory, square-root singularity is associated with the in-plane deformation. For this interface, there is also a square-root singularity associated with out-of-plane deformation and K_{III}. To obtain a definition for the complex stress intensity factor K in Eq. (5.9), consider the stress components which are related to the stress function vector through Eq. (5.8). The stress function vector $\phi^{(1)}$ in Eq. (C.14) is differentiated with respect to x_1 and evaluated along the interface for $\theta = 0$ to obtain the stress components ${}_1\sigma_{2i}$ for the oscillatory, square-root singular part of the solution as

$$\left[\begin{array}{c} {}_1\sigma_{21} \\ {}_1\sigma_{22} \\ {}_1\sigma_{23} \end{array}\right]\Bigg|_{\theta=0} = r^{-\frac{1}{2}} \cosh \pi\varepsilon \left[\begin{array}{c} -\sqrt{\dfrac{D_{22}}{D_{11}}}\, \Im\left\{(1+2i\varepsilon) r^{i\varepsilon} d_2\right\} \\ \Re\left\{(1+2i\varepsilon) r^{i\varepsilon} d_2\right\} \\ 0 \end{array}\right] . \tag{5.10}$$

It may be noted that the vector $\mathbf{d}$ in Eq. (C.26) is substituted into Eq. (C.14) and d_2 is complex. For the square-root singular part of the solution, Eq. (C.18) is used with Eq. (C.27) to obtain

$$\left[\begin{array}{c} {}_1\sigma_{21} \\ {}_1\sigma_{22} \\ {}_1\sigma_{23} \end{array}\right]\Bigg|_{\theta=0} = \frac{1}{2} r^{-\frac{1}{2}} \left[\begin{array}{c} 0 \\ 0 \\ 1 \end{array}\right] d_3 \tag{5.11}$$

where d_3 is real. The back subscript 1 denotes the upper material. The total solution is the sum of the oscillatory, square-root and square-root singular stress components.

By manipulating Eq. (5.10), it seems natural to express the complex stress intensity factor K as

$$K \equiv \lim_{r\to 0} \sqrt{2\pi r}\, r^{-i\varepsilon} \left(\sigma_{22} - i\sqrt{\frac{D_{11}}{D_{22}}}\sigma_{21} \right)\Bigg|_{\theta=0} . \tag{5.12}$$

The amplitude of the square-root singularity K_{III} is obtained directly from Eq. (5.11) as

$$K_{III} \equiv \lim_{r\to 0} \sqrt{2\pi r}\, \sigma_{23}\Big|_{\theta=0} . \tag{5.13}$$

The unknown scalars d_2 and d_3 in Eqs. (5.10) and (5.11) are obtained by substituting the traction components given in Eqs. (5.10) and (5.11) into (5.12) and (5.13), respectively, yielding

$$d_2 = \frac{K}{\sqrt{2\pi}\,(1+2i\varepsilon)\cosh \pi\varepsilon}, \quad d_3 = \frac{2K_{III}}{\sqrt{2\pi}} . \tag{5.14}$$

Referring again to the expression for the stress components in Eqs. (2.1) and (2.5), the functions ${}_k\Sigma^{(1)}_{\alpha\beta}(\theta)$, ${}_k\Sigma^{(2)}_{\alpha\beta}(\theta)$ and ${}_k\Sigma^{(III)}_{\alpha 3}(\theta)$ are given in Appendix C. The displacement functions ${}_kU^{(1)}_{\alpha}(\theta)$, ${}_kU^{(2)}_{\alpha}(\theta)$ and ${}_kU^{(III)}_{\alpha}(\theta)$ in Eqs. (2.6) and (2.7) are also given in Appendix C.

For conditions of plane deformation [14], it is possible from Eqs. (5.12) and (5.13) to write the stress components along the interface ahead of the crack tip as

$$\left(\sigma_{22} - i\sqrt{\frac{D_{11}}{D_{22}}}\sigma_{21} \right)\Bigg|_{\theta=0} = \frac{K r^{i\varepsilon}}{\sqrt{2\pi r}} \tag{5.15}$$

and

$$\sigma_{23}\Big|_{\theta=0} = \frac{K_{III}}{\sqrt{2\pi r}} . \tag{5.16}$$

From Eqs. (2.6) and (2.7), with use of Appendix C, the crack face displacement jumps in the vicinity of the crack tip are found to be

$$\Delta u_2 - i\sqrt{\frac{D_{22}}{D_{11}}}\Delta u_1 = \frac{2D_{22}}{(1+2i\varepsilon)\cosh \pi\varepsilon}\sqrt{\frac{r}{2\pi}}\, K r^{i\varepsilon} \tag{5.17}$$

and

$$\Delta u_3 = 2D_{33}\sqrt{\frac{r}{2\pi}}\, K_{III} . \tag{5.18}$$

It may be noted that in [2], the parameter β defined in Eq. (5.2) was chosen to be negative, so that the oscillatory parameter ε in Eq. (5.1) was also negative.

Here, ε is chosen to be positive which may be done without loss of generality. In addition, the form of the complex vector $\mathbf{d}$ in Eq. (C.26) was chosen differently in [2]. Hence, the stress functions ${}_k\Sigma^{(1)}_{\alpha\beta}(\theta)$ and ${}_k\Sigma^{(2)}_{\alpha\beta}(\theta)$, as well as the displacement functions ${}_kU^{(1)}_{\alpha}(\theta)$ and ${}_kU^{(2)}_{\alpha}(\theta)$ take a different form. But the values of the stress and displacement components are the same.

Use is made of the Irwin crack closure integral in Eq. (3.45) with a coordinate transformation to obtain the in-plane interface energy release rate as

$$\mathcal{G}_o = \lim_{\Delta a\to 0}\frac{1}{2\Delta a}\int_0^{\Delta a}\Re\left\{\left[\sigma_{22}(x_1) - i\sqrt{\frac{D_{11}}{D_{22}}}\sigma_{21}(x_1)\right]\right.$$
$$\left.\times\left[\Delta u_2(\Delta a - x_1) + i\sqrt{\frac{D_{22}}{D_{11}}}\Delta u_1(\Delta a - x_1)\right]\right\}dx_1\ . \tag{5.19}$$

In Eq. (5.19), the subscript o represents oscillatory. The mode III interface energy release rate may be determined from

$$\mathcal{G}_s = \lim_{\Delta a\to 0}\frac{1}{2\Delta a}\int_0^{\Delta a}\sigma_{23}(x_1)\Delta u_3(\Delta a - x_1)dx_1\ . \tag{5.20}$$

In Eq. (5.20), the subscript s represents square-root singular. Substituting Eqs. (5.15) and (5.17) into (5.19) and substituting Eqs. (5.16) and (5.18) into (5.20), and carrying out the integration, leads to an expression for the total interface energy release rate given as

$$\mathcal{G}_i = \frac{1}{H_1}\left(K_1^2 + K_2^2\right) + \frac{1}{H_2}K_{III}^2 \tag{5.21}$$

where

$$\frac{1}{H_1} = \frac{D_{22}}{4\cosh^2\pi\varepsilon} \tag{5.22}$$

$$\frac{1}{H_2} = \frac{D_{33}}{4}\ . \tag{5.23}$$

The complex stress intensity factor K in Eq. (2.2) is written in normalized form in Eq. (2.9), so that

$$\hat{K} = |K|\,e^{i\psi}\ , \tag{5.24}$$

and the phase angle is given as

$$\psi = \tan^{-1}\left[\frac{\Im(K\hat{L}^{i\varepsilon})}{\Re(K\hat{L}^{i\varepsilon})}\right] = \tan^{-1}\left[\sqrt{\frac{D_{11}}{D_{22}}}\frac{\sigma_{21}}{\sigma_{22}}\right]\Bigg|_{\theta=0,r=\hat{L}}\ . \tag{5.25}$$

It may be noted that

$$|K| = |\hat{K}|\ , \tag{5.26}$$

$\hat{L}$ is an arbitrary length quantity, and D_{11} and D_{22} are given in Eqs. (B.37) and (B.38). It may be noted that in Chap. 4, $\hat{L}$ was used to center the test data in the failure space. A second phase angle may be defined as

$$\phi = \tan^{-1}\left[\sqrt{\frac{H_1}{H_2}}\frac{K_{III}}{\sqrt{K_1^2+K_2^2}}\right] = \tan^{-1}\left(\sqrt{\frac{H_1}{H_2}}\frac{\sigma_{23}}{\sqrt{\sigma_{22}^2+D_{11}\sigma_{21}^2/D_{22}}}\right)\Bigg|_{\theta=0,r=\hat{L}}. \tag{5.27}$$

Equations $(5.25)_1$ and $(5.27)_1$ are the same as Eqs. $(2.14)_1$ and $(2.15)_1$. The difference is in the expressions for H_1 and H_2. Moreover, the expression for the interface energy release rate in Eqs. (2.10) and (5.21) are identical. The J-integral in Eq. (2.17) and the relation between J and $\mathcal{G}_i$ hold for all combinations of anisotropic materials including those for the $0°//90°$ interface.

5.2 The $+45°//-45°$ Interface

In this section, an interface delamination between two plies is considered in which the upper ply consists of fibers which are rotated by 45° with respect to the x_1-direction and those in the lower ply are rotated by $-45°$ with respect to the x_1-direction as shown in Fig. 5.1. For the analysis, the geometry considered is shown in Fig. 2.1 in which two half-spaces of these two materials are modeled.

For this material pair, the amplitude of the oscillatory, square-root singularity is

$$K = K_1 + iK_3 \tag{5.28}$$

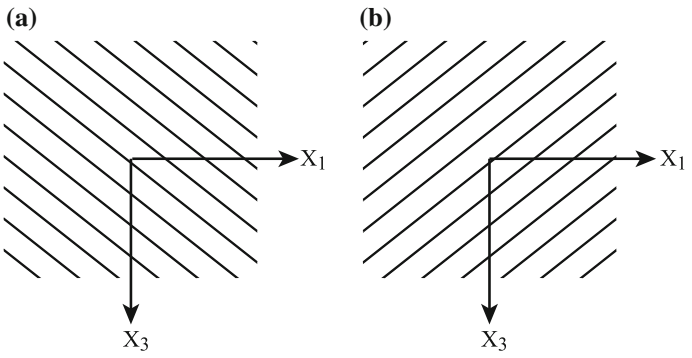

Fig. 5.1 Fibers shown in **a** $+45°$-direction and **b** $-45°$-direction with respect to the x_1-axis

and the amplitude of the square-root singularity is K_{II}. For the upper material, the displacement and stress function vectors $\mathbf{u}^{(1)}$ and $\phi^{(1)}$ are defined in Eqs. (C.13) and (C.14) for the oscillatory, square-root singularity and in Eqs. (C.17) and (C.18) for the square-root singularity; for the lower material, they are defined in Eqs. (C.15) and (C.16) for the oscillatory, square-root singularity and in Eqs. (C.19) and (C.20) for the square-root singularity. The components of the matrix $\mathbf{A}_k$ are given in Eqs. (B.62)–(B.70); those of $\mathbf{B}_k$ are given in Eqs. (B.83)–(B.91); and those of $\mathbf{B}_k^{-1}$ are given in Eqs. (B.96)–(B.104). Recall the relations in Eqs. (B.79)–(B.82), (B.92)–(B.95) and (B.105)–(B.108).

The complex vector $\mathbf{d}$ in Eqs. (C.13)–(C.16) is found from Eq. (C.10) and is given by

$$\mathbf{d}^T = \left[0,\, 1,\, -i\sqrt{D_{22}/D_{33}}\right] d_2 \tag{5.29}$$

where d_2 is an arbitrary complex scalar. In a similar manner, the real vector $\mathbf{d}^*$ in Eqs. (C.17)–(C.20) is found as

$$\mathbf{d}^{*T} = [1,\, 0,\, 0]\, d_3 \tag{5.30}$$

where d_3 is a real constant.

Using Eq. (5.29) in (C.14) and (5.8), the tractions along the interface for the oscillatory, square-root singularity are found as

$$\left[\begin{array}{c} {}_1\sigma_{21} \\ {}_1\sigma_{22} \\ {}_1\sigma_{23} \end{array}\right]\Bigg|_{\theta=0} = r^{-\frac{1}{2}} \cosh \pi\varepsilon \left[\begin{array}{c} 0 \\ \Re\left\{(1+2i\varepsilon)r^{i\varepsilon} d_2\right\} \\ \sqrt{\dfrac{D_{22}}{D_{33}}}\, \Im\left\{(1+2i\varepsilon)r^{i\varepsilon} d_2\right\} \end{array}\right] . \tag{5.31}$$

For the square-root singular part of the solution from Eqs. (5.30), (C.18) and (5.8),

$$\left[\begin{array}{c} {}_1\sigma_{21} \\ {}_1\sigma_{22} \\ {}_1\sigma_{23} \end{array}\right]\Bigg|_{\theta=0} = \frac{1}{2} r^{-\frac{1}{2}} \left[\begin{array}{c} 1 \\ 0 \\ 0 \end{array}\right] d_3 \, . \tag{5.32}$$

As before for the $0°//90°$ interface, the total solution is the sum of the oscillatory, square-root singular and the square-root singular stress components.

By manipulating Eq. (5.31), the complex stress intensity factor in Eq. (5.28) may be defined as

$$K \equiv \lim_{r\to 0} \sqrt{2\pi r}\, r^{-i\varepsilon} \left(\sigma_{22} + i\sqrt{\frac{D_{33}}{D_{22}}}\sigma_{23}\right)\Bigg|_{\theta=0} . \tag{5.33}$$

The amplitude of the square-root singularity K_{II} is obtained from Eq. (5.32) as

$$K_{II} \equiv \lim_{r\to 0} \sqrt{2\pi r}\, \sigma_{21}\Big|_{\theta=0} . \tag{5.34}$$

The unknown scalars d_2 and d_3 in Eqs. (5.31) and (5.32) are obtained by substituting the traction components given in Eqs. (5.31) and (5.32) into (5.33) and (5.34), respectively, yielding

$$d_2 = \frac{K}{\sqrt{2\pi}\,(1+2i\varepsilon)\cosh\pi\varepsilon}, \quad d_3 = \frac{2K_{II}}{\sqrt{2\pi}}\,. \tag{5.35}$$

For conditions of plane deformation, it is possible from Eqs. (5.33) and (5.34) to write the stress components along the interface ahead of the crack tip as

$$\left(\sigma_{22} + i\sqrt{\frac{D_{33}}{D_{22}}}\sigma_{23}\right)\Big|_{\theta=0} = \frac{Kr^{i\varepsilon}}{\sqrt{2\pi r}} \tag{5.36}$$

and

$$\sigma_{21}\Big|_{\theta=0} = \frac{K_{II}}{\sqrt{2\pi r}}\,. \tag{5.37}$$

The crack face displacement jumps in the vicinity of the crack tip are found to be

$$\Delta u_2 + i\sqrt{\frac{D_{22}}{D_{33}}}\Delta u_3 = \frac{2D_{22}}{(1+2i\varepsilon)\cosh\pi\varepsilon}\sqrt{\frac{r}{2\pi}}\,Kr^{i\varepsilon} \tag{5.38}$$

and

$$\Delta u_1 = 2D_{11}\sqrt{\frac{r}{2\pi}}K_{II}\,. \tag{5.39}$$

Substituting Eqs. (C.14) and (C.18) for the upper material and Eqs. (C.16) and (C.20) for the lower material into Eqs. (5.7) and (5.8), the stress components may be written as

$${}_k\sigma_{ij} = \frac{1}{\sqrt{2\pi r}}\left[\Re\left(Kr^{i\varepsilon}\right)\,{}_k\Sigma_{ij}^{(1)}(\theta) + \Im\left(Kr^{i\varepsilon}\right)\,{}_k\Sigma_{ij}^{(3)}(\theta)\right] + \frac{K_{II}}{\sqrt{2\pi r}}\,{}_k\Sigma_{ij}^{(II)}(\theta) \tag{5.40}$$

where the complex stress intensity factor is defined in Eq. (5.28) and $i, j = 1, 2, 3$. In Eqs. (C.14), (C.18), (C.16) and (C.20), the expressions in Eqs. (B.83)–(B.108) are used for the upper and lower materials. It may be noted that all stress components have an oscillatory, square-root singular and square-root singular component. On the interface, the stress component ${}_k\sigma_{21}$ is only square-root singular; it does not have an oscillatory part. The stress components ${}_k\sigma_{22}$ and ${}_k\sigma_{23}$ on the interface possess an oscillatory, square-root singularity and not a pure square-root singularity. This behavior is corroborated by Eqs. (5.31) and (5.32). The behavior of the stress components for the $+45°//-45°$ interface differs from that of the $0°//90°$ interface. Whereas, for the latter, the in-plane stress components have only an oscillatory, square-root

singular part, all stress components for the former have this behavior. In addition, for the latter, only the out-of-plane stress components have a square-root singular part, for the former, all stress components have this behavior. The functions $k\Sigma_{ij}^{(1)}(\theta)$, $k\Sigma_{ij}^{(3)}(\theta)$ and $k\Sigma_{ij}^{(II)}(\theta)$ in Eq. (5.40) are presented in [7].

Using Eqs. (C.13) and (C.17) for the upper material and Eqs. (C.15) and (C.19) for the lower material, the displacement components are found as

$$ {}_k u_i = \sqrt{\frac{r}{2\pi}}\left[\Re\left(Kr^{i\varepsilon}\right)\ {}_k U_i^{(1)}(\theta) + \Im\left(Kr^{i\varepsilon}\right)\ {}_k U_i^{(3)}(\theta)\right] + \sqrt{\frac{r}{2\pi}} K_{II}\ {}_k U_i^{(II)}(\theta)\ . \tag{5.41} $$

In Eqs. (C.13), (C.17), (C.15) and (C.19), the expressions in Eqs. (B.62)–(B.70) and (B.96)–(B.108) are used for the upper and lower materials. The functions ${}_k U_i^{(1)}(\theta)$, ${}_k U_i^{(3)}(\theta)$ and ${}_k U_i^{(II)}(\theta)$ may be found in [7].

Making use of the Irwin crack closure integral in Eq. (3.45) with a coordinate transformation, the interface energy release rate is found to be

$$ \mathcal{G}_i = \frac{1}{H_1}\left(K_1^2 + K_3^2\right) + \frac{1}{H_2} K_{II}^2 \tag{5.42} $$

where

$$ \frac{1}{H_1} = \frac{D_{22}}{4\cosh^2 \pi\varepsilon} \tag{5.43} $$

$$ \frac{1}{H_2} = \frac{D_{11}}{4}\ . \tag{5.44} $$

The complex stress intensity factor K in Eq. (5.28) is normalized as in Eq. (5.24) where the phase angle ψ is given by

$$ \psi = \tan^{-1}\left[\frac{\Im(K\ L^{i\varepsilon})}{\Re(K\ L^{i\varepsilon})}\right] = \tan^{-1}\left[\sqrt{\frac{D_{33}}{D_{22}}}\frac{\sigma_{23}}{\sigma_{22}}\right]\Bigg|_{\theta=0, r=L}\ . \tag{5.45} $$

A second phase angle is defined as

$$ \phi = \tan^{-1}\left[\sqrt{\frac{H_1}{H_2}}\frac{K_{II}}{\sqrt{K_1^2 + K_3^2}}\right] = \tan^{-1}\left(\sqrt{\frac{H_1}{H_2}}\frac{\sigma_{21}}{\sqrt{\sigma_{22}^2 + D_{33}\sigma_{23}^2/D_{22}}}\right)\Bigg|_{\theta=0, r=\hat{L}}\ . \tag{5.46} $$

5.3 The $+30°//-60°$ and $-30°//+60°$ Interfaces

In this section, two interfaces are considered. Material (1) in Fig. 2.1 has fibers either in the $+30°$-direction or the $-30°$-direction. For the former direction, the fibers are rotated clockwise by $30°$ with respect to the x_1-axis similar to that shown in Fig. 5.1a; for the latter direction, the fibers are rotated counter-clockwise by $30°$ with respect to the x_1-axis similar to that shown in Fig. 5.1b. For material (2) in Fig. 2.1, fibers are either in the $-60°$-direction as shown schematically in Fig. 5.1b or the $+60°$-direction as shown schematically in Fig. 5.1a. Each pair of materials represents a cross-ply which is at an angle with respect to the delamination front. Each of the materials is monoclinic with respect to the delamination coordinates shown in Fig. 2.1 with $x_2 = 0$ a symmetry plane for all materials.

In Sect. B.3, some of the basic expressions related to these interfaces are presented. As with the other interfaces discussed here, there is an oscillatory, square-root singularity and a square-root singularity. To obtain the first term of the asymptotic expressions for the stress and displacement components the vector $\mathbf{d}$ used in Eqs. (C.13)–(C.16) must be determined. A relation between the components of the vector $\boldsymbol{d}$ is obtained by solving Eq. (C.10) with the eigenvalue $\cot \delta\pi$. The eigenvector $\boldsymbol{d}$ that corresponds to the eigenvalue $\cot \delta\pi = -i\beta$, for which the singularity $\delta = -\frac{1}{2} + i\varepsilon$, where β is given in Eq. (B.140) and ε is given in Eq. (5.1), is of the form

$$\boldsymbol{d}^T = [i\Omega, 1, i\Lambda]\, d_2 \,, \tag{5.47}$$

where d_2 is a complex unknown constant. In Eq. (5.47), Ω and Λ are real and given by

$$\Omega = \frac{D_{33}W_{12} + D_{13}W_{23}}{\beta(D_{11}D_{33} - D_{13}^2)} \tag{5.48}$$

$$\Lambda = -\frac{D_{13}W_{12} + D_{11}W_{23}}{\beta(D_{11}D_{33} - D_{13}^2)} \,. \tag{5.49}$$

The constants D_{11}, D_{33}, D_{13}, W_{12}, W_{13} and W_{23} are components of the tensors $\mathbf{D}$ and $\mathbf{W}$ given in Eqs. (B.135) and (B.138). The eigenvector for $\cot \delta\pi = i\beta$, for which $\delta = -\frac{1}{2} - i\varepsilon$, is the complex conjugate of $\boldsymbol{d}$, namely

$$\overline{\boldsymbol{d}}^T = [-i\Omega, 1, -i\Lambda]\, \overline{d}_2 \,. \tag{5.50}$$

The eigenvectors $\boldsymbol{d}$ and $\overline{\boldsymbol{d}}$ correspond to the oscillatory, square-root solution. Note that a bar over a quantity represents its complex conjugate. The components of these vectors are used to relate the stress and displacement fields to the stress intensity factors of this solution. For the square-root singular solution, the eigenvector is found for $\cot(\delta\pi) = 0$, for which $\delta = -\frac{1}{2}$, as

$$\boldsymbol{d}^{*T} = \left[\frac{W_{23}}{W_{12}}\,,0\,,1\right] d_3 \tag{5.51}$$

where d_3 is a real unknown constant which is used to relate the stress and displacement fields to the stress intensity factors of this solution.

The vectors $\boldsymbol{d}$ and $\boldsymbol{d}^*$ may be related to the stress intensity factors through the stresses along the interface, namely for $\theta = 0$. Along the interface, the expressions for the stresses are a linear combination of $\boldsymbol{d}$ and $\boldsymbol{d}^*$. For the most general case, the vectors $\boldsymbol{d}$ and $\boldsymbol{d}^*$ each consists of three independent components, leading to the existence of six stress intensity factors; three associated with the oscillatory, square-root singularities ($\delta = -\frac{1}{2} \pm i\varepsilon$), and three associated with the square-root singularity ($\delta = -\frac{1}{2}$). For the monoclinic materials studied in this investigation, $\boldsymbol{d}$ and $\boldsymbol{d}^*$ are given in Eqs. (5.47) and (5.51), respectively. Hence, it may be seen that one stress intensity factor which belongs to the square-root singularity vanishes, which reduces the number of stress intensity factors to five. In fact, it is possible to reduce the number of independent stress intensity factors to three. This is a direct result of the way in which $\boldsymbol{d}$ and $\boldsymbol{d}^*$ are related to the stress intensity factors as shown in the sequel.

For monoclinic materials with $x_2 = 0$ a symmetry plane, at first it may seem impossible to define the stress intensity factors as has been done previously. However, closer observation reveals that although there are five stress intensity factors, only three of them are independent. This allows representation of the stress and displacement components with only three of the stress intensity factors. The stress intensity factors related to the oscillatory, square-root singular field are denoted by K_1, K_2 and K_3, whereas the stress intensity factors related to the square-root singular field will be denoted by K_{II} and K_{III}. Relations have been found between K_2 and K_3, and between K_{II} and K_{III}, which will be presented in the sequel. Without loss of generality, further derivations are in terms of the stress intensity factors K_1, K_2 and K_{III}.

For the oscillatory, square-root singular solution, the traction components along the interface may be obtained from Eqs. (C.14), (5.8) and (5.47) with $\theta = 0$ as

$$\left[\begin{array}{c} {}_1\sigma_{21} \\ {}_1\sigma_{22} \\ {}_1\sigma_{23} \end{array}\right]\Bigg|_{\theta=0} = r^{-\frac{1}{2}} \cosh \pi\varepsilon \left[\begin{array}{c} -\Omega\, \Im\left\{(1+2i\varepsilon) r^{i\varepsilon} d_2\right\} \\ \Re\left\{(1+2i\varepsilon) r^{i\varepsilon} d_2\right\} \\ -\Lambda\, \Im\left\{(1+2i\varepsilon) r^{i\varepsilon} d_2\right\} \end{array}\right] . \tag{5.52}$$

For the square-root singular part of the solution from Eqs. (C.18), (5.8) and (5.51),

$$\left[\begin{array}{c} {}_1\sigma_{21} \\ {}_1\sigma_{22} \\ {}_1\sigma_{23} \end{array}\right]\Bigg|_{\theta=0} = \frac{1}{2} r^{-\frac{1}{2}} \left[\begin{array}{c} \dfrac{W_{23}}{W_{12}} \\ 0 \\ 1 \end{array}\right] d_3 \,. \tag{5.53}$$

By manipulating Eq. (5.52), the complex stress intensity factor in Eq. (5.9) may be defined as

$$K \equiv \lim_{r\to 0} \sqrt{2\pi r}\, r^{-i\varepsilon} \left(\sigma_{22} - i\Omega^{-1}\sigma_{21}\right)\Big|_{\theta=0} . \tag{5.54}$$

The amplitude of the square-root singularity K_{III} is obtained from Eq. (5.53) as

$$K_{III} \equiv \lim_{r\to 0} \sqrt{2\pi r}\, \sigma_{23}\Big|_{\theta=0} . \tag{5.55}$$

The unknown scalars d_2 and d_3 in Eqs. (5.52) and (5.53) are obtained by substituting the traction components given in Eqs. (5.52) and (5.53) into (5.54) and (5.55), respectively, yielding

$$d_2 = \frac{K}{\sqrt{2\pi}\,(1+2i\varepsilon)\cosh \pi\varepsilon}, \quad d_3 = \frac{2K_{III}}{\sqrt{2\pi}} . \tag{5.56}$$

Another definition for the stress intensity factors, for a bimaterial interface crack between two general anisotropic materials, may be found in [3, 9].

Recall that for the oscillatory part of the solution, three stress intensity factors exist. However, the solution is presented with the use of only two of them. A relation between two of the stress intensity factors will be derived in order to justify this proposition. It may be seen from the first and third rows of Eq. (5.52) that the shear stresses of the oscillatory solution along the interface are related by

$$\sigma_{23}\big|_{\theta=0} = \eta\sigma_{21}\big|_{\theta=0} \tag{5.57}$$

where

$$\eta = \frac{\Lambda}{\Omega} = -\frac{D_{13}W_{12} + D_{11}W_{23}}{D_{33}W_{12} + D_{13}W_{23}} . \tag{5.58}$$

Since the tractions along the interface are directly related to the stress intensity factors, the relation introduced in Eq. (5.57) implies that a relation between K_2 and K_3 exists. To this end, Eq. (5.54) may be rewritten as

$$\left(\sigma_{22} - i\Omega^{-1}\sigma_{21}\right)\Big|_{\theta=0} = \frac{Kr^{i\varepsilon}}{\sqrt{2\pi r}} . \tag{5.59}$$

When relating the complex stress intensity factors through the traction components σ_{22} and σ_{21}, K may be chosen as given in Eq. (5.9), where the imaginary part of K is taken as K_2. The reason for this choice is that K_2 is associated with σ_{21}. However, Eq. (5.57) implies that Eq. (5.59) may also be written with the use of σ_{23} as

$$\left(\sigma_{22} - i\Lambda^{-1}\sigma_{23}\right)\Big|_{\theta=0} = \frac{Kr^{i\varepsilon}}{\sqrt{2\pi r}} \tag{5.60}$$

where K is now taken as defined in Eq. (5.28). The choice of K in this form is a result of use of σ_{23}, which is associated with K_3. Hence, determination of the imaginary part of K depends on the relation used, which, in general, is arbitrary. As a result of Eqs. (5.57), (5.59) and (5.60)

$$K_2 = K_3 \ . \tag{5.61}$$

The square-root singular part of the solution consists of two stress intensity factors; however, only one is used in the representation of the solution. A relation between the stress intensity factors, which will be derived makes this possible. Equation (5.53) shows that K_I vanishes. The remaining stress intensity factors may be defined according to

$$K_{II} = \lim_{r\to 0} \sqrt{2\pi r}\ \sigma_{21}\Big|_{\theta=0} \tag{5.62}$$

$$K_{III} = \lim_{r\to 0} \sqrt{2\pi r}\ \sigma_{23}\Big|_{\theta=0} \ . \tag{5.63}$$

Substitution of the first and third rows in Eq. (5.53) into (5.62) and (5.63), respectively, and comparison, leads to

$$K_{II} = \frac{W_{23}}{W_{12}} K_{III} \ . \tag{5.64}$$

Hence, it is possible to write that

$$\sigma_{23}\Big|_{\theta=0} = \frac{K_{III}}{\sqrt{2\pi r}} \tag{5.65}$$

$$\sigma_{21}\Big|_{\theta=0} = \frac{W_{23}}{W_{12}} \frac{K_{III}}{\sqrt{2\pi r}} \tag{5.66}$$

The crack face displacement jumps in the vicinity of the crack tip are found to be

$$\Delta u_2 - i\Omega\,(\Delta u_1 + \eta \Delta u_3) = \frac{2D_{22}}{(1+2i\varepsilon)\cosh \pi\varepsilon} \sqrt{\frac{r}{2\pi}}\ K r^{i\varepsilon} \tag{5.67}$$

for the oscillatory, square-root singularity and

$$\Delta u_1 = 2\sqrt{\frac{r}{2\pi}} \left[D_{11} \left(\frac{W_{23}}{W_{12}} \right) + D_{13} \right] K_{III} \tag{5.68}$$

$$\Delta u_3 = 2\sqrt{\frac{r}{2\pi}} \left[D_{13} \left(\frac{W_{23}}{W_{12}} \right) + D_{33} \right] K_{III} \tag{5.69}$$

for the square-root singularity.

Substituting Eqs. (C.14) and (C.18) for the upper material and Eqs. (C.16) and (C.20) for the lower material into Eqs. (5.7) and (5.8), the stress components may be

written as

$$ {}_k\sigma_{ij} = \frac{1}{\sqrt{2\pi r}}\left[\Re\left(Kr^{i\varepsilon}\right)\ {}_k\Sigma_{ij}^{(1)}(\theta) + \Im\left(Kr^{i\varepsilon}\right)\ {}_k\Sigma_{ij}^{(2)}(\theta)\right] + \frac{K_{III}}{\sqrt{2\pi r}}\ {}_k\Sigma_{ij}^{(III)}(\theta) \tag{5.70} $$

where the complex stress intensity factor is defined in Eq. (5.9) and $i, j = 1, 2, 3$. In Eqs. (C.14) and (C.18), the expressions for $\mathbf{B}_1$ and $\mathbf{B}_1^{-1}$ are used for the upper material; for the lower material, the matrices $\mathbf{B}_2$ and $\mathbf{B}_2^{-1}$ are required for substitution into Eqs. (C.16) and (C.20). These matrices are found from Eqs. (B.11) and (B.12). It may be noted that all stress components have an oscillatory, square-root singular and square-root singular component. On the interface, the stress component $\sigma_{11}^{(k)}$ does not have a square-root singularity. The functions ${}_k\Sigma_{ij}^{(1)}(\theta)$, ${}_k\Sigma_{ij}^{(3)}(\theta)$ and ${}_k\Sigma_{ij}^{(II)}(\theta)$ in Eq. (5.70) are presented in [12].

Using Eqs. (C.13) and (C.17) for the upper material and Eqs. (C.15) and (C.19) for the lower material, the displacement components are found as

$$ {}_ku_i = \sqrt{\frac{r}{2\pi}}\left[\Re\left(Kr^{i\varepsilon}\right)\ {}_kU_i^{(1)}(\theta) + \Im\left(Kr^{i\varepsilon}\right)\ {}_kU_i^{(2)}(\theta)\right] + \sqrt{\frac{r}{2\pi}}K_{III}\ {}_kU_i^{(III)}(\theta)\ . \tag{5.71} $$

In Eqs. (C.13), (C.17), (C.15) and (C.19), the expressions for the matrices $\mathbf{A}_k$ and $\mathbf{B}_k^{-1}$ in Eqs. (B.1) and (B.12) are used for the upper and lower materials. The functions ${}_kU_i^{(1)}(\theta)$, ${}_kU_i^{(3)}(\theta)$ and ${}_kU_i^{(III)}(\theta)$ may be found in [12].

The Irwin crack closure integral in Eq. (3.45) with a coordinate transformation is written for the oscillatory, square-root singular part of the solution as

$$ \mathcal{G}_o = \lim_{\Delta a\to 0}\frac{1}{2\Delta a}\int_0^{\Delta a}\Re\left\{\left[\sigma_{22}(x_1) - i\Omega^{-1}\sigma_{21}(x_1)\right]\Big(\Delta u_2(\Delta a - x_1) + i\Omega\left[\Delta u_1(\Delta a - x_1) + \eta\,\Delta u_3(\Delta a - x_1)\right]\Big)\right\}\,dx_1\ . \tag{5.72} $$

The interface energy release rate related to the square-root singular part of the solution may be determined from

$$ \mathcal{G}_s = \lim_{\Delta a\to 0}\frac{1}{2\Delta a}\int_0^{\Delta a}\Big[\sigma_{21}(x_1)\Delta u_1(\Delta a - x_1) + \sigma_{22}(x_1)\Delta u_2(\Delta a - x_1) + \sigma_{23}(x_1)\Delta u_3(\Delta a - x_1)\Big]dx_1\ . \tag{5.73} $$

Substituting Eqs. (5.59) and (5.67) into (5.72), and substituting Eqs. (5.65), (5.66), (5.68) and (5.69) into (5.73), integrating and summing them leads to

$$ \mathcal{G}_i = \frac{1}{H_1}(K_1^2 + K_2^2) + \frac{1}{H_2}K_{III}^2 \tag{5.74} $$

where i represents interface, and

$$\frac{1}{H_1} = \frac{D_{22}}{4\cosh^2 \pi\varepsilon} \tag{5.75}$$

$$\frac{1}{H_2} = \frac{1}{4}\left[D_{11}\left(\frac{W_{23}}{W_{12}}\right)^2 + 2D_{13}\left(\frac{W_{23}}{W_{12}}\right) + D_{33}\right] . \tag{5.76}$$

The phase angles ψ and ϕ are defined in this case as

$$\psi = \tan^{-1}\left\{\frac{\Im(K\hat{L}^{i\varepsilon})}{\Re(K\hat{L}^{i\varepsilon})}\right\} \tag{5.77}$$

$$\phi = \tan^{-1}\left\{\sqrt{\frac{H_1}{H_2}}\frac{K_{III}}{\sqrt{K_1^2 + K_2^2}}\right\} \tag{5.78}$$

where H_1 and H_2 are given in Eqs. (5.75) and (5.76), respectively, and $\hat{L}$ is an arbitrary length parameter.

5.4 An Interface Between Two Woven Plies

In this section, a delamination is considered along the interface between two plain, balanced woven plies of material. A plain weave is one in which the weft alternates over and under the warp (see Fig. 5.2); the weave is balanced when the fiber volume fraction in the yarn in the weft and warp directions are equal. The upper material $k = 1$ (see Fig. 2.1) has fibers in the 0° and 90°-directions. The lower material is rotated about the x_2-axis by 45° so that it has fibers in the +45° and −45°-directions. Both materials are tetragonal and described by six independent mechanical properties. The compliance matrix is presented in Sect. B.4.

Many of the equations which describe the material in this section are exactly those in Appendix C. The precise expressions for D_{11}, D_{22} and D_{33} are taken from Eq. (B.36) with the appropriate values of the reduced compliance coefficients and $\beta_j^{(k)}$. These expressions are given in Sect. B.4. The displacement and stress function vectors for the upper material have the same form as those for the 0°//90° interface given in Eqs. (C.13) and (C.14) for the oscillatory, square-root singularity and Eqs. (C.17) and (C.18) for the square-root singularity. The lower material for this case is not mathematically degenerate. Hence, the equations to use are (C.15) and (C.16) for the oscillatory, square-root singularity and Eqs. (C.19) and (C.20) for the square-root singularity. Explicit expressions are presented in [5].

5.5 Afterward

In Sect. 5.1, it was mentioned that β in Eq. (5.2) was chosen to be negative in [2, 4] for the $0°//90°$ interface. It is recommended in [14] to take $\beta > 0$ without loss of generality. It may be pointed out that when exchanging the materials, that is upper is lower and lower is upper, the sign of β does not change as it does for two isotropic materials. Hence, in Sect. 5.1, β was taken to be positive. The effect of these choices are discussed here.

When $\beta > 0, \varepsilon > 0$. Then, the singularities are given in Eq. (C.12). An eigenvector is paired to each singularity as

$$\delta_1 = -\frac{1}{2} + i\varepsilon \leftrightarrow \boldsymbol{d} \tag{5.79}$$

$$\delta_2 = -\frac{1}{2} - i\varepsilon \leftrightarrow \overline{\boldsymbol{d}} \tag{5.80}$$

where $\mathbf{d}$ is given in Eq. (C.26) for the $0°//90°$ interface. If ε is chosen to be negative, namely $\hat{\varepsilon} = -|\varepsilon|$, this choice has no effect on the singularities, which remain

$$\hat{\delta}_1 = -\frac{1}{2} + i\hat{\varepsilon} = -\frac{1}{2} - i|\varepsilon| = \delta_2 \tag{5.81}$$

$$\hat{\delta}_2 = -\frac{1}{2} - i\hat{\varepsilon} = -\frac{1}{2} + i|\varepsilon| = \delta_1. \tag{5.82}$$

Following [14] (p. 427), the eigenvectors associated with the singularities are paired as

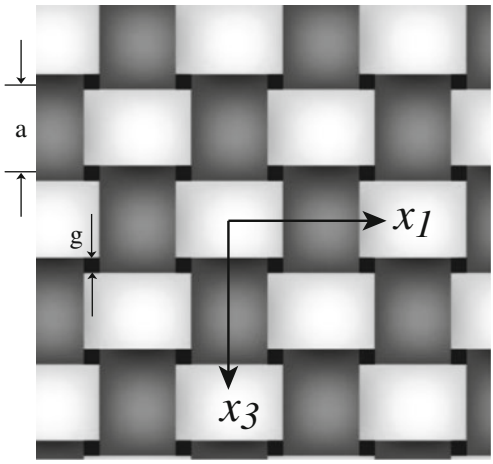

Fig. 5.2 Plain balanced weave

$$-\frac{1}{2} + i\hat{\varepsilon} \leftrightarrow \hat{\boldsymbol{d}} \tag{5.83}$$

$$-\frac{1}{2} - i\hat{\varepsilon} \leftrightarrow \overline{\hat{\boldsymbol{d}}} \tag{5.84}$$

where from Eq. (C.10), $\hat{\boldsymbol{d}}$ is in the form

$$\hat{\mathbf{d}}^T = \left[-i\sqrt{D_{22}/D_{11}}, 1, 0\right]\hat{d}_2 \,. \tag{5.85}$$

By determining the tractions for the oscillatory, square-root singular solution along the interface from Eq. (C.14), it is possible to write

$$\left(\sigma_{22} + i\sqrt{\frac{D_{11}}{D_{22}}}\sigma_{21}\right)\Big|_{\theta=0} = \frac{K_{\hat{\varepsilon}} r^{i\hat{\varepsilon}}}{\sqrt{2\pi r}} \tag{5.86}$$

where $K_{\hat{\varepsilon}}$ denotes the complex stress intensity factor associated with $\hat{\varepsilon}$. Substitution of the appropriate tractions into Eq. (5.86) yields

$$\hat{d}_2 = \frac{K_{\hat{\varepsilon}}}{\sqrt{2\pi}(1 + 2i\hat{\varepsilon})\cosh \pi\hat{\varepsilon}} \,. \tag{5.87}$$

It may be easily seen that the left hand side of Eq. (5.86) is the complex conjugate of the left hand side of Eq. (5.15). Taking the complex conjugate of Eq. (5.15) where $\varepsilon > 0$, comparing it to Eq. (5.86) and recalling that $\hat{\varepsilon} = -|\varepsilon|$, leads to a relation between the different definitions for K, which is

$$K_{\hat{\varepsilon}} = \overline{K}_{\varepsilon} \tag{5.88}$$

or explicitly

$$K_{1\,\hat{\varepsilon}} = K_{1\,\varepsilon} \qquad K_{2\,\hat{\varepsilon}} = -K_{2\,\varepsilon} \,. \tag{5.89}$$

Substituting Eq. (5.88) and $\hat{\varepsilon} = -|\varepsilon|$ into Eq. (5.87) shows that

$$\hat{d}_2 = \frac{\overline{K}_{\varepsilon}}{\sqrt{2\pi}(1 - 2i|\varepsilon|)\cosh \pi\varepsilon} \,. \tag{5.90}$$

Comparing Eq. (5.90) to $(5.14)_1$ shows

$$\hat{d}_2 = \overline{d}_2 \,. \tag{5.91}$$

Then from Eqs. (C.26), (5.85) and (5.91),

$$\hat{\mathbf{d}} = \overline{\mathbf{d}} \,. \tag{5.92}$$

Thus, the equations governing the displacement and stress function vectors in Eqs. (C.13), (C.14), (C.21) and (C.22) are identical for ε positive or negative. However, the definitions of the stress intensity factors differ as shown in Eq. (5.88).

Next, a different representation is used for the vector $\mathbf{d}$. In this case, $\mathbf{d}$ is expressed in terms of the arbitrary scalar d_1 rather than d_2 as

$$\mathbf{d}^T = \left[1, -i\sqrt{D_{11}/D_{22}}, 0\right] d_1 \ . \tag{5.93}$$

The tractions along the interface may be written from Eqs. (C.14) and (5.8) as

$$\left(-\sqrt{\frac{D_{22}}{D_{11}}}\sigma_{22} + i\sigma_{21}\right)\Big|_{\theta=0} = \frac{K_{\varepsilon}^{d_1} r^{i\varepsilon}}{\sqrt{2\pi r}} \ . \tag{5.94}$$

So that

$$d_1 = \frac{-i\, K_{\varepsilon}^{d_1}}{\sqrt{2\pi}(1+2i\varepsilon)\cosh \pi\varepsilon} \ . \tag{5.95}$$

It may be noted that K in Eq. $(5.14)_1$ is not the same as $K_{\varepsilon}^{d_1}$ in Eq. (5.95).

When a negative value of ε is taken, namely $\hat{\varepsilon} = -|\varepsilon|$, $\hat{\boldsymbol{d}}$ is given by

$$\hat{\mathbf{d}}^T = \left[1, i\sqrt{D_{11}/D_{22}}, 0\right] \hat{d}_1 \tag{5.96}$$

as may be found in [2]. In Eq. (5.96), $\hat{d}_1$ is an arbitrary complex constant and is found through

$$\left(\sqrt{\frac{D_{22}}{D_{11}}}\sigma_{22} + i\sigma_{21}\right)\Big|_{\theta=0} = \frac{K_{\hat{\varepsilon}}^{d_1} r^{i\hat{\varepsilon}}}{\sqrt{2\pi r}} \ . \tag{5.97}$$

Substitution of the appropriate tractions into Eq. (5.97), leads to

$$\hat{d}_1 = \frac{-i\, K_{\hat{\varepsilon}}^{d_1}}{\sqrt{2\pi}(1+2i\hat{\varepsilon})\cosh \pi\hat{\varepsilon}} \ . \tag{5.98}$$

It may be noted that $K_{\hat{\varepsilon}}$ in Eq. (5.87) is not the same as $K_{\hat{\varepsilon}}^{d_1}$ in Eq. (5.98). The left hand side of Eq. (5.97) may be obtained from the left hand side of Eq. (5.94) by taking the complex conjugate and multiplying by -1. Doing so, and comparing, leads to the relation

$$K_{\hat{\varepsilon}}^{d_1} = -\overline{K}_{\varepsilon}^{d_1} \tag{5.99}$$

or explicitly

$$K_{1\,\hat{\varepsilon}}^{d_1} = -K_{1\,\varepsilon}^{d_1} \qquad K_{2\,\hat{\varepsilon}}^{d_1} = K_{2\,\varepsilon}^{d_1} \ . \tag{5.100}$$

The definition of K, for a certain representation of $\mathbf{d}$, depends upon the sign of ε, which changes the relation between the tractions along the interface and K, as shown in Eqs. (5.12) and (5.86), and (5.94) and (5.97). In addition, it may be noted that the definition of K changes also as a result of the representation of $\mathbf{d}$. It may be seen from Eqs. (5.15) and (5.94) that

$$K^{d_1}_{\varepsilon>0} = -\sqrt{\frac{D_{22}}{D_{11}}} K^{d_2}_{\varepsilon>0} \tag{5.101}$$

for a positive value of ε; from Eqs. (5.86) and (5.97) that

$$K^{d_1}_{\varepsilon<0} = \sqrt{\frac{D_{22}}{D_{11}}} K^{d_2}_{\varepsilon<0}, \tag{5.102}$$

for a negative value of ε. It is concluded that investigators should be careful in comparing numerically obtained stress intensity factor values to account for possible differences in definitions. In the end, the field quantities and the interface energy release rates should be the same for the same problem. Recalling that K could also be defined by use of K_1 and K_3, as shown in Eq. (5.28), similar conclusions could be obtained. Finally, for the $+30°/-60°$ and $-30°/+60°$ interfaces discussed in Sect. 5.3, a similar exposition may be found in [12].

In Chap. 6, methods for calculating stress intensity factors with assistance from finite element analyses will be described. In addition, failure criteria will be presented in Chap. 7.

References

1. Aboudi J (2004) The generalized method of cells and high-fidelity generalized method of cells micromechanical models - a review. Mech Adv Mater Struct 11:329–366
2. Banks-Sills L, Boniface V (2000) Fracture mechanics for an interface crack between a special pair of transversely isotropic materials. In: Chuang T-J, Rudnicki JW (eds) Multiscale deformation and fracture in materials and structures–the James R. Rice 60th anniversary volume. Kluwer Academic Publishers, The Netherlands, pp 183–204
3. Banks-Sills L, Ikeda T (2011) Stress intensity factors for interface cracks between orthotropic and monoclinic materials. Int J Fract 167:47–56
4. Banks-Sills L, Boniface V, Eliasi R (2005) Development of a methodology for determination of interface fracture toughness of laminate composites-the 0°/90° pair. Int J Solids Struct 42:663–680
5. Banks-Sills L, Ishbir C, Fourman V, Rogel L, Eliasi R (2013) Interface fracture toughness of a multi-directional woven composite. Int J Fract 182:187–207
6. Dundurs J (1969) Edge-bonded dissimilar orthogonal elastic wedges under normal and shear loading. J Appl Mech 36:650–652
7. Freed Y, Banks-Sills L (2005) A through interface crack between a ±45° transversely isotropic pair of materials. Int J Fract 133:1–41

8. Hutchinson JW (1990) Mixed-mode fracture mechanics of interfaces. In: Rühle M, Evans AG, Ashby MF, Hirth JP (eds) Metal ceramic interfaces. Pergamon Press, Oxford, pp 295–301
9. Hwu C, Hu S (1992) Stress intensity factors and energy release rates of delaminations in composite laminates. Eng Fract Mech 42:977–988
10. Lekhnitskii SG (1950 in Russian; 1963, in English) Theory of elasticity of an anisotropic body. Holden-Day, San Francisco, translated by P. Fern
11. Rice JR (1988) Elastic fracture mechanics concepts for interfacial cracks. J Appl Mech 55:98–103
12. Rogel L, Banks-Sills L (2010) A through interface crack between a transversely isotropic pair of materials $(+30°/-60°, -30°/+60°)$. Eng Fract Mech 77:3261–3291
13. Stroh AN (1958) Dislocations and cracks in anisotropic elasticity. Philos Mag 7:625–646
14. Ting TCT (1996) Anisotropic elasticity-theory and applications. Oxford University Press, Oxford

Chapter 6
Methods of Calculating Stress Intensity Factors–Delaminations

Abstract In this chapter, methods for obtaining the stress intensity factors, interface energy release rate and phase angles are presented for interface cracks between two anisotropic materials. These methods include displacement extrapolation, the conservative interaction energy or M-integral and the Virtual Crack Closure Technique. Although these methods have been formulated with the finite element method in mind, they may be adapted to all numerical techniques which provide field quantities.

Keywords Displacement extrapolation method · Finite element method · M-integral · Thermal residual stresses · Virtual crack closure technique

The materials treated in this part of the book are laminates composed of either long fiber reinforced plies or woven plies. As mentioned previously, for each case the mechanical and thermal properties may be found by a homogenization procedure. For the materials described here, HFGMC [1] was used to determine effective properties. Hence, the materials described here are treated as homogeneous and anisotropic. The same material pairs considered in Chap. 5 are presented in this chapter. In Sect. 6.1, the displacement extrapolation method is presented. The M-integral is described in Sect. 6.2. In Sect. 6.3, the Virtual Crack Closure Technique is discussed.

6.1 Displacement Extrapolation

In this section, the displacement extrapolation method is described. If follows closely the description in Sect. 3.2 for a crack along the interface between two isotropic materials. The crack displacement jumps in Eq. (3.4) are used with $\theta = \pi$ and $-\pi$ with reference to Fig. 2.1. For a crack along the $0°//90°$ interface, the expression for the in-plane displacement jumps is given in Eq. (5.17) and rewritten here as

$$\Delta u_2 - i\sqrt{\frac{D_{22}}{D_{11}}}\Delta u_1 = \frac{8\cosh \pi\varepsilon}{H_1(1+2i\varepsilon)}\sqrt{\frac{r}{2\pi}}\, K r^{i\varepsilon} \tag{6.1}$$

which is similar to Eq. $(3.5)_1$ for two isotropic materials. The difference is the factor multiplying Δu_1 and H_1 which is found in Eq. (5.22). In Eq. (6.1) D_{11} and D_{22}

L. Banks-Sills, *Interface Fracture and Delaminations in Composite Materials*,
SpringerBriefs in Structural Mechanics, DOI 10.1007/978-3-319-60327-8_6

are found in Eqs. (B.37) and (B.38), respectively. The displacement jump in the x_3-direction is given in Eq. (5.18) and rewritten here as

$$\Delta u_3 = \frac{8}{H_2}\sqrt{\frac{r}{2\pi}}K_{III} \tag{6.2}$$

where for this material combination H_2 is given in Eq. (5.23) and D_{33} is given in Eq. (B.39). Solving for the in-plane local stress intensity factors from Eq. (6.1) and the out-of-plane mode III local stress intensity factor from Eq. (6.2), one may write

$$K_1^*(r) = \frac{\sqrt{2\pi(1+4\varepsilon^2)}}{8\cosh\pi\varepsilon}H_1\left\{\cos\chi\ \frac{\Delta u_2(r)}{\sqrt{r}} + \sqrt{\frac{D_{22}}{D_{11}}}\sin\chi\ \frac{\Delta u_1(r)}{\sqrt{r}}\right\} \tag{6.3}$$

$$K_2^*(r) = \frac{\sqrt{2\pi(1+4\varepsilon^2)}}{8\cosh\pi\varepsilon}H_1\left\{\sin\chi\ \frac{\Delta u_2(r)}{\sqrt{r}} - \sqrt{\frac{D_{22}}{D_{11}}}\cos\chi\frac{\Delta u_1(r)}{\sqrt{r}}\right\} \tag{6.4}$$

$$K_{III}^*(r) = \frac{\sqrt{2\pi}\ H_2}{8}\ \frac{\Delta u_3}{\sqrt{r}} \tag{6.5}$$

where χ is given in Eq. (3.9). Equations (6.3) and (6.4) are similar to Eqs. (3.6) and (3.7) differing by a factor of $\sqrt{D_{22}/D_{11}}$ on the second term in the curly brackets. Equation (6.5) is identical to Eq. (3.8). The difference in the equations is the expressions for H_1 and H_2 as noted above. The method delineated in Sect. 3.2 is the same one to be used here for the $0°//90°$ interface with Eq. (3.12).

For a crack along the $+45°//-45°$ interface, the expression for the displacement jumps in the x_2 and x_3-directions is given in Eq. (5.38) and rewritten here as

$$\Delta u_2 + i\sqrt{\frac{D_{22}}{D_{33}}}\Delta u_3 = \frac{8\cosh\pi\varepsilon}{H_1(1+2i\varepsilon)}\sqrt{\frac{r}{2\pi}}\ Kr^{i\varepsilon} \tag{6.6}$$

where H_1 is given in Eq. (5.43) and D_{22} and D_{33} are given in Eqs. (B.112) and (B.113), respectively. The displacement jump in the x_1-direction given in Eq. (5.39) is rewritten as

$$\Delta u_1 = \frac{8}{H_2}\sqrt{\frac{r}{2\pi}}K_{II} \tag{6.7}$$

where H_2 is given in Eq. (5.44) and D_{11} is given in Eq. (B.111). Solving for the stress intensity factors from Eqs. (6.6) and (6.7), one may write

$$K_1^*(r) = \frac{\sqrt{2\pi(1+4\varepsilon^2)}}{8\cosh\pi\varepsilon} H_1 \left\{ \cos\chi \, \frac{\Delta u_2(r)}{\sqrt{r}} - \sqrt{\frac{D_{22}}{D_{33}}} \sin\chi \, \frac{\Delta u_3(r)}{\sqrt{r}} \right\} \tag{6.8}$$

$$K_3^*(r) = \frac{\sqrt{2\pi(1+4\varepsilon^2)}}{8\cosh\pi\varepsilon} H_1 \left\{ \sin\chi \, \frac{\Delta u_2(r)}{\sqrt{r}} + \sqrt{\frac{D_{22}}{D_{33}}} \cos\chi \frac{\Delta u_3(r)}{\sqrt{r}} \right\} \tag{6.9}$$

$$K_{II}^*(r) = \frac{\sqrt{2\pi}\, H_2}{8} \frac{\Delta u_1}{\sqrt{r}} \tag{6.10}$$

where χ is given in Eq. (3.9). Equations (6.8) and (6.9) are similar to Eqs. (6.3) and (6.4) differing by a factor of $\sqrt{D_{22}/D_{33}}$ on the second term in the curly brackets. Equation (6.10) is similar to Eq. (6.5). The difference in the equations is the expressions for H_1 and H_2 as noted above. The method delineated in Sect. 3.2 is the same one to be used here for the $+45^\circ//-45^\circ$ interface with Eq. (3.12) replacing K_2 with K_3 and K_{III} with K_{II}. Expressions different than those in Eqs. (6.8)–(6.10) may be found in [5]. They are equivalent.

For a crack along a $+30^\circ//-60^\circ$ or a $-30^\circ//+60^\circ$ interface, the expression for the displacement jumps is given in Eq. (5.67) and rewritten here as

$$\Delta u_2 - i\Omega\left(\Delta u_1 + \eta \Delta u_3\right) = \frac{8\cosh\pi\varepsilon}{H_1(1+2i\varepsilon)} \sqrt{\frac{r}{2\pi}}\, K r^{i\varepsilon} \tag{6.11}$$

where Ω and η are given in Eqs. (5.48) and (5.58), respectively, and H_1 is given in Eq. (5.75). The parameter D_{22} may be found by following the development in Sect. B.3. The displacement jump for the square-root singularity may be written from Eqs. (5.68) and (5.69) as

$$\frac{W_{23}}{W_{12}} \Delta u_1 + \Delta u_3 = \frac{8}{H_2} \sqrt{\frac{r}{2\pi}} K_{III} \tag{6.12}$$

where H_2 is given in Eq. (5.76) and the parameters D_{11}, D_{13}, D_{33}, W_{12} and W_{23} may be found by following the development in Sect. B.3. Solving for the stress intensity factors from Eqs. (6.11) and (6.12), the local stress intensity factors become

$$K_1^*(r) = \frac{\sqrt{2\pi(1+4\varepsilon^2)}}{8\cosh\pi\varepsilon} H_1 \left\{ \cos\chi \, \frac{\Delta u_2(r)}{\sqrt{r}} + \Omega \sin\chi \left(\frac{\Delta u_1(r) + \eta \Delta u_3(r)}{\sqrt{r}} \right) \right\} \tag{6.13}$$

$$K_2^*(r) = \frac{\sqrt{2\pi(1+4\varepsilon^2)}}{8\cosh\pi\varepsilon} H_1 \left\{ \sin\chi \, \frac{\Delta u_2(r)}{\sqrt{r}} - \Omega \cos\chi \left(\frac{\Delta u_1(r) + \eta \Delta u_3(r)}{\sqrt{r}} \right) \right\} \tag{6.14}$$

$$K^*_{III}(r) = \frac{\sqrt{2\pi}\, H_2}{8} \left\{ \frac{W_{23}}{W_{12}} \frac{\Delta u_1}{\sqrt{r}} + \frac{\Delta u_3}{\sqrt{r}} \right\} \tag{6.15}$$

where χ is given in Eq. (3.9). Equations (6.13)–(6.15) are somewhat more complicated in form in comparison to the previous equations for the local stress intensity factors for the other interfaces considered. But they are implemented in the same way by extrapolating the local stress intensity factors to zero as in Eq. (3.12).

For the woven MD composite described in Sect. 5.4, the equations describing the displacement jumps have the same form as those in Sect. 5.1 for the $0°//90°$ interface, namely, Eqs. (5.17) and (5.18). Hence, Eqs. (6.3)–(6.5) may be used to carry out the extrapolation with the constants D_{11}, D_{22} and D_{33} chosen for the current interface. Other interfaces may easily be treated.

6.2 *M*-Integral

In this section, the M-integral is extended for the interfaces considered here for both mechanical and thermal loads. Only the three-dimensional version will be considered.

As for an interface crack between two isotropic materials as described in Sect. 3.3.1, two equilibrium solutions are considered. Solution (1) is the sought after solution and solution (2) is an auxiliary solution. The stress, strain and displacement components are given as a superposition of the two solutions in Eqs. (3.13)–(3.15). For the $0°//90°$, $+30°// - 60°$, $-30°// + 60°$ interfaces, as well as the multidirectional woven composite described in Sect. 5.4, the superposed stress intensity factors are given in Eqs. (3.16), (3.17) and (3.36). The same development presented for three dimensions in Sect. 3.3.2 is followed here leading to Eqs. (3.41)–(3.43) for the three stress intensity factors $K_1^{(1)}$, $K_2^{(1)}$ and $K_{III}^{(1)}$.

Consider the definitions of each of the parameters in Eqs. (3.41)–(3.43). For each interface, H_1 and H_2 are taken from the appropriate equations. For the $0°//90°$ interface, H_1 and H_2 are defined in Eqs. (5.22) and (5.23). In those equations, ε is found in Eqs. (5.1) and (B.44). The components of the matrices $\mathbf{D}$ and $\mathbf{W}$ are given in Eqs. (B.37)–(B.39) and (B.43). For the $+30°// - 60°$ and $-30°// + 60°$ interfaces, H_1 and H_2 are defined in Eqs. (5.75) and (5.76). The oscillatory parameter ε is found in Eqs. (5.1) and (B.140). The matrices $\mathbf{D}$ and $\mathbf{W}$, may be found in Eqs. (B.135) and (B.138). The components of the matrices may be calculated from $-\mathbf{A}_k\mathbf{B}_k^{-1}$ by multiplying the two matrices in Eqs. (B.1) and (B.12). By means of Eq. (5.6), it is possible to determine $\mathbf{S}_k\mathbf{L}_k^{-1}$ and $\mathbf{L}_k^{-1}$. Then use is made of Eqs. (5.4) and (5.5). For the interface in the MD woven composite, H_1 and H_2 are defined in Eqs. (5.22) and (5.23). The expression for the oscillatory parameter ε is found in Eqs. (5.1) and (B.44). To obtain the matrices $\mathbf{D}$ and $\mathbf{W}$, the matrix $\mathbf{A}_k\mathbf{B}_k^{-1}$ given in Eq. (B.34) is used with the appropriate values of the material eigenvalues and reduced compliance components. The components of the matrices $\mathbf{D}$ and $\mathbf{W}$ may be obtained from Eqs. (B.36) and (B.42), respectively.

The parameter A_1 in Eqs. (3.41)–(3.43) is the area shown in Fig. 3.6 between the delamination front and the curve created by the virtual crack extension. It is given in Eq. (3.38). The volume V_k consists of a slice of elements along the delamination front in the location of the virtual crack extension. The parameter $k = 1, 2$ represents the upper and lower materials. The cross-section of the volume depends upon which domain is used in the calculation as shown in Fig. 3.7. Recall that succeeding domains are used in the calculation by adding a ring of elements about the previous domain.

The field quantities containing a superscript (1), namely ${}_k\sigma_{ij}^{(1)}$, ${}_k\epsilon_{ij}^{(1)}$ and ${}_ku_i^{(1)}$ are, respectively, the stress, strain and displacement components of the sought after solution which is obtained by means of a finite element solution. The back subscript $k = 1, 2$ represents the upper and lower materials. The second or auxiliary solution ${}_k\sigma_{ij}^{(2\alpha)}$, ${}_k\epsilon_{ij}^{(2\alpha)}$ and ${}_ku_i^{(2\alpha)}$ is derived from the singular terms of the asymptotic expressions. There are three auxiliary solutions with $2\alpha = 2a, 2b, 2c$. For these solutions, Table 3.1 is used to define the stress intensity factors of solution (2). As an example, for the $0°//90°$ interface, the in-plane displacement components are given in Eq. (2.6) and the out-of-plane components are found in Eq. (2.7). The displacement functions ${}_kU_\alpha^{(1)}$, ${}_kU_\alpha^{(2)}$ and ${}_kU_\alpha^{(III)}$ are given in Eqs. (C.37)–(C.39). The stress and strain components are found by means of a finite element scheme, namely, the strain components are obtained by means of the displacements at the nodal points and the derivatives of the shape functions; the stress components are obtained by means of the constitutive law from the strains. All values are found at the integration points. The interaction strain energy density ${}_kW^{(1,2a)}$ in Eqs. (3.41)–(3.43) is given in Eq. (3.21). In Eqs. (3.41)–(3.43), δ_{1j} is the Kronecker delta. Finally, the normalized virtual crack extension is given in Eq. (3.39). For other interfaces, the appropriate asymptotic expressions for the displacement field are required. As mentioned previously, for the $+30°//-60°$ and $-30°//+60°$ interfaces, the expressions are found in [6]; for the MD woven composite laminate, they may be found in [3].

For the $+45°//-45°$ interface, the character of the solution changes. The amplitude of the oscillatory, square-root singularity is related to in-plane and out-of-plane deformations and given in Eq. (5.28); whereas, the amplitude of the square-root singularity is K_{II}. Hence, Eqs. (3.41)–(3.43) are replaced with

$$K_1^{(1)} = \frac{H_1}{2A_1} \sum_{k=1}^{2} \int_{V_k} \left[{}_k\sigma_{ij}^{(1)} \frac{\partial_k u_i^{(2a)}}{\partial x_1} + {}_k\sigma_{ij}^{(2a)} \frac{\partial_k u_i^{(1)}}{\partial x_1} - {}_kW^{(1,2a)}\delta_{1j} \right] \frac{\partial q_1}{\partial x_j} \, dV \; ; \tag{6.16}$$

$$K_{II}^{(1)} = \frac{H_2}{2A_1} \sum_{k=1}^{2} \int_{V_k} \left[{}_k\sigma_{ij}^{(1)} \frac{\partial_k u_i^{(2b)}}{\partial x_1} + {}_k\sigma_{ij}^{(2b)} \frac{\partial_k u_i^{(1)}}{\partial x_1} - {}_kW^{(1,2b)}\delta_{1j} \right] \frac{\partial q_1}{\partial x_j} \, dV \; ; \tag{6.17}$$

and

$$K_3^{(1)} = \frac{H_1}{2A_1} \sum_{k=1}^{2} \int_{V_k} \left[{}_k\sigma_{ij}^{(1)} \frac{\partial_k u_i^{(2c)}}{\partial x_1} + {}_k\sigma_{ij}^{(2c)} \frac{\partial_k u_i^{(1)}}{\partial x_1} - {}_kW^{(1,2c)}\delta_{1j} \right] \frac{\partial q_1}{\partial x_j} \, dV \; . \tag{6.18}$$

Actually, Eq. (6.16) is the same as Eq. (3.41). Of course, the definitions of some of the parameters change. As an example, H_1 and H_2 may be found in Eqs. (5.43) and (5.44). In those equations, ε is found in Eqs. (5.1) and (B.117). The components of the matrices **D** and **W** are given in Eqs. (B.111)–(B.113) and (B.116). The remainder of the quantities in Eqs. (6.16)–(6.18) are defined similarly to the way in which they were defined for other interfaces (see [5] for further details).

The thermal M-integral for all interfaces is the same as that in Eq. (3.44). The definitions of the various parameters in the expression for $M_N^{(1,2\alpha)}$ are the same as for the three-dimensional M-integral for applied force. The difference relates to the constitutive law and the definition of β_{ij}^k. The constitutive relation is given by

$$ {}_k\sigma_{ij} = {}_kC_{ijrs}\ {}_k\epsilon_{rs} - \beta_{ij}^k\vartheta \tag{6.19} $$

where ${}_kC_{ijrs}$ is the stiffness tensor which is the inverse of the compliance tensor and β_{ij}^k is defined for isotropic material in Eqs. (3.30) and (3.31). For anisotropic material,

$$ \beta_{ij}^k = {}_kC_{ijrs}\ {}_k\alpha_{rs} \tag{6.20} $$

where ${}_k\alpha_{rs}$ are the components of the coefficients of thermal expansion. As an example, for the $0°//90°$ interface using contracted notation,

$$ \beta_A = C_{11}\alpha_A + 2C_{12}\alpha_T \tag{6.21} $$

$$ \beta_T = C_{12}\alpha_A + (C_{22} + C_{23})\alpha_T \tag{6.22} $$

where the subscripts A and T refer to quantities in the axial and transverse direction. These expressions are for both upper and lower materials where axial and transverse directions are interchanged.

For the $+45°//-45°$ interface,

$$ \beta_{ij}^{(+45°)} = \begin{bmatrix} \frac{1}{2}(\beta_A + \beta_T) & 0 & -\frac{1}{2}(\beta_A - \beta_T) \\ & \beta_T & 0 \\ \text{sym} & & \frac{1}{2}(\beta_A + \beta_T) \end{bmatrix} \tag{6.23} $$

$$ \beta_{ij}^{(-45°)} = \begin{bmatrix} \frac{1}{2}(\beta_A + \beta_T) & 0 & \frac{1}{2}(\beta_A - \beta_T) \\ & \beta_T & 0 \\ \text{sym} & & \frac{1}{2}(\beta_A + \beta_T) \end{bmatrix}. \tag{6.24} $$

It may be noted that the coefficients of thermal expansion for the two weaves with yarn in the $0°/90°$-directions and the $+45°/-45°$-directions are the same. Hence, thermal curing stresses are minimal for these plies.

6.3 Virtual Crack Closure Technique

The virtual crack closure technique was presented in Sect. 3.4 for an interface crack between two dissimilar isotropic materials. Recently, the VCCT was extended for the $0°//90°$ interface [4]. That investigation followed the formulation presented in [2] in which the oscillatory parameter was chosen to be negative and d_1 was chosen as the arbitrary parameter as explained in Sect. 5.5, Eq. (5.96). In this section, ε is chosen to be positive and $\mathbf{d}$ defined in Eq. (C.26). The formulation used in this section relies on the development presented in Sect. 5.1. Note that the treatment here is two-dimensional.

The modes I and II energy release rates are given by

$$\mathcal{G}_I = \lim_{\Delta a \to 0} \frac{1}{2\Delta a} \int_0^{\Delta a} \sigma_{22}(x_1) \Delta u_2(\Delta a - x_1)\, dx_1 \tag{6.25}$$

$$\mathcal{G}_{II} = \lim_{\Delta a \to 0} \frac{1}{2\Delta a} \int_0^{\Delta a} \sigma_{21}(x_1) \Delta u_1(\Delta a - x_1)\, dx_1 \tag{6.26}$$

where Eqs. (6.25) and (6.26) are obtained from Eq. (3.45) by means of a coordinate transformation as may be seen in Fig. 3.8. In the derivation, define two auxiliary integrals

$$A_T = \frac{1}{2\Delta a} \int_0^{\Delta a} \left[\sigma_{22}(x_1) - i\sqrt{\frac{D_{11}}{D_{22}}}\sigma_{21}(x_1) \right] \left[\Delta u_2(\Delta a - x_1) + i\sqrt{\frac{D_{22}}{D_{11}}}\Delta u_1(\Delta a - x_1) \right] dx_1 \,. \tag{6.27}$$

$$D_T = \frac{1}{2\Delta a} \int_0^{\Delta a} \left[\sigma_{22}(x_1) - i\sqrt{\frac{D_{11}}{D_{22}}}\sigma_{21}(x_1) \right] \left[\Delta u_2(\Delta a - x_1) - i\sqrt{\frac{D_{22}}{D_{11}}}\Delta u_1(\Delta a - x_1) \right] dx_1 \tag{6.28}$$

where D_{11} and D_{22} are found in Eqs. (B.37) and (B.38), respectively. Using Eqs. (6.25)–(6.28), it is possible to show that the energy release rates for modes I and II are given by

$$\mathcal{G}_I = \frac{1}{2} \lim_{\Delta a \to 0} \left[\Re(A_T) + \Re(D_T) \right] \tag{6.29}$$

$$\mathcal{G}_{II} = \frac{1}{2} \lim_{\Delta a \to 0} \left[\Re(A_T) - \Re(D_T) \right] . \tag{6.30}$$

Substitution of Eqs. (6.29) and (6.30) into (3.49) results in

$$\mathcal{G}_i = \lim_{\Delta a \to 0} \Re(A_T) \,. \tag{6.31}$$

It may be shown that

$$A_T = \frac{D_{22}}{4\cosh^2 \pi\varepsilon} \left(K_1^2 + K_2^2\right) \tag{6.32}$$

so that

$$\mathcal{G}_i = \frac{1}{H_1} \left(K_1^2 + K_2^2\right) \tag{6.33}$$

where H_1 is given in Eq. (5.22) and $\mathcal{G}_i$ is given in the first term of Eq. (5.21).

By means of the imaginary components in Eq. (6.27), one may define

$$\mathcal{I}_I^{(T)} = \frac{1}{2\Delta a}\sqrt{\frac{D_{22}}{D_{11}}} \int_0^{\Delta a} \sigma_{22}(x)\Delta u_1(\Delta a - x)dx \tag{6.34}$$

$$\mathcal{I}_{II}^{(T)} = \frac{1}{2\Delta a}\sqrt{\frac{D_{11}}{D_{22}}} \int_0^{\Delta a} \sigma_{21}(x)\Delta u_2(\Delta a - x)dx \ . \tag{6.35}$$

Since A_T is real, $\Im(A_T) = 0$; so that by means of Eqs. (6.27), (6.34) and (6.35), it is possible to show that

$$\mathcal{I}_I^{(T)} = \mathcal{I}_{II}^{(T)} \ . \tag{6.36}$$

Calculation of the integral in Eq. (6.28) leads to

$$D_T = \frac{D_{22}}{4\pi\cosh \pi\varepsilon} P K^2 \Delta a^{2i\varepsilon} \ . \tag{6.37}$$

One may separate D_T into real and imaginary parts as

$$\Re(D_T) = \frac{1}{H_1}(K_1^2 + K_2^2)\, C \cos\chi \tag{6.38}$$

$$\Im(D_T) = \frac{1}{H_1}(K_1^2 + K_2^2)\, C \sin\chi \tag{6.39}$$

where H_1 is given in Eq. (5.22), C is defined in Eq. (3.55) and

$$\chi = 2\tan^{-1}\left(\frac{K_2}{K_1}\right) + \tan^{-1}\left(\frac{P_I}{P_R}\right) + 2\varepsilon \ln \Delta a \ . \tag{6.40}$$

The parameter $P = P_R + i\, P_I$ is defined in Eq. (3.54).

Following the development in Sect. 3.4 for two isotropic materials, the modes I and II energy release rates $\mathcal{G}_I$ and $\mathcal{G}_{II}$ are obtained from Eqs. (3.50) and (3.51), respectively. The sum of these energy release rates provides the interface energy release rate $\mathcal{G}_i$ given in Eq. (3.49); the quotient, provides g in Eq. (3.53). The phase angle ψ is calculated as in Eq. (3.52), leading to the stress intensity factors K_1 and K_2

given in Eq. (3.47). Since there are two pairs of stress intensity factors, the criterion in Eq. (3.56) is used to eliminate one pair. This criterion requires the crack faces to be open.

For other interfaces, the same analysis presented here may be carried out. All that is needed are the expressions for the traction along the interface and the crack face displacement jumps in the neighborhood of the crack tip, meaning equations analogous to Eqs. (5.15) and (5.17). The method can be extended to three dimensions. But very fine meshes are necessary to obtain accurate results [4].

References

1. Aboudi J (2004) The generalized method of cells and high-fidelity generalized method of cells micromechanical models - a review. Mech Adv Mater Struct 11:329–366
2. Banks-Sills L, Boniface V (2000) Fracture mechanics for an interface crack between a special pair of transversely isotropic materials. In: Chuang T-J, Rudnicki JW (eds) Multiscale deformation and fracture in materials and structures–the James R. Rice 60th anniversary volume. Kluwer Academic Publishers, The Netherlands, pp 183–204
3. Banks-Sills L, Ishbir C, Fourman V, Rogel L, Eliasi R (2013) Interface fracture toughness of a multi-directional woven composite. Int J Fract 182:187–207
4. Farkash E, Banks-Sills L (2017) Virtual Crack Closure Technique for an interface crack between two transversely isotropic materials. Int J Fract 205:189–202
5. Freed Y, Banks-Sills L (2005) A through interface crack between a $\pm 45^\circ$ transversely isotropic pair of materials. Int J Fract 133:1–41
6. Rogel L, Banks-Sills L (2010) A through interface crack between a transversely isotropic pair of materials ($+30^\circ/-60^\circ$, $-30^\circ/+60^\circ$). Eng Fract Mech 77:3261–3291

Chapter 7
Testing–Delamination Between Two Dissimilar Plies

Abstract In this chapter, results are presented for the fracture toughness or critical interface energy release rate under mixed mode conditions. Deterministic and probabilistic criteria are considered. In addition, beam type specimens which are recommended in international standards are presented.

Keywords Beam type specimens · Brazilian disk specimen · Confidence · Cross-ply · Failure curve · Failure surface · Fracture toughness · Probability · R-curve

In this chapter, tests performed on two multi-directional (MD) laminates will be described. These tests follow those presented in Chap. 4. These results are considered in Sect. 7.1. In Sect. 7.2, testing of beam type specimens is discussed.

7.1 Failure of a Delamination in a Cross-Ply

Composite plies containing long fibers in an epoxy matrix prepreg AS4/3502 were formed into a cross-ply laminate. A cross-ply laminate is one in which the fibers in the adjacent plies form an angle of 90°. A plate of this material was fabricated and composite strips containing a delamination formed from a Teflon film were machined. The delamination was along the interface between two plies: either $0°//90°$ [10] or $+45°// -45°$ [11].

In Fig. 7.1a, a Brazilian disk specimen containing a composite strip with three layers, each about 4 mm wide, is shown. The layers consist of plies with fibers in the 0° and 90°-directions. A delamination is indicated along the interface between plies whose fibers are in the 0° and 90°-directions. Partial disks of aluminum were glued to the composite strip to complete the Brazilian disk specimens. Although the load is applied only to the composite at various angles ω, the aluminum partial disks allow for easier handling of the specimen and accurate placement in the loading frame. Recall that varying the angle ω results in various mode mixities. The radius of the disk is nominally 20 mm and its nominal thickness is 8 mm. In Fig. 7.1b, a variation of the specimen in Fig. 7.1a is shown. In this specimen, the inner part of the composite strip consists of three layers with plies in the 0°, 90° and 0°-directions. Each layer

L. Banks-Sills, *Interface Fracture and Delaminations in Composite Materials*,
SpringerBriefs in Structural Mechanics, DOI 10.1007/978-3-319-60327-8_7

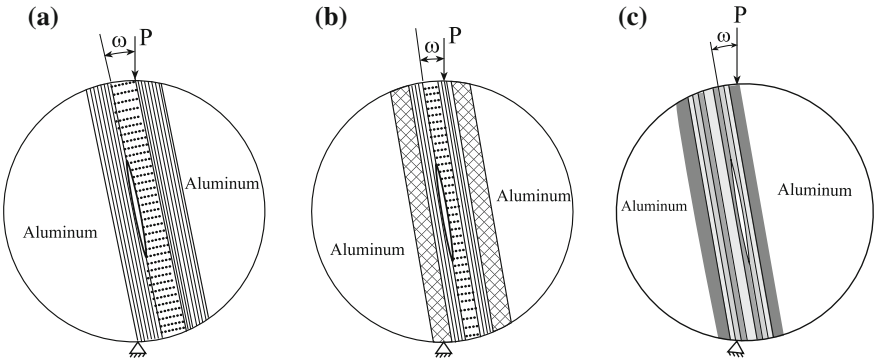

Fig. 7.1 Brazilian disk specimens. Composite specimens containing **a** $[0°//90°/0°]$ strip, **b** $[0°//90°/0°]$ strip with $\pm 45°$ outer stiffening layers and **c** $[0, -45, +45, 0]_s$ strip with $\pm 45°$ outer stiffening layers

Table 7.1 Some effective material properties of a graphite/epoxy (AS4/3502) fiber reinforced composite ($V_f = 0.62$)

E_A (GPa)	E_T (GPa)	G_A (GPa)	ν_A	ν_T	$\alpha_A/°\text{C}$	$\alpha_T/°\text{C}$
138	9.7	4.6	0.32	0.46	-0.5×10^{-6}	36.6×10^{-6}

is nominally 0.5 mm wide. The Teflon strip forming the delamination is between a 0° and 90° ply. There are outer plies alternating in the ±45°-directions to prevent bending of the composite plate when it was cured. In Fig. 7.1c, the second interface is shown which is between +45° and −45° plies. The layup is more complex than the previous specimens. The composite consists of an inner part $[0, -45, +45, 0]_s$ with each layer of nominal width 0.54 mm with outer stiffening layers of ±45° which are about 4.05 mm wide. The 0° plies where inserted in order to prevent buckling of the specimen.

The effective material parameters for one layer of the material were obtained by means of the generalized method of cells [32] and are presented in Table 7.1; recall that E_A and E_T are the Young's moduli in the axial and transverse directions, respectively; ν_A and ν_T are Poisson's ratios in the axial and transverse directions, respectively; G_A is the axial shear modulus, $G_T = E_T/2(1 + \nu_T)$, α_A and α_T are the coefficients of thermal expansion in the axial and transverse directions, respectively. The composite contained a fiber volume fraction, $V_f = 0.62$.

Twenty-four specimens containing a delamination between the 0° and 90° plies were tested with results reported in [10]. The normalized crack length ranged between $0.36 \leq a/R \leq 0.43$, where R is the specimen radius; the specimen thickness ranged between 7.82 mm $\leq B \leq$ 8.20 mm; and the loading angles ranged between $-10° \leq \omega \leq 10°$. Recall that the delamination was actually a thin notch created by a strip of Teflon film with a thickness of about 25.4 μm. The oscillatory parameter, found from

Eqs. (5.1) and (B.44) was $\varepsilon = -0.03627$. The composite layer in the specimens was cured at 177 °C; so that the temperature change ϑ was taken to be 150 °C.

The problem was treated in two dimensions. Hence, the two-dimensional M-integral in Eqs. (3.25)–(3.28) was used to determine the stress intensity factors $K_1^{(f)}$ and $K_2^{(f)}$ arising from applied loading (see [8]). The thermal curing stresses were also accounted for following [9] and using Eq. (3.34) to obtain $K_1^{(r)}$ and $K_2^{(r)}$. It may be noted that the equations presented in Sect. 3.3.1 were for a bimaterial crack between two isotropic materials. The M-integrals take the same form for two anisotropic materials except that the correct constitutive law and the appropriate values for H_1 are required. Employing the superposed stress intensity factors $K_1^{(T)}$ and $K_2^{(T)}$, the interface energy release rate $\mathcal{G}_i$ and the phase angle ψ are calculated. The former is obtained from Eq. (5.21) with $K_{III} = 0$ and $H_1 = 16.35$ GPa as calculated from Eq. (5.22); the latter is obtained from Eq. (5.25) with $\hat{L} = 100$ μm. It may be noted that the sign of the oscillatory parameter ε was taken to be negative in [10].

The failure curve presented for two isotropic materials and given in Eq. (4.1) may be used here. The data points for this case are plotted in Fig. 7.2. It may be noted that the data points from the specimens in Fig. 7.1b fall within the scatter of those of the type in Fig. 7.1a. The value of $\overline{\mathcal{G}}_{1c} = 26.2$ N/m was found by taking the average of the values in Eq. (2.23) for all tests with H_1 obtained from Eq. (5.22). The standard error of $\overline{\mathcal{G}}_{1c}$ is 2.3 N/m. Equation (4.1) is plotted as the black curve in Fig. 7.2. The curve which predicts a 10% probability of unexpected failure using the t-statistic may be found by making use of Eqs. (2.26), (2.27) and (2.29). The value of $\mathcal{G}_{1c}^*$ is found from Eq. (2.26) with a standard deviation $s = 11.5$ N/m and the value of $t_{0.1,23} = 1.32$, so that $K = 1.35$ and $\mathcal{G}_{1c}^* = 10.7$ N/m. The curve in Eq. (2.27) is plotted in red in Fig. 7.2. For this curve, there is a 10% probability that the next data point will be

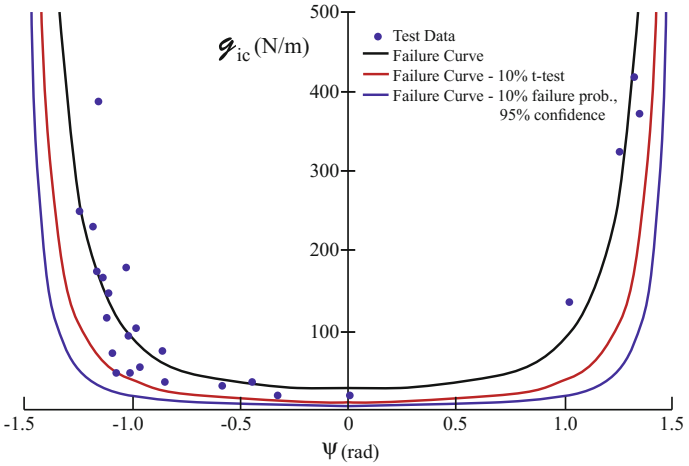

Fig. 7.2 Failure curves and test points for the 0°//90° delamination in the graphite/epoxy AS4/3502 laminate ($\overline{\mathcal{G}}_{1c} = 26.2$ N/m, $\mathcal{G}_{1c}^* = 10.7$ N/m using the t-statistic, $\mathcal{G}_{1c}^* = 5.1$ N/m using the z-variate model and $\hat{L} = 100$ μm)

below this curve and the specimen or structure will fail unexpectedly. Indeed, there is one data point from the test data below the curve. For a failure curve with a 10% probability of unexpected failure and a 95% confidence, the expression in Eq. (2.30) is used. The value of $z_{0.1} = -1.28$ and $z_{0.95} = 1.64$ leading to a value of $K = 1.84$ and $\mathcal{G}_{1c}^{*} = 5.1$ N/m. Plotting Eq. (2.27) with this value of $\mathcal{G}_{1c}^{*}$ leads to the blue curve in Fig. 7.2. This time, there are no test points below the curve.

Next, the specimens with the delamination along the $+45°//-45°$ interface of the graphite/epoxy AS4/3502 composite are considered [11]. In this case, the in-plane and out-of-plane fields are coupled. Hence, three-dimensional finite element analyses were carried out to obtain the stress intensity factors resulting from the applied load and thermal stresses. The analyses accounted for delamination eccentricity, varying layer height, specimen thickness and diameter, loading angle, and load at failure. The three-dimensional mechanical M-integral was used to obtain $K_1^{(f)}$, $K_3^{(f)}$ and $K_{II}^{(f)}$ from Eqs. (6.16)–(6.18) (see [21] for details). The stress intensity factors resulting from the residual stresses $K_1^{(r)}$, $K_3^{(r)}$ and $K_{II}^{(r)}$ were also determined (see [11]). The composite strip in the specimens was cured at 177 °C; so that the temperature change ϑ was taken to be 150 °C. Twenty-six specimens containing a delamination between the $+45°$ and $-45°$ plies were tested with results reported in [11]. The normalized crack length $a/R \sim 0.38$, the thickness ranged between $7.94 \text{ mm} \leq B \leq 8.17 \text{ mm}$ and the loading angles ranged between $2° \leq \omega \leq 13°$. It may be noted that the crack was actually a thin notch created by a strip of Teflon film which was about 25.4 μm thick. The oscillatory parameter, found from Eqs. (5.1) and (B.117) was $\varepsilon = 0.000615$.

From the total stress intensity factors, values of $\mathcal{G}_i$, ψ and ϕ were calculated by means of Eqs. (5.42), $(5.45)_1$ and $(5.46)_1$, respectively, and plotted in Fig. 7.3a, b. The values of H_1 and H_2 given in Eqs. (5.43) and (5.44) are 11.46 GPa and 14.48 GPa,

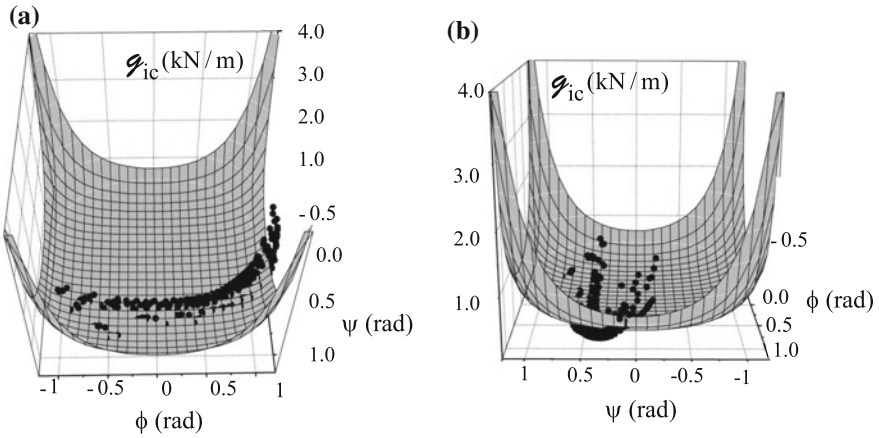

Fig. 7.3 Deterministic failure surface and test points for the $+45°//-45°$ delamination of the graphite/epoxy AS4/3502 laminate ($\overline{\mathcal{G}}_{1c} = 92.4$ N/m and $\hat{L} = 200$ μm). **a** View as a function of ϕ and **b** view as a function of ψ

respectively. It should be noted that there are 21 points along the delamination front for each specimen. Hence, there are 546 data points. The value of $\overline{\mathcal{G}}_{1c} = 92.4$ N/m was found by taking the average of the values in Eq. (2.23) with a standard error of 1.25 N/m. It may be noted in passing that in [11], $\overline{\mathcal{G}}_{1c}$ was given as 90.3 N/m. In that case, the average values of $\hat{K}_1^{(T)}$ were used to calculate $\overline{\mathcal{G}}_{1c}$. Equation (2.25) is plotted as the surface in Fig. 7.3a, b. It may be observed that for a given specimen the data points along the delamination front are nearly a function of ϕ with little change in ψ. This is a result of the dominant behavior of K_1 and K_{II} with secondary behavior for K_3. This may be seen clearly in Fig. 7.3a. The failure surface behaves in the same manner as the failure curve. For points below the surface, from a deterministic point of view, the structure should be safe. However, failure points below the failure curve may be observed in Fig. 7.3b.

It may be noted that the 546 samples are not all independent. For each specimen, there are 21 points along the delamination front. For eight of the specimens, points along the delamination front intersect the failure surface. It was postulated in [11] for these specimens that some of the points along the crack front have become critical and drag the rest of the crack front with them as the delamination propagates. For seven of the specimens, all of the points are above the surface; whereas for 11 of them, all of the points are below. This behavior is considered as experimental scatter. The specimens for which the points are all below the failure curve in Fig. 7.3 are the troublesome ones, since one should assume that there is no failure for those values of $\mathcal{G}_i$, ψ and ϕ. Hence, as before, a statistical approach is taken.

First, the t-statistic is used which predicts a 10% probability that a $\mathcal{G}_{ic}$ value will be unexpectedly below the surface. The value of $\mathcal{G}_{1c}^*$ is found by means of Eqs. (2.26) and (2.29) with the standard deviation $s = 29.3$ N/m and the value of $t_{0.1,545} = 1.28$, so that $K = 1.28$ and $\mathcal{G}_{1c}^* = 54.8$ N/m. The surface in Eq. (2.28) is plotted in Fig. 7.4. There is a 10% probability that the next data point will be below this surface; that

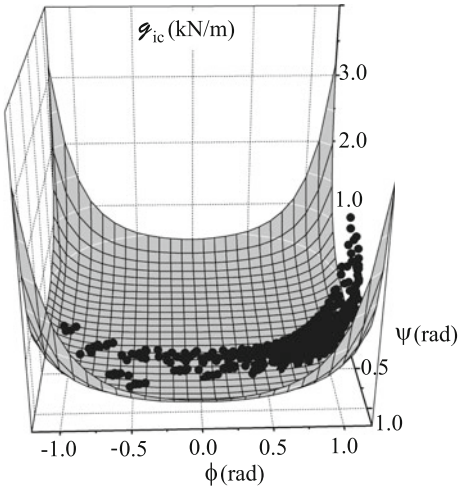

Fig. 7.4 Ten percent (10%) failure surface obtained with the t-statistic and test points for the $+45°//-45°$ delamination of the graphite/epoxy AS4/3502 laminate; ($\mathcal{G}_{1c}^* = 54.8$ N/m and $\hat{L} = 200$ μm)

is, that it will fail even though it is in the safe region. Some points from two of the specimens are below this failure surface. Hence, as postulated in [11], all of the specimens tested would be expected to fail based on the failure surface obtained with the t-statistic. For a 10% failure surface with a 95% confidence, the expression in Eq. (2.30) is used. The value of $z_{0.1} = -1.28$ and $z_{0.95} = 1.64$ leading to a value of $K = 1.38$ and $\mathcal{G}_{1c}^{*} = 51.9$ N/m. Plotting Eq. (2.28) with this value of $\mathcal{G}_{1c}^{*}$ leads to a surface similar to the one in Fig. 7.4. There are still several points below the failure surface for two specimens. Either failure surface obtained by the statistical approach is a good choice to predict failure.

The main advantage of Brazilian disk specimens is that with one specimen and test setup, one is able to obtain a wide range of mode mixities.

7.2 Beam Type Specimens

It is common to carry out quasi-static fracture toughness tests on composite laminates with beam type specimens. These include the double cantilever beam (DCB) specimen shown in Fig. 7.5 for mode I testing; the edge notch flexure (ENF) specimen shown in Fig. 7.6 and the calibrated end loaded split (C-ELS) specimen shown in Fig. 7.7a for mode II testing; and the mixed mode bending (MMB) and mixed mode end loaded split (MMELS) specimen shown in Fig. 7.8 and 7.7b, respectively, for mixed mode deformation. In these figures a_0 is the initial delamination length, h or $2h$ is the specimen thickness, b is the specimen width, L and l are longitudinal length measures and c is the lever arm.

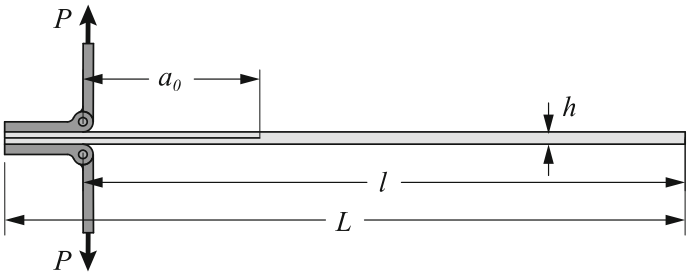

Fig. 7.5 Double cantilever beam specimen with piano hinges

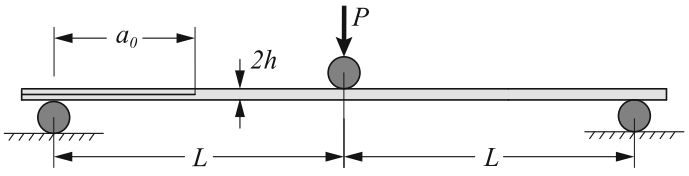

Fig. 7.6 Edge notch flexure specimen

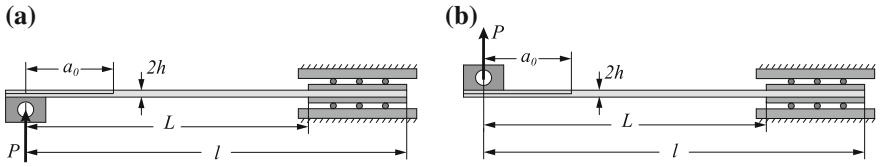

Fig. 7.7 **a** C-ELS and **b** MMELS specimens

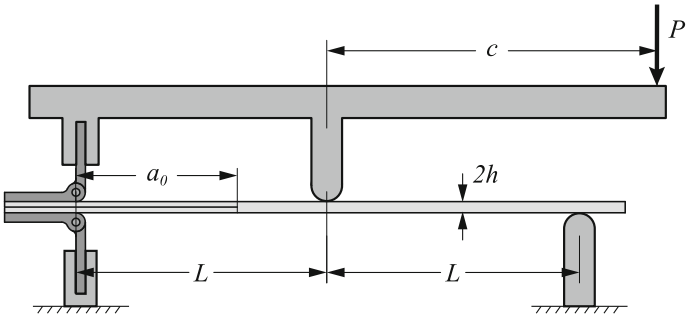

Fig. 7.8 Mixed mode bending specimen

For unidirectional (UD) composite material, there are two standards for the DCB test [5, 26]. There is a standard for ENF specimens also for UD composites [7], as well as the C-ELS specimen [27]. For mixed mode and UD composites, there is a standard [6] making use of MMB specimens. Progress is being made to develop a standard for the MMELS specimen, also for UD composites.

Tests have been performed on DCB specimens fabricated from both UD and MD composites to determine the mode I energy release rate $\mathcal{G}_{Ic}$ [4, 15–17, 23, 30, 35]. In many cases, graphite/epoxy material was tested. For a $0°//90°$ interface, a fracture toughness of $\mathcal{G}_{Ic} = 140$ N/m was found in [30] where the delamination propagated along the interface. For angle ply laminates higher values were obtained because of the damage that occurred. In [15, 16], it was found that for MD composites the mode I fracture toughness was independent of ply orientation when the delamination propagated along the interface. Values as low as 86 N/m were found. In reviewing the literature, it was found in [4] that mode I initiation toughness was affected moderately by the interface lay-up and delamination growth direction relative to the fiber direction. For MD specimens it was found in [23] that as specimen width increased the distribution of $\mathcal{G}_I$ along the interface became more uniform. The directions of the plies adjacent to the interface were shown to affect the $\mathcal{G}_{Ic}$ values.

Fracture tests reported in Sect. 7.1 were conducted with a Brazilian disk specimen on carbon/epoxy material with $0°//90°$ and $+45°// - 45°$ interfaces. The minimum interface energy release rate was found to be 26.5 N/m for the former interface and 92.4 N/m for the latter. For the former, a two-dimensional failure curve was derived; for the latter a three-dimensional failure surface was obtained.

There have also been measurements of fracture toughness for woven composites. As a result of the interlaced yarn, woven composites produce complicated fracture mechanisms. The fracture toughness of a woven composite depends on the deformation type, the weave pattern, the fabric geometry and process, the volume fraction of the fibers and the crack propagation direction. Values of $\mathcal{G}_{Ic}$ may be obtained by conducting mode I fracture tests, although these may produce small shear components for MD lay-ups.

Toughness tests on woven composites with all plies in the same directions were reported in [2, 3, 13, 22, 29, 31]. Both carbon/epoxy and glass/epoxy woven materials were considered. In addition to mode II and mixed mode tests, DCB specimens were tested in [2, 3]. For the latter, R-curve behavior was found for 5H-satin specimens made with carbon fibers. The behavior was influenced by the direction of the delamination relative to the warp and weft directions. Two DCB specimen sets consisting of plain weave E-glass/epoxy were tested in [29]. In one set, the fibers were in the $0^\circ/90^\circ$ directions, and in the other set, the weave was rotated by 45° in the plane with respect to the loading direction. Values of $\mathcal{G}_{Ic}$ were less for the rotated laminate. In [22], 5H-satin carbon/epoxy woven DCB specimens were tested. It was found that higher fiber volume fraction and more transverse tows along the delamination plane result in higher fracture toughness. DCB specimens were tested in [13] to investigate the fracture behavior of E-glass woven fabric composites. The weave was unbalanced with 55% of the fibers in the warp direction and 45% in the weft direction. There was great variability between the results. Tests were carried out for multi-directional woven composites in [34]. The material was a crowsfoot satin woven fabric glass reinforced epoxy. DCB specimens with different stacking sequences including the following delamination interfaces were tested: between $0^\circ/90^\circ$ and $\theta/(\theta + 90^\circ)$ weaves, and between $\theta/(\theta + 90^\circ)$ and $-\theta/(-\theta + 90^\circ)$ weaves. It was observed that the $\mathcal{G}_{Ic}$ values for delamination initiation for the $0^\circ/90^\circ$ and $\theta/(\theta + 90^\circ)$ were independent of θ.

In [12], quasi-static fracture toughness tests were carried out on DCB, MD, woven composite specimens containing a delamination. The load P is applied through the piano hinges. Each ply in the specimen is a balanced plain weave of carbon fiber yarn in an epoxy matrix. For woven composites, a balanced weave is composed of yarn which has the same fiber volume fraction in the weft and warp directions. The plies are laid up so that they alternate between a $0^\circ/90^\circ$ and a $+45^\circ/-45^\circ$ weave. There are 15 plies with the delamination located between the seventh and eighth plies. Thus, the interface is between a $0^\circ/90^\circ$ weave and a $+45^\circ/-45^\circ$ weave. Each of these plies is taken to be effectively anisotropic and hence tetragonal.

The fibers in the composite were carbon T300 which are transversely isotropic; hence, they are described by five independent elastic constants and two thermal constants. These include E_A and E_T which are the axial and transverse Young's moduli, respectively, ν_A and ν_T, the axial and transverse Poisson's ratios, respectively, G_A, the axial shear modulus and the transverse shear modulus, $G_T = E_T/2(1 + \nu_T)$. The thermal properties are α_A and α_T, respectively, the axial and transverse thermal coefficients of expansion. The epoxy matrix is 913 which is isotropic and described by two independent elastic constants: Young's modulus E, Poisson's ratio ν and

Table 7.2 Mechanical properties for T300 [28]; for epoxy 913 [38]. Thermal properties for T300 and epoxy 913 [14, 37]

Material	E_A (GPa)	E_T (GPa)	G_A (GPa)	ν_A	ν_T	α_A ($\times 10^{-6}/°C$)	α_T ($\times 10^{-6}/°C$)
Graphite T300	230	8	27.3	0.26	0.30	−0.41	10.08
Epoxy 913	3.4			0.41		43.92	

Table 7.3 Mechanical properties of the woven composite measured by Israel Aerospace Industries [20]

$E_{11} = E_{33}$ (GPa)	G_{13} (GPa)	ν_{13}
59.6	3.9	0.07

the coefficient of thermal expansion α. Their mechanical and thermal properties are presented in Table 7.2. There is a range of properties in the literature for carbon T300. The mechanical properties of the T300 carbon fibers may be found in [28]; those of epoxy were taken from [38]. The axial CTE of the T300 carbon is given in the Torayka data sheet [37]; its transverse component was taken from [14]. For the epoxy, the value given for three other epoxies in [14] was taken for the epoxy 913. The fiber volume fraction for this material was not obtained experimentally. The material was produced by Hexcel with an apparent fiber volume fraction within the weave of 51% [24].

Each ply in the specimen is a balanced, plain weave; a sketch of the $0°/90°$ layer is shown in Fig. 5.2. Mechanical properties measured by Israel Aerospace Industries (IAI, [20]) are presented in Table 7.3. The subscripts on the mechanical properties are with reference to the coordinate system in Fig. 5.2. Note that the x_2-coordinate is perpendicular to the plane of the weave.

The mechanical and thermal properties were calculated by means of HFGMC (for details of the method see [1, 18]). To achieve this value, it was assumed that the fiber volume fraction within the yarn is 63% and the yarn volume fraction within the weave is 81%. Multiplying these together gives the desired fiber volume fraction of 51% within the weave. In addition, measurements were made of the geometric properties of the weave. The parameters are shown in Fig. 5.2 where a is the yarn width, g is the distance between yarns and h is the thickness of a ply. They were taken as $a = 1.7$ mm, $g = 0.4$ mm and $h = 0.24$ mm. Using the mechanical properties in Table 7.2 and the geometrical parameters as input into the HFGMC Graphical User Interface [18] produced the mechanical properties shown in Table 7.4. In Table 7.4, $E_{11} = E_{33}$ are the Young's moduli in the x_1 and x_3-directions, respectively, that is, the in-plane elastic moduli (see Fig. 5.2); E_{22} is the out-of-plane Young's modulus; G_{13} is the in-plane shear modulus and $G_{23} = G_{21}$ are the out-of-plane shear moduli; ν_{13} is the in-plane Poisson's ratio and $\nu_{23} = \nu_{21}$ are the out-of-plane Poisson's ratios. Note that

Table 7.4 Mechanical properties of the plain woven composites ($V_f = 0.51$)

Ply type	$E_{11} = E_{33}$ (GPa)	E_{22} (GPa)	G_{13} (GPa)	$G_{23} = G_{21}$ (GPa)	ν_{13}	$\nu_{23} = \nu_{21}$
0°/90°	57.3	7.6	3.9	2.5	0.04	0.07
+45°/ − 45°	13.6	7.6	27.6	2.5	0.77	0.07
Effective material	41.2	7.6	15.7	2.5	0.31	0.07

$$\frac{\nu_{ij}}{E_{ii}} = \frac{\nu_{ji}}{E_{jj}} \tag{7.1}$$

where summation is not implied. The ply type which is denoted as 0°/90° is the weave as shown in Fig. 5.2. It may be observed in Table 7.4 that the material in this direction is tetragonal, so that there are six independent elastic constants. Comparison may be made to values which were measured and presented in Table 7.3. The in-plane Young's moduli differ by less than 4%; the in-plane shear moduli agree; and there are great differences between the Poisson's ratios. It may be noted that this is a very small quantity and difficult to measure. In the specimens, there are also plies in the +45°/ − 45° direction. By rotating the properties about the x_2-axis in Fig. 5.2 by 45°, they are obtained as shown in Table 7.4; this ply is also represented by six independent mechanical properties. In the finite element model, two plies on each side of the delamination are modeled with these properties. In addition, to save on computational resources, effective properties of the woven laminate are found and presented in Table 7.4. This material is quasi-isotropic in the x_1–x_3 plane. As expected, the CTEs in the x_1 and x_3-directions are identical. Hence, thermal residual stresses caused by curing and minimalized.

Eight delamination toughness tests were carried out on DCB specimens. The specimens were fabricated by IAI. The tests were performed in the spirit of the ASTM standard D5528 [5]. Details may be found in [12]. Further testing of five DCB specimens was presented in [36] with an updated test protocol. Results for a $\mathcal{G}_{IR}$-curve from that study are presented in Fig. 7.9. The numbers of each specimen are given in the figure; FT represents fracture toughness, the second number 03 or 04 represents the batch number; the third number represents the number in the test series. In Fig. 7.9, the results of the five fracture toughness tests are presented with respect to the delamination growth from the Teflon insert front $\Delta a = a - a_0$, showing that the test results for both batches share the same scatter. Furthermore, a clear R-curve behavior may be observed. According to [5] for UD laminates, as the delamination grows from the insert, the fracture toughness values will initially increase monotonically reaching a plateau. However, when examining the results of mode I fracture toughness tests preformed on specimens with an MD layup, it appears that this stable phase is not always reached (see [33]). Nonetheless, the fracture toughness results of the tests presented here exhibit the typical behavior previously observed for UD composites. It should be noted that Fig. 7.9 is similar to

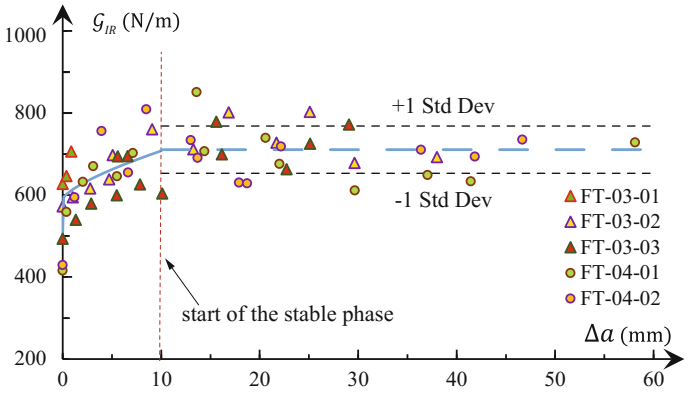

Fig. 7.9 Fracture toughness test results and R-curve behavior [36]

Table 7.5 Average fracture toughness values for all specimens shown in Fig. 7.9

Phase	Δa (mm)	$\mathcal{G}_{IR}$ (N/m)
Initial	0	508
Monotonic rise	$0 < \Delta a < 10$	$586 + 27(\Delta a)^{0.65}$
Stable	$10 < \Delta a$	711

the figure given in [19], marking the initiation of the plateau region with ± 1 standard deviation boundary lines.

It appears that in the case of the specimens from batch 4, an initial phase was also present. This initial phase is defined as the fracture toughness obtained for an artificial delamination formed by the Teflon insert. The $\mathcal{G}_{IR}$ values for this phase were significantly lower than that found for the other phases, as may be observed in Fig. 7.9 for specimens FT04-01 and FT04-02 at $\Delta a = 0$. Lower values may be related to the presence of resin pockets near the insert edge. Note that the Teflon insert thickness used here was nominally 25.4 μm, while the ASTM D-5528-13 standard [5] prescribes the insert thickness to be no greater than 13 μm. A summary of the results for the three phases is presented in Table 7.5. The fracture toughness values for $\Delta a = 0$ and $\Delta a > 10$ are average values. The fracture toughness values for the range $0 < \Delta a < 10$ are presented using a power-like law.

The eight mode I fracture toughness tests which were reported in [12] were carried out on batch 1 of the same material described above. For that batch, the $\mathcal{G}_{IR}$ values were higher. For example, for $\Delta a = 0$, $\mathcal{G}_{IR} = 670$ N/m as compared to $\mathcal{G}_{IR} = 508$ N/m, for batches 3 and 4. It is known that different batches of the same material produce different properties. Moreover, the environmental conditions in the earlier study, were not well controlled.

Fatigue delamination propagation tests were carried out on DCB specimens fabricated from this material. Results may be found in [25, 36].

References

1. Aboudi J (2004) The generalized method of cells and the high-fidelity generalized method of cells micromechanical models-a review. Mech Adv Mater Struct 11:329–366
2. Alif N, Carlsson LA, Gillespie JW (1997) Mode I, mode II and mixed mode fracture of woven fabric carbon/epoxy. In: Hooper SJ (ed) Composite materials: testing and design (Thirteenth Volume), ASTM STP 1242. American Society for Testing and Materials, West Conshohocken, pp 82–106
3. Alif N, Carlsson LA, Boogh L (1998) The effect of weave pattern and crack propagation direction on mode I delamination resistance of woven glass and carbon composites. Compos Part B-Eng 29B:603–611
4. Andersons J, König M (2004) Dependence of fracture toughness of composite laminates on interface ply orientations and delamination growth direction. Compos Sci Technol 64:2139–2152
5. ASTM Standard D5528-13 (2014) Standard test method for mode I interlaminar fracture toughness of unidirectional fiber-reinforced polymer matrix composites. In: Space simulation; aerospace and aircraft; composite materials, vol. 15.03. ASTM International, West Conshohocken, pp 289–301
6. ASTM Standard D6671-13e1 (2014) Test method for mixed mode I - mode II interlaminar fracture toughness of unidirectional fiber-reinforced polymer matrix composites. In: Space simulation; aerospace and aircraft; composite materials, vol. 15.03. ASTM International, West Conshohocken, pp 429–438
7. ASTM Standard D7905-14 (2015) Standard test method for determination of the mode II interlaminar fracture toughness of unidirectional fiber-reinforced polymer matrix composites. In: Space simulation; aerospace and aircraft; composite materials, vol. 15.03. ASTM International, West Conshohocken, pp 718–735
8. Banks-Sills L, Boniface V (2000) Fracture mechanics for an interface crack between a special pair of transversely isotropic materials. In: Chuang T-J, Rudnicki, JW (eds) Multiscale deformation and fracture in materials and structures–the James R. Rice 60th anniversary volume. Kluwer Academic Publishers, The Netherlands, pp 183–204
9. Banks-Sills L, Dolev O (2004) The conservative M-integral for thermal-elastic problems. Int J Fract 125:149–170
10. Banks-Sills L, Boniface V, Eliasi R (2005) Development of a methodology for determination of interface fracture toughness of laminate composites-the $0°/90°$ pair. Int J Solids Struct 42:663–680
11. Banks-Sills L, Freed Y, Eliasi R, Fourman V (2006) Fracture toughness of the $+45°/-45°$ interface of a laminate composite. Int J Fract 141:195–210
12. Banks-Sills L, Ishbir C, Fourman V, Rogel L, Eliasi R (2013) Interface fracture toughness of a multi-directional woven composite. Int J Fract 182:187–207
13. Blake SP, Berube KA, Lopez-Anido RA (2011) Interlaminar fracture toughness of woven E-glass fabric composites. J Compos Mater 46:1583–1593
14. Bowles DE, Tompkins SS (1989) Prediction of coefficients of thermal expansion for unidirectional composites. J Compos Mater 23:370–388
15. Chai H (1984) The characterization of mode I delamination failure in non-woven multidirectional laminates. Compos 15:277–290
16. Chai H (1986) On the correlation between the mode I failure of adhesive joints and laminated composites. Eng Fract Mech 24:413–431
17. de Morais AB, de Moura MF, Goncalves JPM, Camanho PP (2003) Analysis of crack propagation in double cantilever beam tests of multidirectional laminates. Mech Mater 35:641–652
18. Decad D, Aboudi J, Banks-Sills L (2007) Micromechanics-based modeling of woven composite materials. In: Idan M (ed) Proceedings of the 47th Israel annual conference on aerospace sciences. Technion, Haifa, Israel
19. Dharmawan F, Simpson G, Herszberg I, John S (2006) Mixed mode fracture toughness of GFRP composites. Compos Struct 75:328–338

20. Freed Y (2009) Personal communication
21. Freed Y, Banks-Sills L (2005) A through interface crack between a $\pm 45^{\circ}$ transversely isotropic pair of materials. Int J Fract 133:1–41
22. Gill A, Robinson P, Pinho S (2009) Effect of variation in fibre volume fraction on modes I and II delamination behaviour of 5H-satin woven composites manufactured by RTM. Compos Sci Technol 69:2368–2375
23. Gong XJ, Hurez A, Verchery G (2010) On the determination of delamination toughness by using multidirectional DCB specimens. Polym Test 29:658–666
24. Hexcel composite properties calculator (2012). http://www.hexcel.com:82/calculators/src/CompositeProps2WithBleed.aspx?mc=23&mt=2&ft=0&fw=140&rc=30&mc_v=1.242&ft_v=1.79&fw_v=170&rc_v=40. Accessed 14 Oct 2012
25. Ishbir C, Banks-Sills L, Fourman V, Eliasi R (2014) Delamination propagation in a multi-directional woven composite DCB specimen subjected to fatigue loading. Compos Part B Eng 66:180–189
26. ISO Standard 15024 (2001) Fibre-reinforced plastic composites - determination of mode I interlaminar fracture toughness, G_{IC}, for unidirectionally reinforced materials. International Standards Organization, Switzerland
27. ISO Standard 15114 (2014) Fibre-reinforced plastic composites - determination of the mode II fracture resistance for unidirectionally reinforced materials using the calibrated end-loaded split (C-ELS) test and an effective crack length approach. International Standards Organization, Switzerland
28. Miyagawa H, Sato C, Mase T, Drown E, Drzal LT, Ikegami K (2005) Transverse elastic modulus of carbon fibers measured by Raman spectroscopy. Mater Sci Eng A 412:88–92
29. Naik NK, Reddy KS, Meduri S, Raju NB, Prasad PD, Azad SKNM, Ogde PA, Reddy BCK (2002) Interlaminar fracture characterization for plain weave fabric composites. J Mater Sci 37:2983–2987
30. Nicholls DJ, Gallagher JP (1983) Determination of G_{IC} in angle ply composites using a cantilever beam test method. J Reinf Plast Compos 2:2–17
31. Nikbakht M, Choupani C (2009) Experimental investigation of mixed-mode fracture behaviour of woven laminated composite. J Mater Sci 44:3428–3437
32. Paley M, Aboudi J (1992) Micromechanical analysis of composites by the generalized cells model. Mech Mater 14:127–139
33. Peng L, Zhang J, Zhao L, Bao R, Yang H, Fei B (2011) Mode I delamination growth of multidirectional composite laminates under fatigue loading. J Compos Mater 45:1077–1090
34. Pereira AB, de Morais AB, de Moura MFSF, Magalhaes AG (2005) Mode I interlaminar fracture of woven glass/epoxy multidirectional laminates. Compos Part A, Appl Sci Manuf 36:1119–1127
35. Robinson P, Song DQ (1992) A modified DCB specimen for mode I testing of multidirectional laminates. J Compos Mater 26:1554–1577
36. Simon I, Banks-Sills L, Fourman V (2017) Mode I delamination propagation and R-ratio effects in woven composite DCB specimens for a multi-directional layup. Int J Fatigue 96:237–251
37. Torayka T300 Data Sheet (2012). http://www.aerosol.co.il/files/article/1315850055u55QN.pdf. Accessed 13 Oct 2012
38. Yee JCH, Pellegrino S (2005) Folding of woven composite structures. Compos Part A, Appl Sci Manuf 36:273–278

Appendix A
Stress and Displacement Functions for the First Term of the Asymptotic Expansion of an Interface Crack Between Two Linear Elastic, Homogeneous and Isotropic Materials

The stress and displacement functions for the first term of the asymptotic expansion of an interface crack between two linear elastic, homogeneous and isotropic materials are presented here. For material (1), the upper material, the stress functions in Eq. (2.1) are given by [1]

$$
\begin{aligned}
{}_1\Sigma_{11}^{(1)}(\theta,\varepsilon) = & -\frac{1}{\cosh \pi\varepsilon}\left\{\left[\sinh(\pi-\theta)\varepsilon - e^{-(\pi-\theta)\varepsilon}\right]\cos\frac{\theta}{2}\right. \\
& \left.+\frac{1}{2}e^{-(\pi-\theta)\varepsilon}\sin\theta\left[\sin\frac{3\theta}{2} - 2\varepsilon\cos\frac{3\theta}{2}\right]\right\} \qquad \text{(A.1)} \\
{}_1\Sigma_{12}^{(1)}(\theta,\varepsilon) = & \frac{1}{\cosh \pi\varepsilon}\left\{-\sinh(\pi-\theta)\varepsilon\ \sin\frac{\theta}{2}\right. \\
& \left.-\frac{1}{2}e^{-(\pi-\theta)\varepsilon}\sin\theta\left[-\cos\frac{3\theta}{2} - 2\varepsilon\sin\frac{3\theta}{2}\right]\right\} \qquad \text{(A.2)} \\
{}_1\Sigma_{22}^{(1)}(\theta,\varepsilon) = & \frac{1}{\cosh \pi\varepsilon}\left\{\left[\sinh(\pi-\theta)\varepsilon + e^{-(\pi-\theta)\varepsilon}\right]\cos\frac{\theta}{2}\right. \\
& \left.+\frac{1}{2}e^{-(\pi-\theta)\varepsilon}\sin\theta\left[\sin\frac{3\theta}{2} - 2\varepsilon\cos\frac{3\theta}{2}\right]\right\} \qquad \text{(A.3)} \\
{}_1\Sigma_{11}^{(2)}(\theta,\varepsilon) = & -\frac{1}{\cosh \pi\varepsilon}\left\{\left[\cosh(\pi-\theta)\varepsilon + e^{-(\pi-\theta)\varepsilon}\right]\sin\frac{\theta}{2}\right. \\
& \left.+\frac{1}{2}e^{-(\pi-\theta)\varepsilon}\sin\theta\left[\cos\frac{3\theta}{2} + 2\varepsilon\sin\frac{3\theta}{2}\right]\right\} \qquad \text{(A.4)} \\
{}_1\Sigma_{12}^{(2)}(\theta,\varepsilon) = & \frac{1}{\cosh \pi\varepsilon}\left\{\cosh(\pi-\theta)\varepsilon\ \cos\frac{\theta}{2}\right. \\
& \left.-\frac{1}{2}e^{-(\pi-\theta)\varepsilon}\sin\theta\left[\sin\frac{3\theta}{2} - 2\varepsilon\cos\frac{3\theta}{2}\right]\right\} \qquad \text{(A.5)}
\end{aligned}
$$

L. Banks-Sills, *Interface Fracture and Delaminations in Composite Materials*, SpringerBriefs in Structural Mechanics, DOI 10.1007/978-3-319-60327-8

$$ {}_1\Sigma_{22}^{(2)}(\theta,\varepsilon) = \frac{1}{\cosh\pi\varepsilon}\left\{\left[\cosh(\pi-\theta)\varepsilon + e^{-(\pi-\theta)\varepsilon}\right]\sin\frac{\theta}{2} + \frac{1}{2}e^{-(\pi-\theta)\varepsilon}\sin\theta\left[\cos\frac{3\theta}{2} + 2\varepsilon\sin\frac{3\theta}{2}\right]\right\} . \tag{A.6} $$

For the upper material, the out-of-plane stress functions in Eq. (2.5) are given by

$$ {}_1\Sigma_{31}^{(III)}(\theta) = -\sin\frac{\theta}{2} \tag{A.7} $$

$$ {}_1\Sigma_{32}^{(III)}(\theta) = \cos\frac{\theta}{2} . \tag{A.8} $$

For material (1), the upper material, the displacement functions in Eq. (2.6) are given by

$$ {}_1U_1^{(1)} = -\frac{1}{\mu_1(1+4\varepsilon^2)\cosh\pi\varepsilon}\left\{\left[\sinh(\pi-\theta)\varepsilon - \frac{\kappa_1-1}{2}e^{-(\pi-\theta)\varepsilon}\right]\cos\frac{\theta}{2} - \frac{1}{2}(1+4\varepsilon^2) \times e^{-(\pi-\theta)\varepsilon}\sin\theta\sin\frac{\theta}{2} + 2\varepsilon\left[\cosh(\pi-\theta)\varepsilon + \frac{\kappa_1-1}{2}e^{-(\pi-\theta)\varepsilon}\right]\sin\frac{\theta}{2}\right\} \tag{A.9} $$

$$ {}_1U_2^{(1)} = \frac{1}{\mu_1(1+4\varepsilon^2)\cosh\pi\varepsilon}\left\{\left[\cosh(\pi-\theta)\varepsilon + \frac{\kappa_1-1}{2}e^{-(\pi-\theta)\varepsilon}\right]\sin\frac{\theta}{2} - \frac{1}{2}(1+4\varepsilon^2) \times e^{-(\pi-\theta)\varepsilon}\sin\theta\cos\frac{\theta}{2} - 2\varepsilon\left[\sinh(\pi-\theta)\varepsilon - \frac{\kappa_1-1}{2}e^{-(\pi-\theta)\varepsilon}\right]\cos\frac{\theta}{2}\right\} \tag{A.10} $$

$$ {}_1U_1^{(2)} = \frac{1}{\mu_1(1+4\varepsilon^2)\cosh\pi\varepsilon}\left\{\left[\cosh(\pi-\theta)\varepsilon + \frac{\kappa_1-1}{2}e^{-(\pi-\theta)\varepsilon}\right]\sin\frac{\theta}{2} + \frac{1}{2}(1+4\varepsilon^2) \times e^{-(\pi-\theta)\varepsilon}\sin\theta\cos\frac{\theta}{2} - 2\varepsilon\left[\sinh(\pi-\theta)\varepsilon - \frac{\kappa_1-1}{2}e^{-(\pi-\theta)\varepsilon}\right]\cos\frac{\theta}{2}\right\} \tag{A.11} $$

$$ {}_1U_2^{(2)} = \frac{1}{\mu_1(1+4\varepsilon^2)\cosh\pi\varepsilon}\left\{\left[\sinh(\pi-\theta)\varepsilon - \frac{\kappa_1-1}{2}e^{-(\pi-\theta)\varepsilon}\right]\cos\frac{\theta}{2} + \frac{1}{2}(1+4\varepsilon^2) \times e^{-(\pi-\theta)\varepsilon}\sin\theta\sin\frac{\theta}{2} + 2\varepsilon\left[\cosh(\pi-\theta)\varepsilon + \frac{\kappa_1-1}{2}e^{-(\pi-\theta)\varepsilon}\right]\sin\frac{\theta}{2}\right\} . \tag{A.12} $$

where μ_1 is the shear modulus of the upper material and κ_1 is defined in Eq. (2.4). For the upper material, the out-of-plane displacement in Eq. (2.7) is given by

$$ {}_1U_3^{(III)} = \frac{2}{\mu_1}\sin\frac{\theta}{2} . \tag{A.13} $$

For material (2), the lower material, replace π with $-\pi$ in Eqs. (A.1)–(A.6) and (A.9)–(A.12). In addition, replace μ_1 by μ_2 and κ_1 by κ_2 in Eqs. (A.9)–(A.13).

Reference

1. Deng X (1993) General crack-tip fields for stationary and steadily growing interface cracks in anisotropic bimaterials. J Appl Mech 60:183–189

Appendix B
Matrices $\mathbf{A}_k$, $\mathbf{B}_k$ and $\mathbf{B}_k^{-1}$ for Different Anisotropic Material Pairs

In this appendix, the matrices $\mathbf{A}_k$, $\mathbf{B}_k$ and $\mathbf{B}_k^{-1}$ which appear in Eq. (5.6) and are employed to calculate the oscillating part of the singularity ε in Eq. (5.1) are presented. They are also used to obtain the asymptotic expressions for the stress function and displacement vectors given in Eqs. (C.13)–(C.20). The subscript k represents the upper and lower materials, 1 and 2, respectively.

Following [5] (pp. 170–171), the complex 3×3 matrices $\boldsymbol{A}$, $\boldsymbol{B}$ and $\boldsymbol{B}^{-1}$ are presented here for a general anisotropic material. The subscript k has been omitted. The components in the matrices take on the values of the upper and lower materials where appropriate. The matrix $\boldsymbol{A}$ is given by

$$\boldsymbol{A} = \begin{bmatrix} k_1\xi_1(p_1) & k_2\xi_1(p_2) & k_3\eta_1(p_3) \\ k_1 p_1^{-1}\xi_2(p_1) & k_2 p_2^{-1}\xi_2(p_2) & k_3 p_3^{-1}\eta_2(p_3) \\ k_1 p_1^{-1}\xi_4(p_1) & k_2 p_2^{-1}\xi_4(p_2) & k_3 p_3^{-1}\eta_4(p_3) \end{bmatrix}, \tag{B.1}$$

where for $\alpha = 1, 2, 4$ and $\beta = 1, 2$

$$\xi_\alpha(p_\beta) = p_\beta^2 s'_{\alpha 1} - p_\beta s'_{\alpha 6} + s'_{\alpha 2} + \lambda_\beta(p_\beta s'_{\alpha 5} - s'_{\alpha 4}) \tag{B.2}$$

$$\eta_\alpha(p_3) = \lambda_3(p_3^2 s'_{\alpha 1} - p_3 s'_{\alpha 6} + s'_{\alpha 2}) + (p_3 s'_{\alpha 5} - s'_{\alpha 4})\,. \tag{B.3}$$

For a general anisotropic material, there are 21 independent compliance coefficients which may be written in contracted form as a 6×6 matrix $s_{\alpha\beta}$, $\alpha, \beta = 1, \ldots, 6$. These coefficients may be written in a reduced form as

$$s'_{\alpha\beta} = s_{\alpha\beta} - \frac{s_{\alpha 3} s_{3\beta}}{s_{33}} = s'_{\beta\alpha} \tag{B.4}$$

L. Banks-Sills, *Interface Fracture and Delaminations in Composite Materials*,
SpringerBriefs in Structural Mechanics, DOI 10.1007/978-3-319-60327-8

where $s'_{\alpha 3} = s'_{3\beta} = 0$. The parameters λ_i are given as

$$\lambda_\beta = -\frac{\ell_3(p_\beta)}{\ell_2(p_\beta)} = -\frac{\ell_4(p_\beta)}{\ell_3(p_\beta)}, \quad \text{for } \beta = 1, 2 \tag{B.5}$$

$$\lambda_3 = -\frac{\ell_2(p_3)}{\ell_3(p_3)} = -\frac{\ell_3(p_3)}{\ell_4(p_3)} \, . \tag{B.6}$$

The sextic functions ℓ_i, $i = 2, 3, 4$, are defined as

$$\ell_2 = s'_{55}p^2 - 2s'_{45}p + s'_{44} \tag{B.7}$$

$$\ell_3 = s'_{15}p^3 - (s'_{14} + s'_{56})p^2 + (s'_{25} + s'_{46})p - s'_{24} \tag{B.8}$$

$$\ell_4 = s'_{11}p^4 - 2s'_{16}p^3 + (2s'_{12} + s'_{66})p^2 - 2s'_{26}p + s'_{22} \, . \tag{B.9}$$

The eigenvalues p for each material are found as solutions of the sextic equation

$$\ell_2(p)\ell_4(p) - \ell_3(p)\ell_3(p) = 0 \, . \tag{B.10}$$

It has been shown that Eq. (B.10) has three complex conjugate solutions. The three solutions with a positive imaginary part are taken in the expressions presented above. The normalization factors k_1, k_2 and k_3 are not required in the calculations. For each fiber direction, the matrix $\boldsymbol{A}$ in Eq. (B.1) is obtained by substitution of the various parameters found for that material direction.

The matrix $\boldsymbol{B}$ is given by

$$\boldsymbol{B} = \begin{bmatrix} -k_1 p_1 & -k_2 p_2 & -k_3 p_3 \lambda_3 \\ k_1 & k_2 & k_3 \lambda_3 \\ -k_1 \lambda_1 & -k_2 \lambda_2 & -k_3 \end{bmatrix} \tag{B.11}$$

and

$$\boldsymbol{B}^{-1} = \frac{1}{\Delta} \begin{bmatrix} -k_1^{-1}(1 - \lambda_2\lambda_3) & -k_1^{-1}(p_2 - \lambda_2\lambda_3 p_3) & -k_1^{-1}\lambda_3(p_2 - p_3) \\ k_2^{-1}(1 - \lambda_1\lambda_3) & k_2^{-1}(p_1 - \lambda_1\lambda_3 p_3) & k_2^{-1}\lambda_3(p_1 - p_3) \\ k_3^{-1}(\lambda_1 - \lambda_2) & k_3^{-1}(\lambda_1 p_2 - \lambda_2 p_1) & -k_3^{-1}(p_1 - p_2) \end{bmatrix} \tag{B.12}$$

where

$$\Delta = p_1 - p_2 + \lambda_3[\lambda_1 p_2 - \lambda_2 p_1 - p_3(\lambda_1 - \lambda_2)] \, . \tag{B.13}$$

In the following sections, explicit expressions for the matrices are presented for materials with fibers in different directions. The matrices are related to the mechanical properties of each material.

B.1 The 0°/90° Pair

In this section, the matrices are presented for the 0°//90° interface. Each of the materials is transversely isotropic with respect to the delamination front coordinates in Fig. 2.1. For the upper material with $k = 1$, the fibers are in the x_1-direction. The compliance matrix is given by

$$\boldsymbol{s}^{(1)} = \begin{bmatrix} \frac{1}{E_A} & \frac{-\nu_A}{E_A} & \frac{-\nu_A}{E_A} & 0 & 0 & 0 \\ & \frac{1}{E_T} & \frac{-\nu_T}{E_T} & 0 & 0 & 0 \\ & & \frac{1}{E_T} & 0 & 0 & 0 \\ & & & \frac{1}{G_T} & 0 & 0 \\ & & \text{sym} & & \frac{1}{G_A} & 0 \\ & & & & & \frac{1}{G_A} \end{bmatrix} . \tag{B.14}$$

The mechanical properties E_A, E_T, G_A, G_T, ν_A and ν_T are the Young's moduli in the axial and transverse directions, respectively, the shear moduli in the axial and transverse directions, respectively, and the axial and transverse Poisson's ratios. Since the material is transversely isotropic,

$$G_T = \frac{E_T}{2(1+\nu_T)} . \tag{B.15}$$

For the lower material, Eq. (B.14) is rotated by 90° about the x_2-axis. For the upper material, the reduced compliance coefficients in Eq. (B.4) are given by

$$s_{11}'^{(1)} = \left(1 - \nu_A^2 \frac{E_T}{E_A}\right) \frac{1}{E_A} \tag{B.16}$$

$$s_{12}'^{(1)} = s_{21}'^{(1)} = -(1+\nu_T)\frac{\nu_A}{E_A} \tag{B.17}$$

$$s_{22}'^{(1)} = \frac{(1-\nu_T^2)}{E_T} \tag{B.18}$$

$$s_{44}'^{(1)} = \frac{2(1+\nu_T)}{E_T} \tag{B.19}$$

$$s_{55}'^{(1)} = s_{66}'^{(1)} = \frac{1}{G_A} . \tag{B.20}$$

All other compliance coefficients are zero.

Regarding the eigenvalues of the compatibility equations p_j ($j = 1.2.3$), it may be observed that $\ell_3(p) \equiv 0$ in Eq. (B.8), and solution of Eq. (B.10) leads to

$$p_j^{(1)} = i\beta_j^{(1)} \qquad j = 1, 2, 3 \tag{B.21}$$

where $\beta_j^{(1)}$ are three positive real quantities. They are given by

$$\beta_{1,2}^{(1)} = \left[\frac{(2s_{12}'^{(1)} + s_{66}'^{(1)}) \mp \sqrt{(2s_{12}'^{(1)} + s_{66}'^{(1)})^2 - 4s_{11}'^{(1)} s_{22}'^{(1)}}}{2s_{11}'^{(1)}} \right]^{1/2} \tag{B.22}$$

$$\beta_3^{(1)} = \sqrt{\frac{s_{44}'^{(1)}}{s_{55}'^{(1)}}} \,. \tag{B.23}$$

For the upper material $k = 1$, the matrix $\mathbf{A}_1$ in Eq. (B.1) is given by

$$\mathbf{A}_1 = - \begin{bmatrix} k_1^{(1)} \left(s_{11}'^{(1)} \beta_1^{(1)2} - s_{12}'^{(1)} \right) & k_2^{(1)} \left(s_{11}'^{(1)} \beta_2^{(1)2} - s_{12}'^{(1)} \right) & 0 \\ \dfrac{ik_1^{(1)}}{\beta_1^{(1)}} \left(s_{22}'^{(1)} - s_{12}'^{(1)} \beta_1^{(1)2} \right) & \dfrac{ik_2^{(1)}}{\beta_2^{(1)}} \left(s_{22}'^{(1)} - s_{12}'^{(1)} \beta_2^{(1)2} \right) & 0 \\ 0 & 0 & -\dfrac{ik_3^{(1)} s_{44}'^{(1)}}{\beta_3^{(1)}} \end{bmatrix}, \tag{B.24}$$

where $k_j^{(1)}$, $j = 1, 2, 3$, are normalization factors for the upper material which are not necessary in the calculations.

The matrix $\mathbf{B}_1$ from Eq. (B.11) is given by

$$\mathbf{B}_1 = \begin{bmatrix} -ik_1^{(1)} \beta_1^{(1)} & -ik_2^{(1)} \beta_2^{(1)} & 0 \\ k_1^{(1)} & k_2^{(1)} & 0 \\ 0 & 0 & -k_3^{(1)} \end{bmatrix}; \tag{B.25}$$

whereas, its inverse from Eq. (B.12) is given by

$$\mathbf{B}_1^{-1} = \frac{1}{\beta_2^{(1)} - \beta_1^{(1)}} \begin{bmatrix} -\dfrac{i}{k_1^{(1)}} & \dfrac{\beta_2^{(1)}}{k_1^{(1)}} & 0 \\ \dfrac{i}{k_2^{(1)}} & -\dfrac{\beta_1^{(1)}}{k_2^{(1)}} & 0 \\ 0 & 0 & -\dfrac{\beta_2^{(1)} - \beta_1^{(1)}}{k_3^{(1)}} \end{bmatrix}. \tag{B.26}$$

For the lower material, the axial direction coincides with the x_3-direction. The mechanical properties E_A, E_T, G_A, G_T, ν_A and ν_T are taken to be the same as for the

upper material; but they are in different coordinate directions. It turns out that this material is mathematically degenerate. It has three identical complex eigenvalues $p_j^{(2)} = i$ where the subscript $j = 1, 2, 3$, so that

$$\beta_1^{(2)} = \beta_2^{(2)} = \beta_3^{(2)} = 1 \, . \tag{B.27}$$

To determine the stress and displacement fields, matrices alternative to $\mathbf{A}_2$ and $\mathbf{B}_2$ are required; these are $\mathbf{A}_2'$ and $\mathbf{B}_2'$. Since

$$\mathbf{A}\mathbf{B}^{-1} = \mathbf{A}'\mathbf{B}'^{-1} \, , \tag{B.28}$$

it is possible to calculate ε with the aid of Eq. (5.6). On the other hand, one may determine $\mathbf{A}_2\mathbf{B}_2^{-1}$ without calculating the individual matrices (see [5], p. 173).

Nonetheless, the primed matrices are presented. To obtain them, an orthogonalization procedure was employed; for details see [5], pp. 489–492 and [6]. They are found to be

$$\mathbf{A}_2' = \begin{bmatrix} k_1^{(2)}\left(s_{11}'^{(2)} - s_{12}'^{(2)}\right) & -ik_1^{(2)}\kappa\left(s_{11}'^{(2)} - s_{12}'^{(2)}\right) & 0 \\ ik_1^{(2)}\left(s_{11}'^{(2)} - s_{12}'^{(2)}\right) & -k_1^{(2)}\kappa\left(s_{11}'^{(2)} - s_{12}'^{(2)}\right) & 0 \\ 0 & 0 & ik_3^{(2)}s_{44}'^{(2)} \end{bmatrix} , \tag{B.29}$$

$$\mathbf{B}_2' = \begin{bmatrix} ik_1^{(2)} & \frac{1}{2}k_1^{(2)} & 0 \\ -k_1^{(2)} & -\frac{1}{2}ik_1^{(2)} & 0 \\ 0 & 0 & -k_3^{(2)} \end{bmatrix} , \tag{B.30}$$

and

$$\mathbf{B}_2'^{-1} = \begin{bmatrix} \dfrac{-i}{2k_1^{(2)}} & \dfrac{-1}{2k_1^{(2)}} & 0 \\ \dfrac{1}{k_1^{(2)}} & \dfrac{i}{k_1^{(2)}} & 0 \\ 0 & 0 & \dfrac{-1}{k_3^{(2)}} \end{bmatrix} . \tag{B.31}$$

The reduced compliance components are given as

$$\begin{aligned} s_{11}'^{(2)} &= s_{22}'^{(2)} = \frac{1}{E_T}\left(1 - \nu_A^2\frac{E_T}{E_A}\right) \\ s_{12}'^{(2)} &= -\frac{1}{E_T}\left(\nu_T + \nu_A^2\frac{E_T}{E_A}\right) \\ s_{44}'^{(2)} &= s_{55}'^{(2)} = \frac{1}{G_A} \\ s_{66}'^{(2)} &= \frac{2\,(1+\nu_T)}{E_T} \end{aligned} \tag{B.32}$$

and

$$\kappa = \frac{3s_{11}'^{(2)} + s_{12}'^{(2)}}{s_{66}'^{(2)}} \,. \tag{B.33}$$

Recall that $s_{66}'^{(2)} = 2(s_{11}'^{(2)} - s_{12}'^{(2)})$. The normalization factors $k_1^{(2)}$ and $k_3^{(2)}$ are again unnecessary for determining both β in Eq. (5.2) and the stress and displacement fields.

For both materials, using Eqs. (B.24), (B.26), (B.29) and (B.31), as well as (B.27), one may write

$$-\mathbf{A}_k\mathbf{B}_k^{-1} = \begin{bmatrix} is_{11}'^{(k)}\left(\beta_1^{(k)} + \beta_2^{(k)}\right) & -\left(\sqrt{s_{11}'^{(k)}s_{22}'^{(k)}} + s_{12}'^{(k)}\right) & 0 \\ \left(\sqrt{s_{11}'^{(k)}s_{22}'^{(k)}} + s_{12}'^{(k)}\right) & i\sqrt{s_{11}'^{(k)}s_{22}'^{(k)}}\left(\beta_1^{(k)} + \beta_2^{(k)}\right) & 0 \\ 0 & 0 & is_{55}'^{(k)}\beta_3^{(k)} \end{bmatrix} \tag{B.34}$$

where $k = 1, 2$ represents the upper and lower materials, respectively. Equation (B.34) is in a unified form for both materials.

The matrices $\mathbf{A}_2'$, $\mathbf{B}_2'$ and $\mathbf{B}_2'^{-1}$ may be written in a different form as in [1]. But the expression for $\mathbf{A}_k\mathbf{B}_k^{-1}$ in Eq. (B.34) remains the same as in [1] for both the upper and lower materials although in a different form.

From Eq. (B.34), it is possible by means of Eq. (5.6) to obtain

$$\mathbf{L}_k^{-1} = \begin{bmatrix} s_{11}'^{(k)}\left(\beta_1^{(k)} + \beta_2^{(k)}\right) & 0 & 0 \\ 0 & \sqrt{s_{11}'^{(k)}s_{22}'^{(k)}}\left(\beta_1^{(k)} + \beta_2^{(k)}\right) & 0 \\ 0 & 0 & s_{55}'^{(k)}\beta_3^{(k)} \end{bmatrix} . \tag{B.35}$$

Recall that $\mathbf{L}_k^{-1}$ is real. Substituting Eq. (B.35) into (5.4) leads to

$$\mathbf{D} = \begin{bmatrix} \sum_{k=1}^{2} s_{11}'^{(k)}\left(\beta_1^{(k)} + \beta_2^{(k)}\right) & 0 & 0 \\ 0 & \sum_{k=1}^{2}\sqrt{s_{11}'^{(k)}s_{22}'^{(k)}}\left(\beta_1^{(k)} + \beta_2^{(k)}\right) & 0 \\ 0 & 0 & \sum_{k=1}^{2} s_{55}'^{(k)}\beta_3^{(k)} \end{bmatrix} . \tag{B.36}$$

The individual components of $\mathbf{D}$ may be found as

$$D_{11} = \left(1 - \nu_A^2\frac{E_T}{E_A}\right)\left[\frac{\beta_1^{(1)} + \beta_2^{(1)}}{E_A} + \frac{2}{E_T}\right] \tag{B.37}$$

$$D_{22} = \left(1 - \nu_A^2 \frac{E_T}{E_A}\right)\left[\frac{\beta_1^{(1)}\beta_2^{(1)}(\beta_1^{(1)} + \beta_2^{(1)})}{E_A} + \frac{2}{E_T}\right] \tag{B.38}$$

$$D_{33} = \frac{1}{G_A}\left(1 + \beta_3^{(1)}\right) . \tag{B.39}$$

Since the matrix **D** is positive definite [5] (p. 344), it may be shown that

$$D_{11}, D_{22}, D_{33} > 0 . \tag{B.40}$$

These expressions differ in appearance from those in [1]; but are equivalent.

Recalling that $\mathbf{S}_k$ is real, from Eqs. (5.6) and (B.34), it is possible to write

$$\mathbf{S}_k\mathbf{L}_k^{-1} = \begin{bmatrix} 0 & -\left(\sqrt{s_{11}'^{(k)} s_{22}'^{(k)}} + s_{12}'^{(k)}\right) & 0 \\ \left(\sqrt{s_{11}'^{(k)} s_{22}'^{(k)}} + s_{12}'^{(k)}\right) & & 0 \\ 0 & 0 & 0 \end{bmatrix} . \tag{B.41}$$

Substituting Eq. (B.41) into (5.5) leads to

$$\mathbf{W} = \begin{bmatrix} 0 & W_{12} & 0 \\ -W_{12} & 0 & 0 \\ 0 & 0 & 0 \end{bmatrix} \tag{B.42}$$

where

$$W_{12} = (1 + \nu_T)\frac{\nu_A}{E_A} + \frac{1}{E_T}\left(1 - \nu_T - 2\nu_A^2 \frac{E_T}{E_A}\right) - \frac{1}{\beta_1^{(1)}\beta_2^{(1)}}\frac{(1 - \nu_T^2)}{E_T} . \tag{B.43}$$

For the effective mechanical properties of the carbon/epoxy composite considered in [1], $W_{12} > 0$.

From Eqs. (5.2)–(5.5), it is possible to show that

$$\beta = \frac{W_{12}}{\sqrt{D_{11}D_{22}}} \tag{B.44}$$

which is substituted into Eq. (5.1) to obtain the oscillatory parameter ε.

B.2 The $+45°/-45°$ Pair

In this section, the matrices $\mathbf{A}_k$, $\mathbf{B}_k$ and $\mathbf{B}_k^{-1}$ which appear in Eq. (5.6) are presented for the $+45°//-45°$ interface. Each of the materials is transversely isotropic with

respect to the material coordinates. With respect to the delamination front coordinates in Fig. 2.1, the materials are monoclinic with $x_2 = 0$ a symmetry plane [3].

In general, there are thirteen independent compliance components. For these material directions there are only nine independent properties, although the compliance matrix has the form of a monoclinic material. To obtain the compliance components, the matrix in Eq. (B.14) is rotated by 45° about the x_2-axis. To this end, the transpose of the inverse rotation matrix is given by [5] (pp. 54–56)

$$\left(\boldsymbol{K}^{-1}\right)^T = \begin{bmatrix} m^2 & 0 & n^2 & 0 & mn & 0 \\ 0 & 1 & 0 & 0 & 0 & 0 \\ n^2 & 0 & m^2 & 0 & -mn & 0 \\ 0 & 0 & 0 & m & 0 & -n \\ -2mn & 0 & 2mn & 0 & m^2 - n^2 & 0 \\ 0 & 0 & 0 & n & 0 & m \end{bmatrix} \tag{B.45}$$

where T denotes transpose

$$m = \cos\theta \tag{B.46}$$

$$n = \sin\theta\ . \tag{B.47}$$

The compliance matrix may be rotated as

$$\mathbf{s}^* = \left(\boldsymbol{K}^{-1}\right)^T \mathbf{s}\ \boldsymbol{K}^{-1}\ . \tag{B.48}$$

Using Eq. (B.48) with $\theta = 45°$ leads to the compliance coefficients for the upper material as

$$s_{11}^{(1)} = s_{33}^{(1)} = \frac{1-2\nu_A}{4E_A} + \frac{1}{4E_T} + \frac{1}{4G_A} \tag{B.49}$$

$$s_{12}^{(1)} = s_{23}^{(1)} = -\frac{1}{2}\left(\frac{\nu_A}{E_A} + \frac{\nu_T}{E_T}\right) \tag{B.50}$$

$$s_{13}^{(1)} = \frac{1-2\nu_A}{4E_A} + \frac{1}{4E_T} - \frac{1}{4G_A} \tag{B.51}$$

$$s_{15}^{(1)} = s_{35}^{(1)} = -\frac{1}{2}\left(\frac{1}{E_A} - \frac{1}{E_T}\right) \tag{B.52}$$

$$s_{22}^{(1)} = \frac{1}{E_T} \tag{B.53}$$

$$s_{25}^{(1)} = \frac{\nu_A}{E_A} - \frac{\nu_T}{E_T} \tag{B.54}$$

$$s_{44}^{(1)} = s_{66}^{(1)} = \frac{1}{2}\left(\frac{1}{G_T} + \frac{1}{G_A}\right) \tag{B.55}$$

$$s_{46}^{(1)} = \frac{1}{2}\left(\frac{1}{G_T} - \frac{1}{G_A}\right) \tag{B.56}$$

$$s_{55}^{(1)} = \frac{1+2\nu_A}{E_A} + \frac{1}{E_T} \tag{B.57}$$

Of course, the matrix $s_{\alpha\beta}$ is symmetric and $s_{14} = s_{16} = s_{24} = s_{26} = s_{34} = s_{36} = s_{45} = s_{56} = 0$. For the lower material, the compliance matrix in Eq. (B.14) is rotated by $-45°$ about the x_2-axis. The compliance matrix is the same as that of the upper material except that

$$s_{15}^{(2)} = -s_{15}^{(1)} \tag{B.58}$$

$$s_{25}^{(2)} = -s_{25}^{(1)} \tag{B.59}$$

$$s_{35}^{(2)} = -s_{35}^{(1)} \tag{B.60}$$

$$s_{46}^{(2)} = -s_{46}^{(1)} \tag{B.61}$$

Next, the matrices $\mathbf{A}_k$, $\mathbf{B}_k$ and $\mathbf{B}_k^{-1}$ are presented with omission of the normalization factors since they do not appear in the final results. For both materials, using Eq. (B.1)

$$A_{11} = \beta_1^2\left[s_{15}'^2 Q(\beta_1) - s_{11}'\right] + s_{12}' \tag{B.62}$$

$$A_{12} = \beta_2^2\left[s_{15}'^2 Q(\beta_2) - s_{11}'\right] + s_{12}' \tag{B.63}$$

$$A_{13} = \frac{i}{s_{15}' Q(\beta_3)}\left[\frac{s_{12}'}{\beta_3} - \beta_3 s_{11}'\right] + i\beta_3 s_{15}' \tag{B.64}$$

$$A_{21} = i\beta_1\left[s_{12}' - \frac{s_{22}'}{\beta_1^2} - s_{15}' s_{25}' Q(\beta_1)\right] \tag{B.65}$$

$$A_{22} = i\beta_2\left[s_{12}' - \frac{s_{22}'}{\beta_2^2} - s_{15}' s_{25}' Q(\beta_2)\right] \tag{B.66}$$

$$A_{23} = -\frac{s_{12}'}{s_{15}' Q(\beta_3)} + \frac{s_{22}'}{s_{15}' \beta_3^2 Q(\beta_3)} + s_{25}' \tag{B.67}$$

$$A_{31} = -s_{46}' + s_{15}' s_{44}' Q(\beta_1) \tag{B.68}$$

$$A_{32} = -s_{46}' + s_{15}' s_{44}' Q(\beta_2) \tag{B.69}$$

$$A_{33} = \frac{i}{\beta_3}\left[s_{44}' - \frac{s_{46}'}{s_{15}' Q(\beta_3)}\right] \tag{B.70}$$

where the reduced compliance coefficients are found from Eqs. (B.4) and (B.49)–(B.61). The material eigenvalues for both materials are the same and in the form

$$p_1 = i\beta_1\,, \qquad p_2 = i\beta_2\,, \qquad p_3 = i\beta_3 \tag{B.71}$$

where β_j is real and positive. They are found from the sextic equation, Eq. (B.10), where, here,

$$\ell_2 = s'_{55}p^2 + s'_{44} \tag{B.72}$$
$$\ell_3 = s'_{15}p^3 + (s'_{25} + s'_{46})p \tag{B.73}$$
$$\ell_4 = s'_{11}p^4 + (2s'_{12} + s'_{66})p^2 + s'_{22}\ . \tag{B.74}$$

Equation (B.10) is a cubic equation in p^2. In Eqs. (B.62)–(B.70),

$$Q(\beta_j) = \frac{\beta_j^2 - \dfrac{s'_{25} + s'_{46}}{s'_{15}}}{s'_{55}\beta_j^2 - s'_{44}}\ . \tag{B.75}$$

It may be noted that Q has units of inverse compliance.

As a result of the Eqs. (B.58)–(B.61),

$$s'^{(2)}_{15} = -s'^{(1)}_{15} \tag{B.76}$$
$$s'^{(2)}_{25} = -s'^{(1)}_{25} \tag{B.77}$$
$$s'^{(2)}_{46} = -s'^{(1)}_{46}\ . \tag{B.78}$$

Equations (B.76)–(B.78) are obtained by means of Eq. (B.4). The remainder of the reduced compliance coefficients for the upper and lower materials are identical. Moreover, $Q(\beta_j)$ is the same for the upper and lower materials. In addition,

$$A^{(2)}_{13} = -A^{(1)}_{13} \tag{B.79}$$
$$A^{(2)}_{23} = -A^{(1)}_{23} \tag{B.80}$$
$$A^{(2)}_{31} = -A^{(1)}_{31} \tag{B.81}$$
$$A^{(2)}_{32} = -A^{(1)}_{32} \tag{B.82}$$

where the superscripts (1) and (2), denote the upper and lower materials, respectively. Other components of $\mathbf{A}_2$ are identical to those of $\mathbf{A}_1$.

The components of the matrix $\mathbf{B}_k$ for both materials are found from Eq. (B.11) as

$$B_{11} = -i\beta_1 \tag{B.83}$$
$$B_{12} = -i\beta_2 \tag{B.84}$$
$$B_{13} = \frac{1}{s'_{15}Q(\beta_3)} \tag{B.85}$$
$$B_{21} = 1 \tag{B.86}$$
$$B_{22} = 1 \tag{B.87}$$
$$B_{23} = \frac{i}{s'_{15}\beta_3 Q(\beta_3)} \tag{B.88}$$

$$B_{31} = is'_{15}\beta_1 Q(\beta_1) \tag{B.89}$$
$$B_{32} = is'_{15}\beta_2 Q(\beta_2) \tag{B.90}$$
$$B_{33} = -1\ . \tag{B.91}$$

It may be noted that

$$B_{13}^{(2)} = -B_{13}^{(1)} \tag{B.92}$$
$$B_{23}^{(2)} = -B_{23}^{(1)} \tag{B.93}$$
$$B_{31}^{(2)} = -B_{31}^{(1)} \tag{B.94}$$
$$B_{32}^{(2)} = -B_{32}^{(1)}\ . \tag{B.95}$$

The components of the matrix $\mathbf{B}_k^{-1}$ are found from Eq. (B.12) as

$$B_{11}^{-1} = \frac{1}{\Delta_1}\left[\frac{\beta_2 Q(\beta_2)}{\beta_3 Q(\beta_3)} - 1\right] \tag{B.96}$$
$$B_{12}^{-1} = \frac{i\beta_2}{\Delta_1}\left[\frac{Q(\beta_2)}{Q(\beta_3)} - 1\right] \tag{B.97}$$
$$B_{13}^{-1} = \frac{1}{\Delta_1}\left[\frac{\beta_2 - \beta_3}{s'_{15}\beta_3 Q(\beta_3)}\right] \tag{B.98}$$
$$B_{21}^{-1} = \frac{1}{\Delta_1}\left[1 - \frac{\beta_1 Q(\beta_1)}{\beta_3 Q(\beta_3)}\right] \tag{B.99}$$
$$B_{22}^{-1} = \frac{i\beta_1}{\Delta_1}\left[1 - \frac{Q(\beta_1)}{Q(\beta_3)}\right] \tag{B.100}$$
$$B_{23}^{-1} = \frac{1}{\Delta_1}\left[\frac{\beta_3 - \beta_1}{s'_{15}\beta_3 Q(\beta_3)}\right] \tag{B.101}$$
$$B_{31}^{-1} = \frac{is'_{15}}{\Delta_1}\left[\beta_2 Q(\beta_2) - \beta_1 Q(\beta_1)\right] \tag{B.102}$$
$$B_{32}^{-1} = \frac{s'_{15}\beta_1\beta_2}{\Delta_1}\left[Q(\beta_1) - Q(\beta_2)\right] \tag{B.103}$$
$$B_{33}^{-1} = \frac{i}{\Delta_1}\left(\beta_2 - \beta_1\right) \tag{B.104}$$

where

$$B_{13}^{(2)-1} = -B_{13}^{(2)-1} \tag{B.105}$$
$$B_{23}^{(2)-1} = -B_{23}^{(2)-1} \tag{B.106}$$
$$B_{31}^{(2)-1} = -B_{31}^{(2)-1} \tag{B.107}$$
$$B_{32}^{(2)-1} = -B_{32}^{(2)-1} \tag{B.108}$$

and

$$\Delta_1 = i\big(\beta_1 - \beta_2\big) + \frac{i\beta_1\beta_2\big[Q(\beta_1) - Q(\beta_2)\big] - i\beta_3\big[\beta_1 Q(\beta_1) - \beta_2 Q(\beta_2)\big]}{\beta_3 Q(\beta_3)}\,. \tag{B.109}$$

For the upper and lower materials, the 3×3 matrices $-\mathbf{A}_k\mathbf{B}_k^{-1}$ may be found from the expressions in Eqs. (B.62)–(B.70), (B.79)–(B.82), and (B.96)–(B.108). By means of Eq. (5.6), it is possible to determine $\mathbf{S}_k\mathbf{L}_k^{-1}$ and $\mathbf{L}_k^{-1}$. From Eqs. (5.4) and (5.5), the two matrices $\mathbf{D}$ and $\mathbf{W}$ are found. The matrix $\mathbf{D}$ is given by

$$\mathbf{D} = \begin{bmatrix} D_{11} & 0 & 0 \\ 0 & D_{22} & 0 \\ 0 & 0 & D_{33} \end{bmatrix} \tag{B.110}$$

where

$$\begin{aligned} D_{11} = \frac{2s'_{11}}{\Delta}\Bigg\{&\beta_1 + \beta_2 + \frac{\beta_1\beta_2}{\beta_3(\beta_1+\beta_2)}\left[\frac{\beta_2 Q(\beta_1) - \beta_1 Q(\beta_2)}{Q(\beta_3)}\right] \\ &- \frac{\beta_3}{\beta_1 - \beta_2}\left[\frac{\beta_1 Q(\beta_1) - \beta_2 Q(\beta_2)}{Q(\beta_3)}\right]\Bigg\} \\ &+ \frac{2s'_{15}}{\Delta}\Bigg\{\frac{\beta_2^2 Q(\beta_2) - \beta_1^2 Q(\beta_1)}{\beta_1 - \beta_2} + \frac{\beta_1\beta_2}{\beta_3}\frac{Q(\beta_1)Q(\beta_2)}{Q(\beta_3)} \\ &+ \frac{\beta_3}{\beta_1 - \beta_2}\big[\beta_1 Q(\beta_1) - \beta_2 Q(\beta_2)\big]\Bigg\} \end{aligned} \tag{B.111}$$

$$\begin{aligned} D_{22} = \frac{2s'_{22}}{\Delta}\Bigg\{&\frac{\beta_1+\beta_2}{\beta_1\beta_2} + \frac{\beta_1\beta_2}{\beta_3^2(\beta_1-\beta_2)}\left[\frac{Q(\beta_1) - Q(\beta_2)}{Q(\beta_3)}\right] \\ &- \frac{1}{\beta_1\beta_2(\beta_1-\beta_2)}\left[\frac{\beta_1^2 Q(\beta_1) - \beta_2^2 Q(\beta_2)}{Q(\beta_3)}\right]\Bigg\} \end{aligned} \tag{B.112}$$

$$\begin{aligned} D_{33} = \frac{2s'_{44}}{\Delta}\Bigg\{&\frac{1}{\beta_3(\beta_1-\beta_2)}\left[\frac{\beta_2 Q(\beta_1) - \beta_1 Q(\beta_2)}{Q(\beta_3)}\right] \\ &- \frac{1}{\beta_1 - \beta_2}\left[\frac{Q(\beta_1) - Q(\beta_2)}{Q(\beta_3)}\right] + \frac{1}{\beta_3}\Bigg\} \end{aligned} \tag{B.113}$$

and

$$\begin{aligned} \Delta = 1 + \frac{1}{\beta_3(\beta_1-\beta_2)Q(\beta_3)}\Big\{&\beta_1\beta_2\big[Q(\beta_1) - Q(\beta_2)\big] \\ &-\beta_3\big[\beta_1 Q(\beta_1) - \beta_2 Q(\beta_2)\big]\Big\}\,. \end{aligned} \tag{B.114}$$

The matrix **W** is given by

$$\mathbf{W} = \begin{bmatrix} 0 & 0 & 0 \\ 0 & 0 & W_{23} \\ 0 & -W_{23} & 0 \end{bmatrix} \tag{B.115}$$

where

$$W_{23} = 2s_{25}'^{(1)} - \frac{2s_{22}'}{s_{15}'^{(1)}\Delta}\frac{1}{\beta_3 Q(\beta_3)}\left\{\frac{\beta_1+\beta_2-\beta_3}{\beta_1\beta_2} - \frac{1}{\beta_3}\right\}. \tag{B.116}$$

From Eqs. (5.2)–(5.5), it is possible to show that

$$\beta = \frac{|W_{23}|}{\sqrt{D_{22}D_{33}}} \tag{B.117}$$

which is substituted into Eq. (5.1) to obtain the oscillatory parameter ε.

B.3 The $+30°/-60°$ Pair and the $-30°/+60°$ Pair

In this section, the matrices $\mathbf{A}_k$, $\mathbf{B}_k$ and $\mathbf{B}_k^{-1}$ which appear in Eq. (5.6) are presented for the $+30°//-60°$ and $-30°//+60°$ interfaces. As with the $+45°//-45°$ interface, each of the materials described in this section is transversely isotropic with respect to the material coordinates with the compliance matrix given in Eq. (B.14). With respect to the delamination front coordinates given in Fig. 2.1, the materials are monoclinic with $x_2 = 0$ a symmetry plane. For each material, there are 13 independent compliance coefficients. For the material with fibers in the $+30°$-direction, the matrix in Eq. (B.14) is rotated by $+30°$ clockwise about the x_2-axis. Using $\theta = 30°$ in Eqs. (B.45) and (B.48) leads to

$$s_{11}^{(1)} = \frac{1}{16}\left[\frac{3(3-2\nu_A)}{E_A} + \frac{1}{E_T} + \frac{3}{G_A}\right] \tag{B.118}$$

$$s_{12}^{(1)} = -\frac{1}{4}\left(\frac{3\nu_A}{E_A} + \frac{\nu_T}{E_T}\right) \tag{B.119}$$

$$s_{13}^{(1)} = \frac{1}{16}\left[\frac{3-10\nu_A}{E_A} + \frac{3}{E_T} - \frac{3}{G_A}\right] \tag{B.120}$$

$$s_{15}^{(1)} = -\frac{\sqrt{3}}{8}\left[\frac{3+2\nu_A}{E_A} - \frac{1}{E_T} - \frac{1}{G_A}\right] \tag{B.121}$$

$$s_{22}^{(1)} = \frac{1}{E_T} \tag{B.122}$$

$$s_{23}^{(1)} = -\frac{1}{4}\left(\frac{\nu_A}{E_A} + \frac{3\nu_T}{E_T}\right) \tag{B.123}$$

$$s_{25}^{(1)} = \frac{\sqrt{3}}{2}\left(\frac{\nu_A}{E_A} - \frac{\nu_T}{E_T}\right) \tag{B.124}$$

$$s_{33}^{(1)} = \frac{1}{16}\left[\frac{1-6\nu_A}{E_A} + 3\left(\frac{3}{E_T} + \frac{1}{G_A}\right)\right] \tag{B.125}$$

$$s_{35}^{(1)} = -\frac{\sqrt{3}}{8}\left[\frac{1-2\nu_A}{E_A} - \frac{3}{E_T} + \frac{1}{G_A}\right] \tag{B.126}$$

$$s_{44}^{(1)} = \frac{1}{4}\left(\frac{3}{G_T} + \frac{1}{G_A}\right) \tag{B.127}$$

$$s_{46}^{(1)} = \frac{\sqrt{3}}{4}\left(\frac{1}{G_T} - \frac{1}{G_A}\right) \tag{B.128}$$

$$s_{55}^{(1)} = \frac{3}{4}\left[\frac{1+2\nu_A}{E_A} + \frac{1}{E_T} + \frac{1}{3G_A}\right] \tag{B.129}$$

$$s_{66}^{(1)} = \frac{1}{4}\left(\frac{1}{G_T} + \frac{3}{G_A}\right) \tag{B.130}$$

Of course, the matrix $s_{\alpha\beta}^{(1)}$ is symmetric and $s_{14}^{(1)} = s_{16}^{(1)} = s_{24}^{(1)} = s_{26}^{(1)} = s_{34}^{(1)} = s_{36}^{(1)} = s_{45}^{(1)} = s_{56}^{(1)} = 0$.

For the lower material with fibers in the $-60°$-direction, the compliance matrix in Eq. (B.14) requires rotation by $-60°$ with respect to the x_1-axis. Making use of Eqs. (B.45) and (B.48), the compliance matrices were obtained for $\theta = -60°$, $\theta = -30°$ and $\theta = 60°$.

In order to determine the eigenvalues of the material, Eq. (B.10) is solved with $\ell_2(p)$, $\ell_3(p)$ and $\ell_4(p)$ given in Eqs. (B.72), (B.73) and (B.74), respectively. The reduced compliance coefficients may be found by means of Eq. (B.4). For the carbon fiber reinforced material AS4-3502 used in [4], the eigenvalues take the form given in Eq. (B.71) for all materials in this section. In fact, the eigenvalues are the same for the material with fibers in either the $+\theta$ or $-\theta$ directions. The mechanical properties of this material are given in Table 7.1.

The complex 3×3 matrix $\boldsymbol{A}$ is given in Eq. (B.1) where Eqs. (B.2)–(B.3) have been replaced by

$$\xi_\alpha(p_\beta) = p_\beta^2 s'_{\alpha 1} + s'_{\alpha 2} + \lambda_\beta p_\beta s'_{\alpha 5} \tag{B.131}$$

$$\xi_4(p_\beta) = -p_\beta s'_{46} - \lambda_\beta s'_{44} \tag{B.132}$$

$$\eta_\alpha(p_3) = \lambda_3(p_3^2 s'_{\alpha 1} + s'_{\alpha 2}) + p_3 s'_{\alpha 5} \tag{B.133}$$

$$\eta_4(p_3) = -\lambda_3 p_3 s'_{46} - s'_{44} \tag{B.134}$$

for $\alpha, \beta = 1, 2$ and the parameters λ_j ($j = 1, 2, 3$) are given in Eqs. (B.5) and (B.6). The functions ℓ_i, $i = 2, 3, 4$, are given in Eqs. (B.72)–(B.74). The normalization factors k_1, k_2 and k_3 are not required in the calculations. For each fiber direction, the matrix $\boldsymbol{A}$ in Eq. (B.1) is obtained by substitution of the various parameters found for

that material direction. The matrix $\boldsymbol{B}$ for each fiber direction is given in Eq. (B.11) and its inverse is given in Eq. (B.12).

For the upper and lower materials of each interface, the 3×3 matrices $-\mathbf{A}_k\mathbf{B}_k^{-1}$ may be found by multiplying the two matrices Eqs. (B.1) and (B.12). By means of Eq. (5.6), it is possible to determine $\mathbf{S}_k\mathbf{L}_k^{-1}$ and $\mathbf{L}_k^{-1}$. From Eqs. (5.4) and (5.5), the two matrices $\mathbf{D}$ and $\mathbf{W}$ are found. The matrix $\mathbf{D}$ is given by

$$\mathbf{D} = \begin{bmatrix} D_{11} & 0 & D_{13} \\ 0 & D_{22} & 0 \\ D_{13} & 0 & D_{33} \end{bmatrix} \tag{B.135}$$

and its inverse is

$$\boldsymbol{D}^{-1} = \frac{1}{Q}\begin{bmatrix} D_{33} & 0 & -D_{13} \\ 0 & \dfrac{Q}{D_{22}} & 0 \\ -D_{13} & 0 & D_{11} \end{bmatrix} \tag{B.136}$$

where

$$Q = D_{11}D_{33} - D_{13}^2 \, . \tag{B.137}$$

Since $\boldsymbol{D}^{-1}$ is positive definite, $Q > 0$. The matrix $\boldsymbol{W}$ is given by

$$\boldsymbol{W} = \begin{bmatrix} 0 & W_{12} & 0 \\ -W_{12} & 0 & W_{23} \\ 0 & -W_{23} & 0 \end{bmatrix} . \tag{B.138}$$

The matrix $\breve{\mathbf{S}}$ is obtained by means of Eq. (5.3), and given as

$$\breve{\mathbf{S}} = \frac{1}{Q}\begin{bmatrix} 0 & D_{33}W_{12} + D_{13}W_{23} & 0 \\ -\dfrac{QW_{12}}{D_{22}} & 0 & \dfrac{QW_{23}}{D_{22}} \\ 0 & -(D_{13}W_{12} + D_{11}W_{23}) & 0 \end{bmatrix} . \tag{B.139}$$

The parameter β may be calculated by substituting Eq. (B.139) into (5.2) to obtain

$$\beta = \left\{ \frac{D_{11}W_{23}^2 + 2D_{13}W_{12}W_{23} + D_{33}W_{12}^2}{D_{22}\left(D_{11}D_{33} - D_{13}^2\right)} \right\}^{\frac{1}{2}} . \tag{B.140}$$

In Eq. (B.140), it may be seen that the quantity within the curly brackets is real [5] (pp. 179–180, 282–283, 344). A real value for β is obtained when the numerator and

denominator are of the same sign. Since β is real and the denominator is positive, the numerator must be positive as well, namely

$$D_{11}W_{23}^2 + 2D_{13}W_{12}W_{23} + D_{33}W_{12}^2 > 0\,. \tag{B.141}$$

The value of β is substituted into Eq. (5.1) to obtain the oscillatory parameter ε.

B.4 Multi-directional Woven Material

In this section, a multi-directional (MD) composite consisting of plies of a plain, balanced weave are considered. The upper ply has fibers in the 0° and 90°-directions. The lower ply is obtained by rotating the ply about the x_2-axis by 45° so that it has fibers in the +45° and −45°-directions. For the upper material with $k = 1$ (see Fig. 2.1), the compliance matrix is given by

$$\boldsymbol{s}^{(1)} = \begin{bmatrix} \frac{1}{E_{11}} & \frac{-\nu_{12}}{E_{11}} & \frac{-\nu_{13}}{E_{11}} & 0 & 0 & 0 \\ & \frac{1}{E_{22}} & \frac{-\nu_{12}}{E_{11}} & 0 & 0 & 0 \\ & & \frac{1}{E_{11}} & 0 & 0 & 0 \\ & & & \frac{1}{G_{12}} & 0 & 0 \\ & & \text{sym} & & \frac{1}{G_{13}} & 0 \\ & & & & & \frac{1}{G_{12}} \end{bmatrix}. \tag{B.142}$$

The compliance matrix for the lower material may be found by rotating that in Eq. (B.142) by 45° about the x_2-axis using Eqs. (B.45) and (B.48). The components are given by

$$s_{11}^{(2)} = s_{33}^{(2)} = \frac{1-\nu_{13}}{2E_{11}} + \frac{1}{4G_{13}} \tag{B.143}$$

$$s_{12}^{(2)} = s_{23}^{(2)} = -\frac{\nu_{12}}{E_{11}} \tag{B.144}$$

$$s_{13}^{(2)} = \frac{1-\nu_{13}}{2E_{11}} - \frac{1}{4G_{13}} \tag{B.145}$$

$$s_{22}^{(2)} = \frac{1}{E_{22}} \tag{B.146}$$

$$s_{44}^{(2)} = s_{66}^{(2)} = \frac{1}{G_{12}} \tag{B.147}$$

$$s_{55}^{(2)} = \frac{2(1+\nu_{13})}{E_{11}} \tag{B.148}$$

Of course, the matrix $s_{\alpha\beta}^{(2)}$ is symmetric with the same zero entries as in Eq. (B.142). It may be observed that this material is also tetragonal.

The material eigenvalues may be found from Eq. (B.10) where

$$\ell_2 = s'_{55}p^2 + s'_{44} \tag{B.149}$$

$$\ell_3 = 0 \tag{B.150}$$

$$\ell_4 = s'_{11}p^4 + (2s'_{12} + s'_{66})p^2 + s'_{22} \tag{B.151}$$

and $s'_{\alpha\beta}$ are the reduced compliance coefficients in Eq. (B.4) for each material. So that p_j are given in Eq. (B.21) for the specific material studied in [2] and described in Sects. 5.4 and 7.2. The expressions for β_j for both upper and lower materials take the form given in Eqs. (B.22) and (B.23).

Matrices $\mathbf{A}_k$, $\mathbf{B}_k$ and $\mathbf{B}_k^{-1}$ may be found in Eqs. (B.24), (B.25) and (B.26) for both materials. Then $\mathbf{A}_k\mathbf{B}_k^{-1}$ is given in Eq. (B.34). The components of the matrices $\mathbf{D}$ and $\mathbf{W}$ may be obtained from Eqs. (B.36) and (B.42), respectively. For the material studied here, $W_{12} > 0$. The expression for β is given in Eq. (B.44) and the oscillatory parameter ε may be calculated from Eq. (5.1).

References

1. Banks-Sills L, Boniface V (2000) Fracture mechanics for an interface crack between a special pair of transversely isotropic materials. In: Chuang T-J, Rudnicki, JW (eds) Multiscale deformation and fracture in materials and structures–the James R. Rice 60th anniversary volume. Kluwer Academic Publishers, The Netherlands, pp 183–204
2. Banks-Sills L, Ishbir C, Fourman V, Rogel L, Eliasi R (2013) Interface fracture toughness of a multi-directional woven composite. Int J Fract 182:187–207
3. Freed Y, Banks-Sills, L (2005) A through interface crack between a ±45° transversely isotropic pair of materials. Int J Fract 133:1–41
4. Rogel L, Banks-Sills L (2010) A through interface crack between a transversely isotropic pair of materials (+30°/ − 60°, −30°/ + 60°). Eng Fract Mech 77:3261–3291
5. Ting TCT (1996) Anisotropic elasticity–theory and applications. Oxford University Press, Oxford
6. Ting TCT, Hwu C (1988) Sextic formalism in anisotropic elasticity for almost non-semisimple matrix **N**. Int J Solids Struct 24:65–76

Appendix C
Stress and Displacement Functions for the First Term of the Asymptotic Expansion of an Interface Crack Between Two Anisotropic Materials

The stress and displacement functions for the first term of the asymptotic expansion of an interface crack between two linear elastic, homogeneous and anisotropic materials are presented here. For the upper material ($k = 1$), it may be shown that

$$\mathbf{u}^{(1)} = \frac{i}{2}\left\{-e^{-i\delta\pi}\mathbf{A}_1\left\langle z_*^{(1)\,\delta+1}\right\rangle\mathbf{B}_1^{-1} + e^{i\delta\pi}\overline{\mathbf{A}}_1\left\langle \overline{z}_*^{(1)\,\delta+1}\right\rangle\overline{\mathbf{B}}_1^{-1}\right\}\mathbf{g} \tag{C.1}$$

$$\phi^{(1)} = \frac{i}{2}\left\{-e^{-i\delta\pi}\mathbf{B}_1\left\langle z_*^{(1)\,\delta+1}\right\rangle\mathbf{B}_1^{-1} + e^{i\delta\pi}\overline{\mathbf{B}}_1\left\langle \overline{z}_*^{(1)\,\delta+1}\right\rangle\overline{\mathbf{B}}_1^{-1}\right\}\mathbf{g} \tag{C.2}$$

where δ is an unknown eigenvalue and related to the power of the singularities and $\mathbf{A}_1$, $\mathbf{B}_1$ and $\mathbf{B}_1^{-1}$ are given in Eqs. (B.1), (B.11) and (B.12) for a general anisotropic material. The diagonal matrix in Eqs. (C.1) and (C.2) is given by

$$\left\langle z_*^{(1)}\right\rangle = \text{diag}\left[z_1^{(1)}, z_2^{(1)}, z_3^{(1)}\right], \tag{C.3}$$

where

$$z_j^{(1)} = x_1 + p_j^{(1)}x_2 \tag{C.4}$$

and $p_j^{(1)}$ are the eigenvalues of the compatibility equations of the upper material. The bar over a quantity represents its complex conjugate and $\mathbf{g}$ is an arbitrary, complex valued unknown vector.

For the lower material ($k = 2$), it may be shown that

$$\mathbf{u}^{(2)} = \frac{i}{2}\left\{e^{i\delta\pi}\mathbf{A}_2\left\langle z_*^{(2)\,\delta+1}\right\rangle\mathbf{B}_2^{-1} - e^{-i\delta\pi}\overline{\mathbf{A}}_2\left\langle \overline{z}_*^{(2)\,\delta+1}\right\rangle\overline{\mathbf{B}}_2^{-1}\right\}\mathbf{h} \tag{C.5}$$

$$\phi^{(2)} = \frac{i}{2}\left\{e^{i\delta\pi}\mathbf{B}_2\left\langle z_*^{(2)\,\delta+1}\right\rangle\mathbf{B}_2^{-1} - e^{-i\delta\pi}\overline{\mathbf{B}}_2\left\langle \overline{z}_*^{(2)\,\delta+1}\right\rangle\overline{\mathbf{B}}_2^{-1}\right\}\mathbf{h} \tag{C.6}$$

where $\mathbf{A}_2$, $\mathbf{B}_2$ and $\mathbf{B}_2^{-1}$ are given in Eqs. (B.1), (B.11) and (B.12) for a general anisotropic material and $\mathbf{h}$ is an arbitrary, complex valued unknown vector. The

L. Banks-Sills, *Interface Fracture and Delaminations in Composite Materials*,
SpringerBriefs in Structural Mechanics, DOI 10.1007/978-3-319-60327-8

expressions in Eqs. (C.1), (C.2), (C.5), and (C.6) were obtained from expressions given in [3] (p. 341) and by enforcing zero traction on the crack faces.

The two materials are assumed to be perfectly bonded along the interface, so that for $\theta = 0$ (see Fig. 2.1) traction and displacement continuity are required. Hence,

$$\boldsymbol{\phi}^{(1)}\big|_{\theta=0} = \boldsymbol{\phi}^{(2)}\big|_{\theta=0} \tag{C.7}$$

$$\mathbf{u}^{(1)}\big|_{\theta=0} = \mathbf{u}^{(2)}\big|_{\theta=0} \ . \tag{C.8}$$

The relation in Eq. (C.7) is obtained using Eq. (5.8). Continuity of traction leads to the relation

$$\mathbf{g} = \mathbf{h} \equiv \mathbf{d} \ . \tag{C.9}$$

The relations in Eqs. (C.1), (C.2), (C.5), and (C.6) are rewritten with $\mathbf{d}$ replacing $\mathbf{g}$ and $\mathbf{h}$.

Continuity of displacements along the interface provides an equation for determining the singularity δ given by

$$\left\{\check{\mathbf{S}} - \cot \delta\pi \mathbf{I}\right\} \mathbf{d} = 0 \ . \tag{C.10}$$

In Eq. (C.10), $\mathbf{I}$ is the 3×3 unit matrix and $\check{\mathbf{S}}$ is given in Eq. (5.3). Equation (C.10) is an eigenvalue equation for $\check{\mathbf{S}}$, where $\cot \delta\pi$ and $\mathbf{d}$ are the eigenvalues and eigenvectors, respectively. A non-trivial solution is obtained when

$$\det\left[\check{\mathbf{S}} - \cot \delta\pi \mathbf{I}\right] = 0 \tag{C.11}$$

which yields three eigenvalues of the form $\cot \delta\pi = 0$ and $\cot \delta\pi = \pm i\beta$, where β is given in Eq. (5.2). Extracting δ from the eigenvalues yields

$$\delta_{1,2} = -\tfrac{1}{2} \pm i\varepsilon, \ \delta_3 = -\tfrac{1}{2} \tag{C.12}$$

where ε is real, depends upon mechanical properties of the two materials and is given in Eq. (5.1).

The asymptotic stress and displacement fields are obtained by substituting the values of δ obtained in Eq. (C.12) into (C.1), (C.2), (C.5), and (C.6) and superposing the three solutions. For the upper material and the oscillatory, square-root singularity

$$\mathbf{u}^{(1)} = \Re\left[e^{\varepsilon\pi}\mathbf{A}_1 \left\langle z_*^{(1)\ 1/2+i\varepsilon}\right\rangle \mathbf{B}_1^{-1}\mathbf{d} + e^{-\varepsilon\pi}\mathbf{A}_1 \left\langle z_*^{(1)\ 1/2-i\varepsilon}\right\rangle \mathbf{B}_1^{-1}\bar{\mathbf{d}}\right] \tag{C.13}$$

$$\boldsymbol{\phi}^{(1)} = \Re\left[e^{\varepsilon\pi}\mathbf{B}_1 \left\langle z_*^{(1)\ 1/2+i\varepsilon}\right\rangle \mathbf{B}_1^{-1}\mathbf{d} + e^{-\varepsilon\pi}\mathbf{B}_1 \left\langle z_*^{(1)\ 1/2-i\varepsilon}\right\rangle \mathbf{B}_1^{-1}\bar{\mathbf{d}}\right] \ . \tag{C.14}$$

For the lower material,

$$\mathbf{u}^{(2)} = \Re\left[e^{-\varepsilon\pi}\mathbf{A}_2\left\langle z_*^{(2)\ 1/2+i\varepsilon}\right\rangle\mathbf{B}_2^{-1}\mathbf{d} + e^{\varepsilon\pi}\mathbf{A}_2\left\langle z_*^{(2)\ 1/2-i\varepsilon}\right\rangle\mathbf{B}_2^{-1}\bar{\mathbf{d}}\right] \tag{C.15}$$

$$\phi^{(2)} = \Re\left[e^{-\varepsilon\pi}\mathbf{B}_2\left\langle z_*^{(2)\ 1/2+i\varepsilon}\right\rangle\mathbf{B}_2^{-1}\mathbf{d} + e^{\varepsilon\pi}\mathbf{B}_2\left\langle z_*^{(2)\ 1/2-i\varepsilon}\right\rangle\mathbf{B}_2^{-1}\bar{\mathbf{d}}\right] . \tag{C.16}$$

For the square-root singularity and the upper material

$$\mathbf{u}^{(1)} = \Re\left[\mathbf{A}_1\left\langle z_*^{\frac{1}{2}}\right\rangle\mathbf{B}_1^{-1}\right]\mathbf{d}^* \tag{C.17}$$

$$\phi^{(1)} = \Re\left[\mathbf{B}_1\left\langle z_*^{\frac{1}{2}}\right\rangle\mathbf{B}_1^{-1}\right]\mathbf{d}^* ; \tag{C.18}$$

for the lower material,

$$\mathbf{u}^{(2)} = \Re\left[\mathbf{A}_2\left\langle z_*^{\frac{1}{2}}\right\rangle\mathbf{B}_2^{-1}\right]\mathbf{d}^* \tag{C.19}$$

$$\phi^{(2)} = \Re\left[\mathbf{B}_2\left\langle z_*^{\frac{1}{2}}\right\rangle\mathbf{B}_2^{-1}\right]\mathbf{d}^* ; \tag{C.20}$$

where $\mathbf{d}^*$ is an arbitrary, real vector.

In particular, the case when the fibers in the upper material are in the 0°-direction and those in the lower material are in the 90°-direction is considered.

For the upper material, the displacement and the stress function vectors associated with the oscillatory, square-root singularity are given in Eqs. (C.13) and (C.14). The oscillatory parameter ε is given in Eq. (5.1), β in Eq. (B.44), the matrices $\mathbf{A}_1$, $\mathbf{B}_1$ and $\mathbf{B}_1^{-1}$ are given in Eqs. (B.24), (B.25) and (B.26), respectively, and $\mathbf{d}$ is a 3×1 complex vector to be found. The lower material is mathematically degenerate. For this material, a special procedure is required [1, 3] which yields

$$\mathbf{u}^{(2)} = \Re\left[e^{-\varepsilon\pi}\mathbf{A}_2'\mathbf{F}(z^{(2)})\mathbf{B}_2'^{-1}\mathbf{d} + e^{\epsilon\pi}\mathbf{A}_2'\bar{\mathbf{F}}(z^{(2)})\mathbf{B}_2'^{-1}\bar{\mathbf{d}}\right] \tag{C.21}$$

$$\phi^{(2)} = \Re\left[e^{-\varepsilon\pi}\mathbf{B}_2'\mathbf{F}(z^{(2)})\mathbf{B}_2'^{-1}\mathbf{d} + e^{\varepsilon\pi}\mathbf{B}_2'\bar{\mathbf{F}}(z^{(2)})\mathbf{B}_2'^{-1}\bar{\mathbf{d}}\right] . \tag{C.22}$$

In Eqs. (C.21) and (C.22), the matrix $\mathbf{F}(z)$ is given by

$$\mathbf{F}(z) = \begin{bmatrix} f(z) & x_2 f'(z) & 0 \\ 0 & f(z) & 0 \\ 0 & 0 & f(z) \end{bmatrix} , \tag{C.23}$$

$$f(z) = z^{1/2+i\epsilon} \tag{C.24}$$

and $()'$ represents differentiation with respect to z. For a transversely isotropic material with the axial direction coinciding with the x_3-axis, $p_j = i$; hence,

$$z^{(2)} = z = x_1 + ix_2 . \tag{C.25}$$

For the oscillatory, square-root singular part of the solution, the complex vector $\mathbf{d}$ is determined from Eq. (C.10) and is found to be

$$\mathbf{d}^T = \left[i\sqrt{D_{22}/D_{11}},\, 1,\, 0 \right] d_2 \,. \tag{C.26}$$

The complex vector $\mathbf{d}$ is arbitrary and was written differently in [1] (see Sect. 5.5 for a further discussion). Once chosen, the complex scalar d_2 is determined and presented in Eq. $(5.14)_1$. For the square-root part of the solution, in a similar manner, with the real vector $\mathbf{d}$ denoted as $\mathbf{d}^*$

$$\mathbf{d}^{*T} = [0,\, 0,\, 1]\, d_3 \,. \tag{C.27}$$

The real constant d_3 is presented in Eq. $(5.14)_2$.

For material (1), the upper material, the in-plane stress functions in Eq. (2.1) are found by differentiation of the stress function vector in Eq. (C.14) by the in-plane coordinates x_1 and x_2 and substituted into Eqs. (5.7) and (5.8) to obtain

$$\begin{aligned}
{}_1\Sigma_{11}^{(1)} &= -{}_1c_2^* \sum_{s=1}^{2}\sum_{t=1}^{2} (-1)^s\, {}_1\widetilde{N}_{st}\, {}_1B_s^{-\frac{1}{2}}\, \beta_s^{(1)^2} \left({}_1N_{st}^*\, \widetilde{D} + \beta_s^{*(1)} \right) \\
{}_1\Sigma_{11}^{(2)} &= {}_1c_2^* \sum_{s=1}^{2}\sum_{t=1}^{2} (-1)^{s+t}\, {}_1\widetilde{N}_{st}\, {}_1B_s^{-\frac{1}{2}}\, \beta_s^{(1)^2} \left({}_1n_{st}^*\, \widetilde{D} - {}_1M_{st}^* \beta_s^{*(1)} \right) \\
{}_1\Sigma_{12}^{(1)} &= -{}_1c_2^* \sum_{s=1}^{2}\sum_{t=1}^{2} (-1)^{s+t}\, {}_1\widetilde{N}_{st}\, {}_1B_s^{-\frac{1}{2}}\, \beta_s^{(1)} \left({}_1M_{st}^*\, \widetilde{D} - {}_1n_{st}^* \beta_s^{*(1)} \right) \\
{}_1\Sigma_{12}^{(2)} &= {}_1c_2^* \sum_{s=1}^{2}\sum_{t=1}^{2} (-1)^{s}\, {}_1\widetilde{N}_{st}\, {}_1B_s^{-\frac{1}{2}}\, \beta_s^{(1)} \left(\widetilde{D} + {}_1N_{st}^* \beta_s^{*(1)} \right) \\
{}_1\Sigma_{22}^{(1)} &= {}_1c_2^* \sum_{s=1}^{2}\sum_{t=1}^{2} (-1)^{s}\, {}_1\widetilde{N}_{st}\, {}_1B_s^{-\frac{1}{2}} \left({}_1N_{st}^*\, \widetilde{D} + \beta_s^{*(1)} \right) \\
{}_1\Sigma_{22}^{(2)} &= -{}_1c_2^* \sum_{s=1}^{2}\sum_{t=1}^{2} (-1)^{s+t}\, {}_1\widetilde{N}_{st}\, {}_1B_s^{-\frac{1}{2}} \left({}_1n_{st}^*\, \widetilde{D} - {}_1M_{st}^* \beta_s^{*(1)} \right)
\end{aligned} \tag{C.28}$$

For the lower material, material (2), use is made of Eq. (C.22) to obtain

$$\begin{aligned}
{}_2\Sigma_{11}^{(1)} &= {}_2c_2^* \sum_{t=1}^{2} \widetilde{M}_t \left({}_2M_{1t}^*\, \widetilde{D} - m_t^* \right) - 2{}_2c_2^*\, {}_2n_{12} \left(2{}_2N_{12}\, \widetilde{D} - {}_2N_{11} \right) \\
{}_2\Sigma_{11}^{(2)} &= -{}_2c_2^* \sum_{t=1}^{2} (-1)^t\, \widetilde{M}_t \left(\widetilde{D} - {}_2N_{1t}^* \right) + 2{}_2c_2^*\, {}_2n_{11} \left(2{}_2N_{11}\, \widetilde{D} - {}_2N_{12} \right) \\
{}_2\Sigma_{12}^{(1)} &= {}_2c_2^* \sum_{t=1}^{2} (-1)^t\, \widetilde{M}_t \left(N_{1t}^*\, \widetilde{D} - 1 \right) - 2{}_2c_2^*\, {}_2n_{12}\, {}_2N_{12}\, \widetilde{D} \\
{}_2\Sigma_{12}^{(2)} &= {}_2c_2^* \sum_{t=1}^{2} \widetilde{M}_t \left(m_t^*\, \widetilde{D} - {}_2M_{1t}^* \right) - 2{}_2c_2^*\, {}_2n_{11}\, {}_2N_{11}\, \widetilde{D}
\end{aligned} \tag{C.29}$$

$$
\begin{aligned}
{}_2\Sigma_{22}^{(1)} &= -{}_2c_2^* \sum_{t=1}^{2} \widetilde{M}_t \left({}_2M_{1t}^* \widetilde{D} - m_t^*\right) + 2{}_2c_2^* {}_2N_{11}\, {}_2n_{11} \\
{}_2\Sigma_{22}^{(2)} &= \quad {}_2c_2^* \sum_{t=1}^{2} (-1)^t \widetilde{M}_t \left(\widetilde{D} - {}_2N_{1t}^*\right) - 2{}_2c_2^* {}_2N_{12}\, {}_2n_{12}
\end{aligned}
$$

In Eqs. (C.28) and (C.29),

$$
\widetilde{D} = \sqrt{\frac{D_{22}}{D_{11}}} \tag{C.30}
$$

where D_{11} and D_{22} are elements of the matrix $\mathbf{D}$ given explicitly in Eqs. (B.37) and (B.38) and for $s = 1, 2, 3$,

$$
\begin{aligned}
{}_kB_s &= \cos^2\theta + [\beta_s^{(k)}]^2 \sin^2\theta \qquad {}_kn_{s1} = \cos\left(\frac{{}_k\varphi_s}{2}\right) \\
{}_kn_{s2} &= \sin\left(\frac{{}_k\varphi_s}{2}\right) \qquad {}_k\varphi_s = \arg\left(\cos\theta + i\beta_s^{(k)} \sin\theta\right)
\end{aligned} \tag{C.31}
$$

where $k = 1, 2$ represents the upper and lower materials, respectively. Recall that

$$
\beta_1^{(2)} = \beta_2^{(2)} = \beta_3^{(2)} = 1 \tag{C.32}
$$

and $\beta_s^{(1)}$ are given in Eqs. (B.22) and (B.23). For $s, t = 1, 2$,

$$
{}_kc_s^* = \frac{2\left[\frac{1}{2}(1+4\varepsilon^2)\right]^{s-1}}{[\beta_1^{(k)} + (-1)^k\beta_2^{(k)}](1+4\varepsilon^2)\cosh\pi\varepsilon}, \qquad {}_km_s = \frac{\varepsilon}{2}\ln\left({}_kB_s\right)
$$

$$
{}_kN_{s1} = \cosh\varepsilon[\pi + (-1)^k{}_k\varphi_s] \qquad {}_kN_{s2} = \sinh\varepsilon[\pi + (-1)^k{}_k\varphi_s]
$$

$$
{}_kM_{s1} = {}_kM_{s3} + 2\varepsilon\, {}_kM_{s4} \qquad {}_kM_{s2} = {}_kM_{s4} - 2\varepsilon\, {}_kM_{s3} \qquad {}_kM_{s3} = \cos({}_km_s)
$$

$$
{}_kM_{s4} = \sin({}_km_s) \qquad {}_kM_{st}^* = {}_kM_{s1}\, {}_kM_{s2}\, {}_kM_{st}^{-2}
$$

$$
m_{11} = \cos\left(\frac{3\theta}{2}\right) \qquad m_{12} = \sin\left(\frac{3\theta}{2}\right) \qquad m_t^* = m_{11}m_{12}m_{1t}^{-2}
$$

$$
\beta_s^{*(k)} = \beta_1^{(k)}\beta_2^{(k)}\beta_s^{(k)^{-1}} \qquad {}_kN_{st}^* = {}_kN_{s1}\, {}_kN_{s2}\, {}_kN_{st}^{-2} \qquad {}_kn_{st}^* = {}_kn_{s1}\, {}_kn_{s2}\, {}_kn_{st}^{-2}
$$

$$
{}_k\widetilde{N}_{st} = {}_kn_{st}\, {}_kN_{st}\, {}_kM_{st}\, {}_kB_s^{\frac{1}{4}} \qquad \widetilde{M}_t = m_{1t}\, {}_2N_{1t}\, {}_2M_{1t} \sin\theta\ .
$$

In addition,

$$
\begin{aligned}
{}_kQ_s &= -s_{12}^{\prime(k)} + [\beta_s^{(k)}]^2 s_{11}^{\prime(k)} \qquad {}_kQ_{s+2} = s_{22}^{\prime(k)} - [\beta_s^{(k)}]^2 s_{12}^{\prime(k)} \\
[10pt]\kappa_1 &= 1 + 2\kappa \qquad \kappa_2 = 1 - 2\kappa \qquad \widetilde{c} = 2{}_2c_2^*\, {}_2Q_1 \sin\theta\ .
\end{aligned} \tag{C.34}
$$

where κ depends upon the mechanical properties and is given in Eq. (B.33). Moreover, the out-of-plane stress functions in Eq. (2.5) may be written as

$$ {}_k\Sigma_{31}^{(III)} = -\beta_3^{(k)}\, {}_kB_3^{-\frac{1}{4}}\, {}_kn_{32} \tag{C.35} $$

$$ {}_k\Sigma_{32}^{(III)} = {}_kB_3^{-\frac{1}{4}}\, {}_kn_{31} \tag{C.36} $$

The stress functions are non-dimensional.

In Eqs. (2.6), the functions ${}_kU_\alpha^{(1)}(\theta)$ and ${}_kU_\alpha^{(2)}(\theta)$, $(k = 1, 2)$, provide the in-plane displacement components. These functions are obtained from Eqs. (C.13) and (C.21). They depend upon θ and the mechanical properties of both materials. It may be noted that the displacement functions have units of L^2/F where L is a length unit and F is force. The in-plane displacement functions for the upper material $k = 1$ are given by

$$
\begin{aligned}
{}_1U_1^{(1)} &= {}_1c_1^* \sum_{s=1}^{2}\sum_{t=1}^{2} (-1)^{s+t}\, {}_1\widetilde{N}_{st}\, {}_1Q_s \left({}_1N_{st}^*\widetilde{D} + \beta_s^{*(1)}\right) \\
{}_1U_1^{(2)} &= {}_1c_1^* \sum_{s=1}^{2}\sum_{t=1}^{2} (-1)^{s}\, {}_1\widetilde{N}_{st}\, {}_1Q_s \left({}_1n_{st}^*\widetilde{D} + {}_1M_{st}^*\beta_s^{*(1)}\right) \\
{}_1U_2^{(1)} &= {}_1c_1^* \sum_{s=1}^{2}\sum_{t=1}^{2} (-1)^{s}\, {}_1\widetilde{N}_{st}\, {}_1Q_{s+2}\beta_s{}^{(1)^{-1}} \left({}_1M_{st}^*\widetilde{D} + {}_1n_{st}^*\beta_s{}^{*(1)}\right) \\
{}_1U_2^{(2)} &= -{}_1c_1^* \sum_{s=1}^{2}\sum_{t=1}^{2} (-1)^{s+t}\, {}_1\widetilde{N}_{st}\, {}_1Q_{s+2}\beta_s{}^{(1)^{-1}} \left(\widetilde{D} + {}_1N_{st}^*\beta_s^{*(1)}\right).
\end{aligned} \tag{C.37}
$$

For the lower material, $k = 2$, the displacement functions are given as

$$
\begin{aligned}
{}_2U_1^{(1)} &= {}_2c_1^* \sum_{t=1}^{2} {}_2\widetilde{N}_{1t} \left({}_2N_{1t}^*\kappa_1\widetilde{D} + \kappa_2\right) - {}_2n_{12}\widetilde{c}\left({}_2N_{12}\widetilde{D} - {}_2N_{11}\right) \\
{}_2U_1^{(2)} &= -{}_2c_1^* \sum_{t=1}^{2} (-1)^{t}\, {}_2\widetilde{N}_{1t} \left({}_2n_{1t}^*\kappa_1\widetilde{D} - {}_2M_{1t}^*\kappa_2\right) - {}_2n_{11}\widetilde{c}\left({}_2N_{11}\widetilde{D} - {}_2N_{12}\right) \\
{}_2U_2^{(1)} &= -{}_2c_1^* \sum_{t=1}^{2} (-1)^{t}\, {}_2\widetilde{N}_{1t} \left({}_2M_{1t}^*\kappa_2\widetilde{D} - {}_2n_{1t}^*\kappa_1\right) + {}_2n_{11}\widetilde{c}\left({}_2N_{12}\widetilde{D} - {}_2N_{11}\right) \\
{}_2U_2^{(2)} &= {}_2c_1^* \sum_{t=1}^{2} {}_2\widetilde{N}_{1t} \left(\kappa_2\widetilde{D} + {}_2N_{1t}^*\kappa_1\right) - {}_2n_{12}\widetilde{c}\left({}_2N_{11}\widetilde{D} - {}_2N_{12}\right).
\end{aligned} \tag{C.38}
$$

Finally, the out-of-plane displacement functions in Eq. (2.7),

$$ {}_kU_3^{(III)} = 2\sqrt{s_{44}^{\prime(k)}\, s_{55}^{\prime(k)}}\, {}_kB_3^{\frac{1}{4}}\, {}_kn_{32}\,. \tag{C.39} $$

References

1. Banks-Sills L, Boniface V (2000) Fracture mechanics for an interface crack between a special pair of transversely isotropic materials. In: Chuang T-J, Rudnicki, JW (eds) Multiscale deformation and fracture in materials and structures–the James R. Rice 60th anniversary volume. Kluwer Academic Publishers, The Netherlands, pp 183–204
2. Freed Y, Banks-Sills, L (2005) A through interface crack between a ±45° transversely isotropic pair of materials. Int J Fract 133:1–41
3. Ting TCT (1996) Anisotropic elasticity–theory and applications. Oxford University Press, Oxford

Index

L. Banks-Sills, *Interface Fracture and Delaminations in Composite Materials*, SpringerBriefs in Structural Mechanics, DOI 10.1007/978-3-319-60327-8